

University of Warwick institutional repository: <http://go.warwick.ac.uk/wrap>

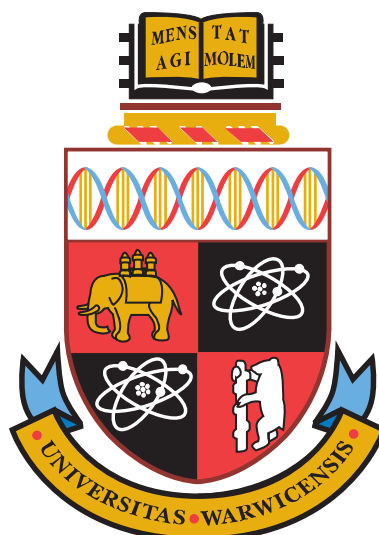
A Thesis Submitted for the Degree of PhD at the University of Warwick

<http://go.warwick.ac.uk/wrap/60308>

This thesis is made available online and is protected by original copyright.

Please scroll down to view the document itself.

Please refer to the repository record for this item for information to help you to cite it. Our policy information is available from the repository home page.



Investigation of the structure and optical properties of $\text{LiNb}_{1-x}\text{Ta}_x\text{O}_3$

by

Steven Huband

Thesis

Submitted to the University of Warwick

for the degree of

Doctor of Philosophy

Department of Physics

September 2013

THE UNIVERSITY OF
WARWICK

Contents

Title page	i
Contents	ii
List of Tables	vii
List of Figures	ix
Acknowledgments	xiii
Declaration and published work	xv
Abstract	xvi
Glossary and abbreviations	xvii
Chapter 1 Introduction	1
1.1 Birefringence	1
1.2 Structure	4
1.3 Piezoelectricity	7
1.4 Literature review	7
1.4.1 Room-temperature structure	8
1.4.2 High-temperature structure	9

1.4.3	Variable Li content	10
1.4.4	Congruent compositions	11
1.4.5	Optical properties	12
1.4.6	Piezoresponse	14
1.4.7	Lithium niobate-tantalate	14
1.4.8	Twinning	16
1.4.9	Density functional theory	16
1.5	Aims of present work	17
	References	19
Chapter 2	Experimental techniques and theory	24
2.1	Diffraction and refinement	24
2.1.1	Neutron and X-ray diffraction	24
2.1.2	Diffractometers	25
2.1.3	Rietveld refinement	25
2.1.3.1	Refinable parameters	28
2.1.3.2	Peak shapes	29
2.1.3.3	Preferred orientation	30
2.1.3.4	Anisotropic peak broadening	32
2.1.4	Single-crystal structure refinement	33
2.2	Birefringence measurements	34
2.2.1	Optical theory	34
2.2.2	Rotating polariser method	34
2.3	Second harmonic generation	36
2.3.1	Nonlinear optics	36
2.4	Density functional theory	38
2.4.1	The Born-Oppenheimer approximation	38
2.4.2	The Kohn-Sham equations	39
2.4.3	Solving the Kohn-Sham equations	39
2.4.4	The full potential LAPW method	41
2.4.5	Optical properties from DFT calculations	42
	References	43

Chapter 3 Powder diffraction study of $\text{LiNb}_{1-x}\text{Ta}_x\text{O}_3$	45
3.1 Sample preparation	45
3.2 Room-temperature X-ray powder diffraction	45
3.3 High-temperature X-ray powder diffraction	53
3.3.1 Lattice parameters	54
3.3.2 Curie point	59
3.4 Low-temperature X-ray powder diffraction	60
3.4.1 Lattice parameters	62
3.5 Conclusions	63
References	66
Chapter 4 Powder diffraction study of $\text{Li}_y\text{Ta}_{1-y}\text{O}_3$	67
4.1 XRD measurements	67
4.1.1 Room-temperature measurements	67
4.1.2 High-temperature measurements	75
4.1.2.1 Lattice parameters	75
4.1.2.2 Curie point	75
4.1.2.3 Atomic positions	75
4.2 Isotopically enriched SLT	78
4.2.1 Introduction	78
4.2.2 XRD measurements	78
4.2.3 Neutron diffraction measurements	81
4.2.4 Lattice parameters	84
4.2.5 Atomic positions	84
4.2.6 Bond lengths	86
4.3 Conclusions	87
References	89
Chapter 5 Single-crystal measurements	90
5.1 Experimental details	90
5.1.1 Single-crystal X-ray diffraction	90
5.1.2 Energy dispersive X-ray spectroscopy	91
5.2 Growth using a floating zone furnace	93

5.2.1	Experimental details	93
5.2.2	Results and analysis	93
5.3	Growth using a lithium vanadate flux	95
5.3.1	Experimental details	95
5.3.2	Crystal orientation	96
5.3.3	Composition	97
5.3.4	Results and analysis	98
5.3.4.1	Lattice parameters	102
5.3.4.2	Atomic positions	102
5.3.4.3	Curie point	104
5.4	Commercially-grown lithium tantalate	106
5.4.1	Piezoresponse	106
5.4.2	Absolute structure determination	106
5.4.2.1	Experimental details	106
5.4.2.2	Results and analysis	107
5.5	Conclusions	108
	References	109
Chapter 6	Optical measurements and calculations	110
6.1	Birefringence measurements	110
6.1.1	Floating zone LNT94 crystal	110
6.1.2	LV flux crystals	111
6.1.3	Commercially-grown LT	115
6.2	DFT calculations using Wien2k	116
6.2.1	Introduction	116
6.2.2	Convergence of calculations	116
6.2.3	Results of calculations on SLT	119
6.2.4	The effect of each atom on the optical properties	121
6.2.4.1	Extraordinary refractive index	122
6.2.4.2	Ordinary refractive index	122
6.2.4.3	Birefringence	123
6.3	Conclusions	124
	References	127

Chapter 7	Conclusions and future work	129
7.1	LNT	129
7.2	LT	129
7.3	Single-crystal measurements	130
7.4	DFT calculations	130
7.5	Final conclusions	131
7.6	Future work	131
	References	134
Appendix A	Rietveld example file	135
Appendix B	Metripol examples	138

List of Tables

1-1	The seven crystal systems, with restrictions on lattice parameters and indicatrix shape	3
1-2	Atomic position parameters for rhombohedral and hexagonal unit cells .	5
1-3	Megaw atomic position parameters for LN	9
1-4	Megaw atomic position parameters for LT	9
2-1	Parameters used in Rietveld refinements	29
2-2	Peak functions used in Rietveld refinement	31
2-3	Refinable FWHM expressions	31
2-4	S_{HKL} restrictions for trigonal crystal systems in a hexagonal setting . . .	32
2-5	Definitions of the goodness-of-fit parameters for single-crystal refinement	34
3-1	Scale factors applied to Bragg peaks during refinements	49
5-1	Collection and refinement details from LNT94 single-crystal diffraction measurements	95
5-2	Angles (°) between lattice directions	95
5-3	Refinement details for LNT0	98
5-4	Refinement details for LNT10	99
5-5	Refinement details for LNT20	99
5-6	Refinement details for LNT30	99
5-7	Refinement details for LNT40	100

5-8	Refinement details for LNT50	100
5-9	Refinement details for LNT60	100
5-10	Refinement details for LNT70	101
5-11	Refinement details for LNT80	101
5-12	Refinement details for LNT90	101
5-13	Refinement details for LNT100	102
5-14	Refinement details for poled CLT crystal	107

List of Figures

1-1	2D indicatrix	2
1-2	3D indicatrix	2
1-3	Hexagonal setting of a trigonal system	4
1-4	Structure of LN and LT	5
1-5	Structure of LN and LT with $\omega = 0^\circ$	6
1-6	Structure of LN and LT with $\omega = 30^\circ$	6
1-7	Number of publications containing ‘lithium tantalate’ or ‘lithium niobate’	8
1-8	LN phase diagram	11
1-9	Refractive indices of CLN	13
1-10	The measured zero-birefringence point of LT as a function of Li content	13
1-11	The measured refractive indices of CLNT as a function of composition	15
1-12	The calculated and measured birefringence as a function of LT content of LNT	17
2-1	Schematic of Bragg-Brentano diffractometer setup	26
2-2	Diagram of the single-crystal diffractometer used in this thesis	27
2-3	Illustration of the effect of sample-height error in powder diffraction	30
2-4	The experimental setup of the Metripol system	35
2-5	Example of measured $ \sin \delta $ using the Metripol system	36
2-6	Experimental setup for SHG measurements	38
2-7	Flow chart for self-consistent solutions of Kohn-Sham equations	40

3-1	XRD measurements on LNT powders across the compositional range . . .	47
3-2	Rietveld refinement of LNT powder made with with 100 % LT	50
3-3	Lattice parameters as a function of the LT content of LNT powders . . .	51
3-4	Structural parameters from Rietveld refinement	52
3-5	<i>c</i> lattice parameters as a function of temperature for Ta-rich LNT samples	55
3-6	Ta displacement as a function of temperature for Ta-rich samples of LNT	56
3-7	The <i>a</i> lattice parameter as a function of temperature	57
3-8	Ta displacement as a function of temperature for Ta-rich samples of LNT	58
3-9	O-O bond lengths in the O octahedra	59
3-10	O-O bond lengths in LNT100 as a function of temperature	59
3-11	Residuals from linear fits to the <i>a</i> lattice parameter	61
3-12	High-temperature phase transition as a function of LT content in the LNT sample	62
3-13	Low-temperature Rietveld refinement of LNT94	63
3-14	Low-temperature lattice parameters	65
4-1	XRD measurements on LT powders made with 48 to 54 mol % Li ₂ O in the initial material	68
4-2	XRD measurements on LT powder samples	69
4-3	Peak widths as a function Li content	70
4-4	Rietveld refinement of LT54 powder	71
4-5	L3T content in LT powders	72
4-6	Lattice parameters as a function of LT content	73
4-7	Displacement of Ta and Li as a function of Li content	74
4-8	The octahedral distortion and tilt as a function of Li content	74
4-9	<i>c</i> lattice parameter as a function of temperature	76
4-10	<i>a</i> lattice parameter as a function of temperature	77
4-11	Curie point as a function of Li content	78
4-12	Ta displacement as a function of Li content	79
4-13	Octahedral tilt as a function of Li content	80
4-14	Lattice parameters as a function of temperature	81
4-15	Rietveld refinements of LT49.36	83
4-16	Lattice parameters as a function of temperature	84

4-17	Li and Ta displacements as a function of temperature	85
4-18	Octahedral distortion and tilt as a function of temperature	85
4-19	Oxygen octahedra showing O-O bond lengths	86
4-20	O-O bond lengths as a function of temperature	87
4-21	O-Li bond lengths as a function of temperature	87
4-22	O-Ta bond lengths as a function of temperature	88
5-1	Reciprocal space unwarp simulations for LNT crystals containing a mechanical twin	92
5-2	Reciprocal space unwarp for an LNT94 crystal containing a mechanical twin	94
5-3	XRD ω - 2θ scan on LNT70 single crystal.	97
5-4	EDX measurements on LNT crystals	98
5-5	Lattice parameters as a function of LT content	103
5-6	Refinement results on LNT crystals	104
5-7	Normalised SHG intensity as a function of temperature during heating of a LV flux grown LNT100 crystal.	105
6-1	$ \sin\delta $ as a function of increasing temperature for the float zone grown LNT94 crystal	112
6-2	$ \sin\delta $ as a function of temperature on LV flux grown samples using a wavelength of 550 nm.	113
6-3	Measured zero-birefringence temperature as a function of composition of the LV flux grown crystals	114
6-4	Measured $ \sin\delta $ of X-cut commercial CLT crystal as a function of temperature using a 550 nm filter	115
6-5	$ \sin\delta $ as a function of increasing temperature for the poled commercial Z-cut crystal	117
6-6	n_e and total energy as a function of k-points used in a calculation	118
6-7	n_e and total energy as a function of the $R_{MT}K_{MAX}$ used in a calculation .	118
6-8	The electronic band structure calculated from the refined structure of LT at 27 °C	120
6-9	Calculated refractive indices of SLT	121

6-10	Calculated n_e as a function of temperature	123
6-11	Calculated n_o as a function of temperature	124
6-12	Calculated birefringence as a function of temperature	125
7-1	Crossed-polars image of LNT90	132
B-1	Measured $ \sin \delta $, orientation and intensity images at 30 °C	139
B-2	Measured $ \sin \delta $, orientation and intensity images at 323 °C	140
B-3	Measured $ \sin \delta $, orientation and intensity images at 600 °C	141

Acknowledgments

I would like to thank my supervisor, Pam Thomas, for all the help and advice over the last four years. She has been invaluable in guiding my research during this time and not letting me spend too long investigating things that were ultimately not going to form part of this thesis.

I am grateful to all the help given to me by Ausrine Bartasyte, who has provided not only information and advice but also samples to aid my research. I am also grateful to Geetha Balakrishnan for growing a crystal for me using a floating zone furnace and to Steve York for his assistance with electron microscopy measurements.

I would like to thank all the Dave's for their help; Dave Walker for his instruction and guidance with all things X-ray diffraction related, Dave Woodward for his help with a range of measurements and finally Dave Hammond for fixing everything that broke during my four years in the lab. I must also thank Dean Keeble for sharing his extensive knowledge of single-crystal diffraction measurements and for many exciting evenings spent in experimental hutches while working at beamlines. He has been a constant source of advice, despite the majority of times telling me all my ideas were completely wrong, usually without me uttering a single word.

My thanks also to Andy, Aoife, Ben, Dan, Iain, Ollie, Mads, Matt, Martin, Meng and Rosie for making the time spent in the office and the lab an enjoyable experience. Aoife, Iain and Mads provided many an entertaining evening in the pub, with some conversations even related to our research. I am extremely grateful to Aoife especially,

for her help in designing our unfortunately rejected group logo. I would also like to thank all of my friends from my undergraduate and postgraduate years, especially my housemate James who helped make living in Coventry an enjoyable experience.

Finally, I would like to thank my parents and my brother for all their support and encouragement over the years. Without which I would not have been able to spend so many years as a student.

Declaration and published work

I declare that the work presented in this thesis is my own except where stated otherwise, and was carried out entirely at the University of Warwick, during the period of October 2009 to October 2013, under the supervision of Professor Pam Thomas. The research reported here has not been submitted, either wholly or in part, in this or any other academic institution for admission to a higher degree.

Some parts of the work reported and other work not reported in this thesis have been published, as listed below, with further submissions for publication in due course.

A.M. Glazer, N. Zhang, A. Bartasyte, D.S. Keeble, S. Huband, and P.A. Thomas, *Journal of Applied Crystallography* **43**, 1305-1313, (2010).

A.M. Glazer, N. Zhang, A. Bartasyte, D.S. Keeble, D.S. Keeble, S. Huband, P.A. Thomas, I. Gregora, F. Borodavka, S. Margueron, and J. Hilinka, *Journal of Applied Crystallography* **45**, 1030-1037, (2012).

A. Bartasyte, A.M. Glazer, F. Wondre, D. Prabhakaran, P.A. Thomas, S. Huband, D.S. Keeble, and S. Margueron, *Materials Chemistry and Physics* **134**, 728-735, (2012).

S. Huband
September 2013

Abstract

The structure and optical properties of lithium niobate-tantalate have been studied with a focus on the Ta-rich end of the solid solution series. Structural studies using a range of X-ray and neutron powder diffraction measurements between -230 and 820 °C have been performed on the full compositional range. Rietveld refinements of the collected diffraction data have allowed the structural changes to be investigated as a function of temperature and Ta content. To complement the structural investigations, the effect of the changes in the Li content in lithium tantalate has also been investigated. As the Li content is decreased or the temperature is increased, the Ta displacement and the octahedral tilt decrease which coincides with an increase in the birefringence.

Crystals of lithium niobate-tantalate, across the full compositional range have been made using a lithium vanadate flux growth technique. Single-crystal diffraction measurements confirmed the results of the powder diffraction measurements; the Nb/Ta displacement and octahedral tilt both decrease as the Ta content is increased. This also results in a decrease in the lattice parameters from lithium niobate to lithium tantalate. Birefringence measurements on the crystals as a function of temperature have been used to determine the point that the crystals become zero-birefringent and by comparison with the structural studies, have shown that the structures remain polar through the zero-birefringence points.

Finally, a series of DFT calculations on the structures determined using Rietveld refinements of the neutron powder diffraction measurements on LT have been used to investigate the effect of each atom on the optical properties. The optical properties are insensitive to the position of the Li and depend on the O and Ta positions. The position of the Ta atom has the largest effect on the optical properties and the calculated birefringence increases with increasing temperature as expected from experimental measurements.

Glossary and abbreviations

DFT	Density functional theory
esd	Estimated standard deviation
FWHM	Full width at half maximum
GGA	Generalised gradient approximation
<i>hkl</i>	Miller indices
L3T	Li_3TaO_4
LAPW	Linearised augmented plane wave
LN	Lithium niobate
LNT	Lithium niobate-tantalate
LT	Lithium tantalate
LV	Lithium vanadate
LDA	Local density approximation
MPD	Multipurpose diffractometer
PMT	Photomultiplier tube
RPA	Random phase approximation
SHG	Second-harmonic generation
VTE	Vapour transport equilibration
XRD	X-ray diffraction

CHAPTER 1

Introduction

Lithium niobate (LN) and lithium tantalate (LT) have both been used extensively for their optical properties; they are birefringent and have a non-linear optical (NLO) response to incident light. In this chapter a theoretical background of the optical properties and their relationship with crystal structures will be given. The crystal structure and its relationship to other physical properties of interest will also be discussed, followed by a literature review of previous research on LN, LT and lithium niobate-tantalate (LNT).

1.1 Birefringence

The speed of light through a transparent medium v is related to the speed of light in a vacuum c by the refractive index n according to $n = c/v$. For two orthogonally polarised rays of light travelling in the same direction through a transparent medium, the speeds of the waves can be different. The refractive indices for the two polarisations (n_1 and n_2) are used to define the birefringence:

$$\Delta n = n_1 - n_2 \tag{1-1}$$

The birefringence is a measure of the optical anisotropy of a material. The refractive index as a function of polarisation direction for a wave with constant direction is de-

scribed by an ellipse as shown in figure 1-1. The direction of the largest n is defined as the slow axis and the angle between this and the experimental x-axis is the orientation angle ϕ . For a material which is optically isotropic the refractive index is the same for

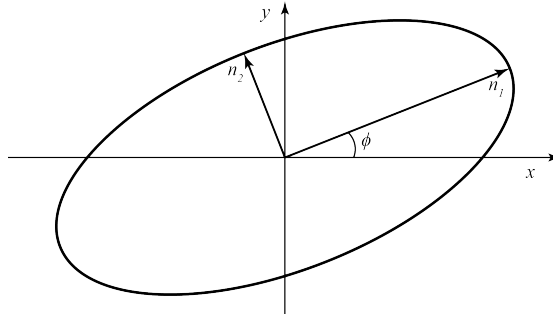


Figure 1-1 2D ellipse showing the variation of refractive index with polarisation direction.

all polarisation directions and the ellipse becomes a circle. If the direction of the light is allowed to pass through the medium in any direction, a refractive index surface in three dimensions can be created. This is called the indicatrix and is shown in figure 1-2.

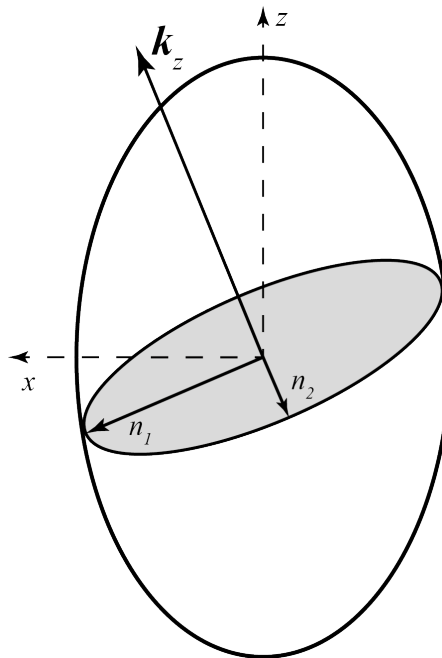


Figure 1-2 Representation of 3D ellipsoid showing the variation of refractive index with polarisation direction, the propagation direction is k_z .

The indicatrix in figure 1-2 is an example of a positive uniaxial crystal. A uniaxial crystal has $n_1 = n_2 \neq n_3$ and is described as positive when n_3 is larger than n_1 . The n_3 axis is defined as the optic axis because the refractive index becomes constant for all

Table 1-1 The seven crystal systems, with restrictions on lattice parameters and indicatrix shape.

Crystal system	Lattice parameter constraints	Indicatrix shape
Triclinic	None	Biaxial
Monoclinic	$\alpha = \gamma = 90^\circ, \beta \neq 90^\circ$	Biaxial
Orthorhombic	$\alpha = \beta = \gamma = 90^\circ$	Biaxial
Hexagonal	$a = b$ $\alpha = \beta = 90^\circ, \gamma = 120^\circ$	Uniaxial
Trigonal	$a = b = c$ $\alpha = \beta = \gamma \neq 90^\circ$ (rhombohedral setting)	Uniaxial
	$a = b$ $\alpha = \beta = 90^\circ, \gamma = 120^\circ$ (hexagonal setting)	
Tetragonal	$a = b$ $\alpha = \beta = \gamma = 90^\circ$	Uniaxial
Cubic	$a = b = c$ $\alpha = \beta = \gamma = 90^\circ$	Sphere

polarisations when light is travelling along this axis. For uniaxial crystals n_1 and n_2 are known as the ordinary refractive index (n_o) and n_3 as the extraordinary refractive index (n_e).

When $n_1 \neq n_2 \neq n_3$ there will be two possible optic axes and these crystals are known as biaxial. The seven crystal systems and their optical properties are listed in table 1-1 along with the imposed lattice parameter constraints. In this thesis the hexagonal setting of a trigonal system will be used. An example of the lattice and reciprocal lattice is shown in figure 1-3. The directions are labelled first by their corresponding lattice or reciprocal lattice vector, followed by their direction in reciprocal space $[hkl]$. All $[hkl]$ directions in this thesis are in reciprocal space.

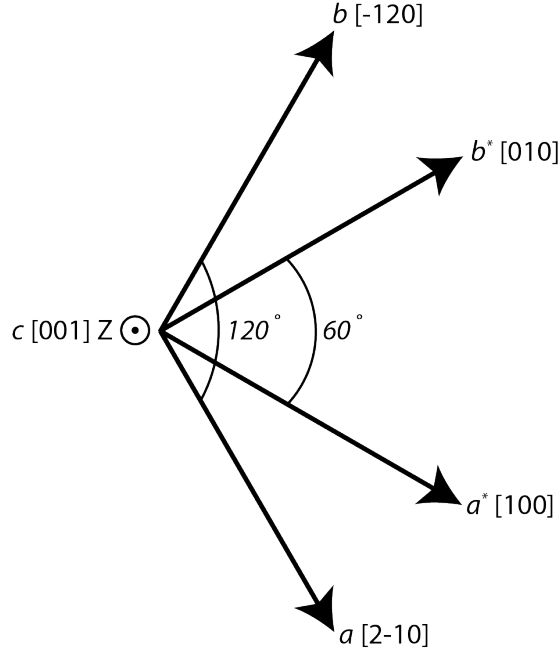


Figure 1-3 The hexagonal setting of a trigonal system. The angles between the lattice and reciprocal lattice vectors are also given. The axes are labelled first by their lattice or reciprocal lattice vector, followed by their direction in reciprocal space.

1.2 Structure

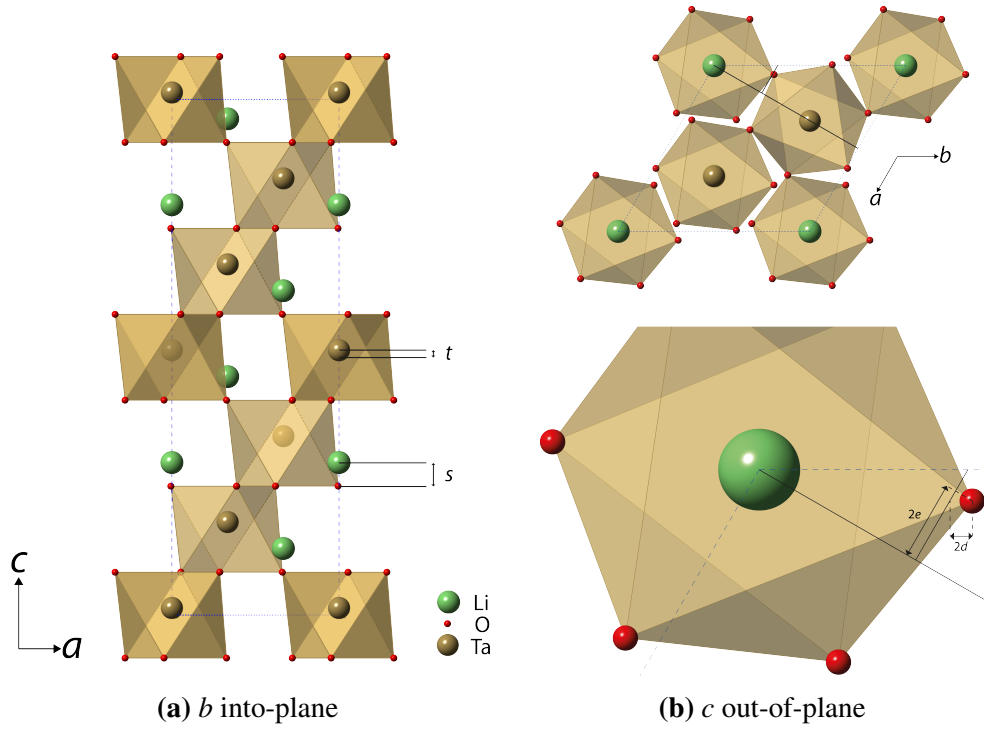
LN and LT have rhombohedral distorted perovskite structures and the unit cell of the structure is shown in figure 1-4a. The general formula for a perovskite material is ABO_3 and the O atoms form an octahedron around the B-site atom. In LN and LT the octahedra are distorted and tilted about the triad axis, as shown in figure 1-4b. The B-cation is also displaced from the centre of the octahedra and along the triad axis. The cation displacements and octahedral tilts will be described in this thesis using a set of parameters introduced by Megaw and Darlington for use with rhombohedral perovskites [1].

The atomic positions determined using the Megaw parameters are listed in table 1-2. The positions for the rhombohedral and hexagonal settings of the unit cell are both included. The hexagonal cell will be used throughout this thesis to describe the LN and LT structures. The position of the Li atom along the c axis is given by its displacement s from the plane of O atoms located at $1/4$. This plane and the displacement s are shown in figure 1-4a.

The position of the Ta atom along the c axis is given by the parameter t which

Table 1-2 Atomic position parameters for rhombohedral and hexagonal unit cells, based on table 2 in Megaw and Darlington [1].

Unit cell	Atom	a direction	b direction	c direction
Rhombohedral	A	$1/4 + s$	$1/4 + s$	$1/4 + s$
	B	t	t	t
	O	$1/4 - 2e - 2d$	$1/4 + 2e - 2d$	$-1/4 + 4d$
Hexagonal	A	0	0	$1/4 + s$
	B	0	0	t
	O	$1/6 - 2e - 2d$	$1/3 - 4d$	$1/12$

**Figure 1-4** The structure of LN and LT with (a) b into-plane and (b) c out-of-plane. The outline of the unit cell is given by the dashed blue line. The octahedral distortion parameter d and the tilt parameter e determining the O positions are also shown.

corresponds to the displacement of the Ta atom from the centre of the O octahedra. The d and e parameters determine the distortion and the tilt of the octahedra and their relation to the position of the O atom in the unit cell is shown in figure 1-4b. The tilt of the octahedra (ω) around the triad axis is calculated from the e parameter according to

$$\tan \omega = 4 \sqrt{3} e. \quad (1-2)$$

The change in the structure for tilt angles of 0 and 30°, with $d = 0$ are shown in figures

1-5 and 1-6, respectively. The top half of the unit cell has been omitted because the effect of the tilting is evident when only showing the bottom half. When the tilt angle is 0° , the O atom lies along the edge of the unit cell and all the octahedra are aligned along their edges. This results in an ideal hexagonal packing of the O atoms. As the tilt angle is increased the effect of the octahedral rotations can be seen in figure 1-6, where the tilt angle is 30° . The octahedra are now aligned along the corners and form the ideal perovskite structure.

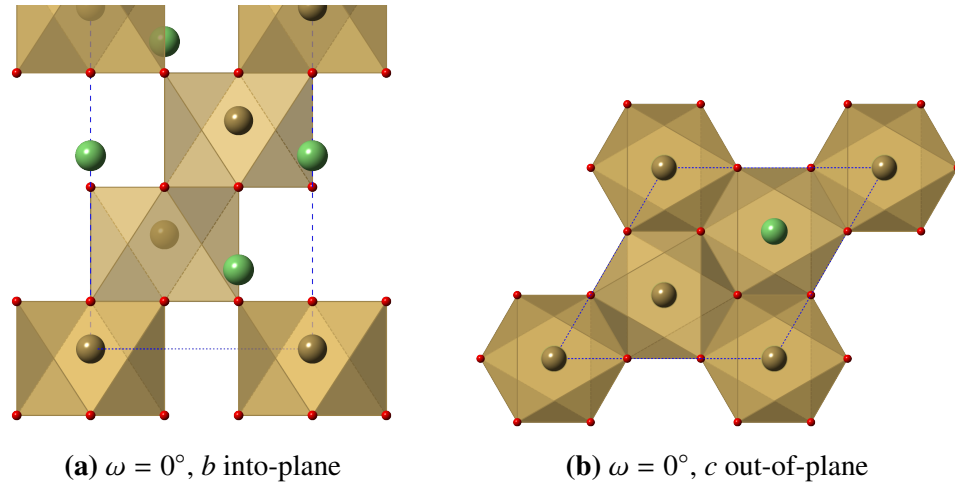


Figure 1-5 The structure of LN and LT with $\omega = 0^\circ$ for (a) b into-plane and (b) c out-of-plane.

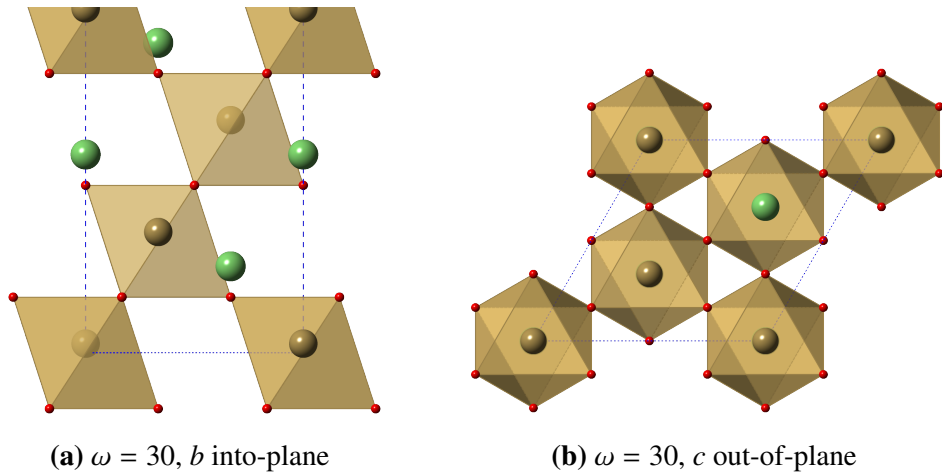


Figure 1-6 The structure of LN and LT with $\omega = 30^\circ$ for (a) b into-plane and (b) c out-of-plane.

1.3 Piezoelectricity

There are 32 crystal classes which describe the symmetry of a crystal and 11 of these contain a centre of symmetry. These are the centrosymmetric crystal classes and the other 21 are the non-centrosymmetric classes. Of these non-centrosymmetric classes, 20 exhibit electrical polarity in response to stress [2]. This is known as the piezoelectric effect and a strain developing due to an applied electric field is the converse-piezoelectric effect. The induced polarisation and strain are given by

$$P_i = \sum_{jk} d_{ijk} \sigma_{jk}, \quad (1-3)$$

$$\epsilon_{jk} = \sum_k d_{ijk} E_i, \quad (1-4)$$

where P_i is the induced polarisation, d_{ijk} is the piezoelectric tensor, σ_{jk} is the applied stress, ϵ_{jk} is the induced strain and E_i is the applied electric field. The piezoelectric tensor is a 3rd rank tensor with 18 coefficients, however, because of the crystal symmetries many of these are zero, and the non-zero ones related to each other [3]. For example, the piezoelectric tensor of a crystal with point group $3m$ is

$$d_{ijk} = \begin{pmatrix} 0 & 0 & 0 & 0 & d_{15} & -2d_{22} \\ -d_{22} & d_{22} & 0 & d_{15} & 0 & 0 \\ d_{31} & d_{31} & d_{33} & 0 & 0 & 0 \end{pmatrix}. \quad (1-5)$$

Of the 20 piezoelectric crystal systems, 10 are also polar and have a spontaneous polarisation. These materials are called ferroelectrics and the spontaneous polarisation is reversible with the application of an external electric field.

1.4 Literature review

A large number of publications have been produced on the properties and applications of LN, with over 9500 since 1970. The increasing quantity of research in LN can be seen in the number of publications each year containing ‘lithium niobate’ as shown in figure 1-7. The number of papers published for LT is considerably less than that of LN but it also follows a similar trend in the increasing number of publications. Despite the large quantity of research on both LN and LT the research on the solid-solution formed between them is small.

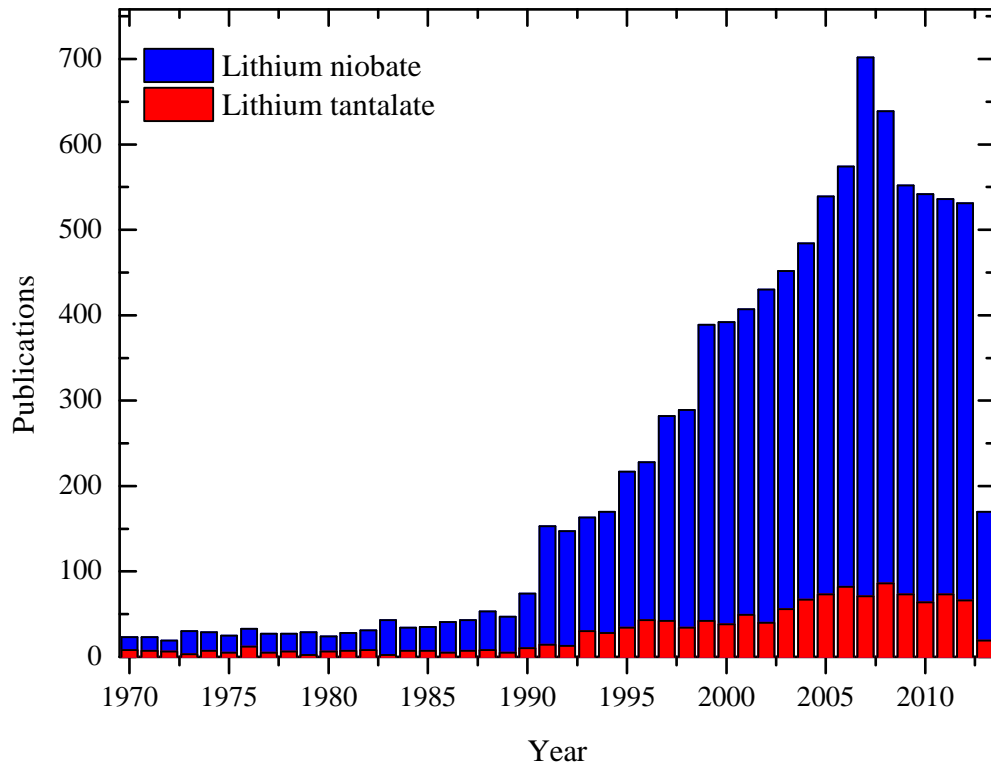


Figure 1-7 Number of publications with ‘lithium tantalate’ in the title, abstract or keywords overlaid on the same search for ‘lithium niobate’.

1.4.1 Room-temperature structure

The growth of single domain LN crystals and the initial measurements on them were published in a series of papers by Nassau et al [4, 5] and Abrahams et al [6–8]. The crystals were grown using the Czochralski technique, which requires a rotating seed crystal to be lowered into a melt of LN and slowly pulled out. As the crystal is pulled, the melt crystallizes onto the seed and large single crystals result. Based on single-crystal X-ray diffraction measurements the structure of LN is rhombohedral with hexagonal lattice parameters $a=5.14829 \pm 0.00002 \text{ \AA}$, $c=13.8631 \pm 0.0004 \text{ \AA}$, space group $R3c$ and point group $3m$ at room temperature [8]. The direction of the polarisation was measured using the different etching response between the positive and negative dipole surfaces and related to the measured structure. It was shown that the displacement of the Nb atom from the centre of the O octahedra was in the same direction as the positive dipole end. The measured atomic positions from the single-crystal neutron and X-ray diffraction measurements are given in table 1-3 using the Megaw position parameters.

The initial structural measurements on LT were made by Abrahams et al in a series

Table 1-3 Megaw atomic position parameters from X-ray and neutron diffraction measurements on LN [6, 7].

Radiation	s	t	d	e	Tilt angle
X-ray	0.71(1) Å	0.26(1) Å	-0.0028(1)	0.062(1)	23.1(1)°
Neutron	0.70(1) Å	0.28(1) Å	-0.0025(1)	0.062(1)	23.3(1)°

Table 1-4 Megaw atomic position parameters from X-ray and neutron diffraction measurements on LT [9, 10].

Radiation	s	t	d	e	Tilt angle
X-ray	0.63(1) Å	0.19(1) Å	-0.0016(1)	0.061(1)	22.0(1)°
Neutron	0.60(1) Å	0.20(1) Å	-0.0026(1)	0.061(1)	22.9(1)°

of papers using X-ray and neutron diffraction measurements similar to their work on LN [9, 10]. They confirmed that LT formed the same structure as LN and had lattice parameters of $a=5.15428 \pm 0.00001$ Å and $c=13.78351 \pm 0.00002$ Å. The absolute structure was determined and the Ta displacements were in the same direction as the positive dipole end, as measured on LN. The atomic positions, using the Megaw parameters are given in table 1-4.

1.4.2 High-temperature structure

The high-temperature phase of LN was investigated by Abrahams et al using X-ray diffraction measurements at 1200 °C, concluding that the space group was $R\bar{3}$ [8]. It was later suggested by Megaw that the loss of symmetry from $R\bar{3}$ to $R3c$ would be very unusual and the correct space group was actually $R\bar{3}c$ [11], which was confirmed by Niizeki et al by analysing the growth ridges formed during the pulling of crystals from the melt [12]. High-temperature neutron diffraction measurements at 1107 °C by Boyson and Altorfer confirmed the previous observations that this was the correct high-temperature space group [13]. The high-temperature phase of LT was also confirmed to be in space group $R\bar{3}c$ by Abrahams et al using neutron diffraction measurements at 667 °C [14].

The response of the LN crystal structure to increasing temperature has been measured using X-ray powder diffraction by Abrahams et al [8] and using single-crystal X-ray diffraction by Kim and Smith [15]. The expansion in the a and b lattice parameters is linear up to 1000 °C and the c lattice parameter reaches a maximum at about

600 °C and decreases on further heating. The decrease in the c lattice parameter was explained by Megaw and is a result of the O octahedra decreasing in size because of the decrease in the displacement of the Nb atoms from the centre of the octahedra [16]. The linear increase in the a and b lattice parameters is because of the linear increase in the octahedral tilt as the temperature increased. A similar trend was measured in the structure of LT by Kim and Smith, where the maximum in the c lattice parameter was at about 250 °C [15].

In these initial measurements as a function of temperature, the Curie point for LN was measured between 1140 °C and 1210 °C [4, 17]. This large range of possible values was because of the different Li concentrations in the samples. The effect of the Li content on the Curie point of Czochralski grown crystals was investigated by Bergman et al, who found it varied from 1070 to 1190 °C [18]. The initial materials used for the crystal growth had Li/Nb ratios ranging from 0.8 to 1.2, which will be given as $\text{Li}_{0.444}\text{Nb}_{0.556}\text{O}_3$ and $\text{Li}_{0.545}\text{Nb}_{0.455}\text{O}_3$ in this thesis. The composition of the crystals grown using this technique is not equal to the ratio of the initial materials and was undetermined in this study.

1.4.3 Variable Li content

The large range of physical properties of LN samples, led to an investigation of the effect of the Li content, and the first phase diagram of the Li_2O - Nb_2O_5 system was published by Lerner et al [19]. The solid-solution range for LN was given between 44 and 51 mol % Li_2O based on differential thermal analysis measurements and powder X-ray diffraction of sintered ceramic powders. The extension of the solid-solution range from 50 to 51 mol % Li_2O was based on measurements of the a lattice parameter, whereas the c lattice parameter measurements suggested the solid-solution range stops at 50 mol % Li_2O . The determination of the upper limit on the range is unreliable based on the measurements of the lattice parameters.

Similar measurements on sintered ceramic powders and Czochralski grown crystals were made by Carruthers et al, producing the phase diagram shown in figure 1-8 [20]. The ceramic powders were weighed before and after sintering to check for loss of Li_2O and it was concluded that some Li was lost but it was below the level of detection. The Curie point was found to vary between 1020 and 1180 °C as the composition varied from

46 to 50 mol % Li_2O . The upper limit to the solid-solution range was given as 50 mol % and is a more reliable result than that of Lerner et al because of the consideration given to the loss of Li_2O during sintering [21].

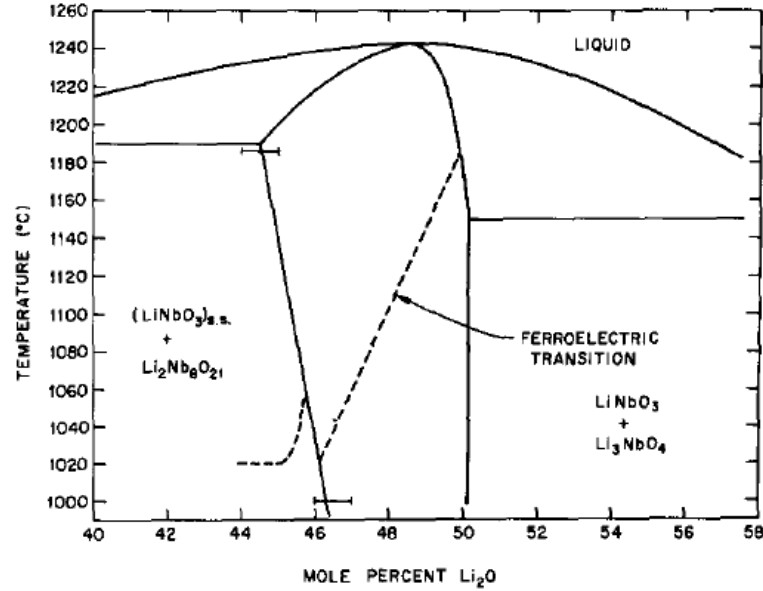


Figure 1-8 The phase diagram and measured Curie temperatures of LN produced by Carruthers et al [20].

The initial measurements investigating the effect of the Li content on the Curie point of LT were made by Ballman et al [22]: the composition of the Czochralski grown crystals was unknown and the Curie points were given as a function of the composition of the initial materials. This was resolved by Barns and Carruthers, who used these crystals and measurements of the Curie point in ceramic powders to estimate the composition of the crystals. The measured Curie points are between 510 and 690 °C as the composition varies from 46 to 50.4 mol % Li_2O .

1.4.4 Congruent compositions

The congruent melting composition has been determined for both LN and LT, allowing the growth of large crystals using the Czochralski technique. Initially the congruent composition of LN was determined to be between 48 and 49 mol % Li_2O by Lerner et al [19] and was later refined to 48.38 mol % Li_2O and 48.45 mol % Li_2O by O'Bryan et al [23] and Bordui et al [24], respectively. The congruent point of LT was determined to be 49 mol % Li_2O by Barns et al [21] and 48.75 mol % Li_2O by Miyazawa et al [25].

To improve the quality of the large number of crystals being grown commercially using the Czochralski technique, Kushibiki et al determined a precise value of 48.46 mol % Li_2O for the congruent composition of LT [26].

The initial defect structure for LN was proposed by Abrahams and Marsh to contain Nb atoms on the Li site and Nb vacancies for charge balance. This was determined using XRD and density measurements. However, the majority of the following structural investigations have shown that the average structure of CLN is best described by a Li vacancy model. Using both neutron and X-ray diffraction measurements the defect model has been described by the formula $\{\text{Li}_{1-5x} [\text{Nb}_{\text{Li}}]_x [\text{V}_{\text{Li}}]_{4x}\} \text{Nb}_{1-x}\text{O}_3$ [27–29].

1.4.5 Optical properties

The refractive indices of Czochralski grown CLN crystals have been determined by a range of authors as a function of both composition and wavelength. The Sellmeier equations for n_o and n_e as a function of temperature and of wavelength were determined by Hobden and Warner with measurements of the refractive index up to 374 °C using the lines of a helium discharge lamp [30]. Using these equations a zero-birefringence temperature for CLT is calculated as 882 °C. This is in agreement with the measurements made by Smith et al, which are shown in figure 1-9 [31]. These results show that the n_e varies more than the n_o and has a larger effect on the measured birefringence.

The change in the refractive indices as a function of wavelength has been studied by a range of authors showing that the refractive indices decrease with increasing wavelength [30, 32, 33]. Variations between the measured refractive indices on different crystals can be explained by the varying compositions of the crystals used. Bergman et al showed that n_o stays constant with changing Li content and n_e decreases as the concentration of Li is increased towards SLT [18].

The initial measurements of the refractive indices of CLT as a function of temperature were made by Iwasaki and Yamada from room temperature to 800 °C with a wavelength range between 468 and 644 nm [34]. These results showed that the birefringence was positive in CLT and became constant above the Curie point. These measurements were used by Abedin et al to produce a Sellmeier equation as a function of both wavelength and temperature for CLT [35]. The Sellmeier equations as a function of wavelength for n_o and n_e have been determined for SLT and CLT by Nakamura et al

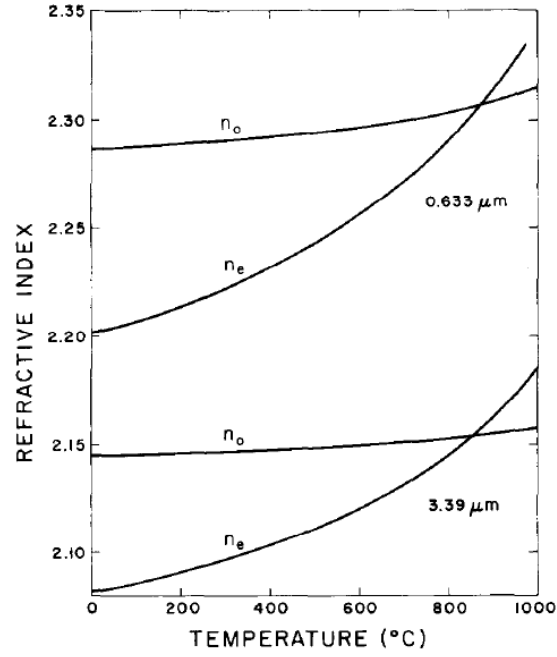


Figure 1-9 The measured refractive indices of CLN measured by Smith et al [31].

between 400 and 1100 nm [36]. The effect of the Li content on the zero-birefringence temperature was determined by Bäumer et al using vapour transport equilibration (VTE) treated CLT crystals and is shown in figure 1-10 [37]. VTE can be used to increase the Li content of congruent crystals and consists of heating a CLT crystal in a crucible containing a Li-rich mixture of Li_2O and Ta_2O_5 to above 1000 °C and dwelling for over 70 h. The measurements show the birefringence is negative for SLT, positive for CLT and becomes zero with a composition close to 49.4 mol % Li_2O .

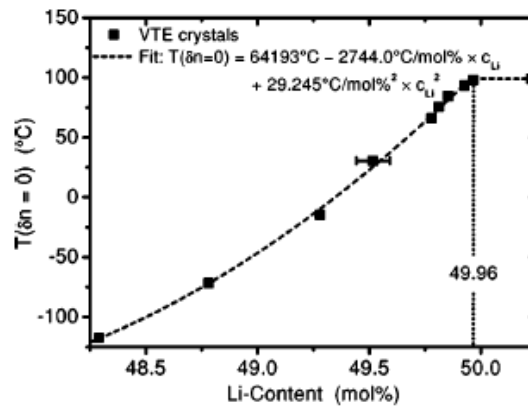


Figure 1-10 The measured zero-birefringence point of LT as a function of Li content [37].

1.4.6 Piezoresponse

The elastic and piezoelectric coefficients for CLN and CLT were determined by Warner et al [38], giving piezoelectric d_{33} values of 6 and 8 pC N⁻¹ for CLN and CLT, respectively. A study of the effect of the Li content on the piezoelectric properties has not been published, however, it is expected that the coefficients will vary between the congruent and stoichiometric compositions. LN and LT are not used for their piezoelectric properties because the d_{33} values are small in comparison to those of undoped lead zirconate-titanate (PZT) which has a d_{33} value of 200 pC N⁻¹ [39].

1.4.7 Lithium niobate-tantalate

It was shown by Peterson et al that a solid-solution existed between LN and LT and extended across the whole compositional range [40]. Powder stoichiometric lithium niobate-tantalate (SLNT) samples were investigated and the Curie point measured using capacitance measurements, showing a linear change from LN to LT. The lattice parameters were also measured using X-ray diffraction, however the errors on the calculated values were of a similar size to the difference between the values of LN and LT, making a trend in the measured values indeterminable.

The first attempts at growing crystals were made using the Czochralski technique by Sugii et al [41] and Fukuda et al [42]. They both successfully grew crystals across the compositional range, showing that the crystals formed Ta-rich compared to the initial materials and that the composition varies along the length of the pulled crystals. Fukuda et al also measured a linear change in the lattice parameters across the compositional range. The Czochralski technique was also used by Shimura and Fujino who investigated the Curie point and lattice parameters as a function of composition. They measured non-linear changes in the Curie point and lattice parameters of the crystals and used the previously determined linear changes to estimate the actual compositions of the grown crystals and allow the growth of crystals with a desired composition [43].

The refractive indices of the the Czochralski grown CLNT crystals were measured by Shimura and Fujino [44]. The measured refractive indices as a function of the corrected crystal composition are shown in figure 1-11 and show that for CLNT crystals a composition close to 95 mol % Ta will be zero-birefringent at room temperature, which

is independent of the wavelength of the light used. The linear change in the birefringence and Curie point with composition, as well as a zero-birefringence composition of 94 mol % Ta were also confirmed on Czochralski grown crystals by Wood et al [45].

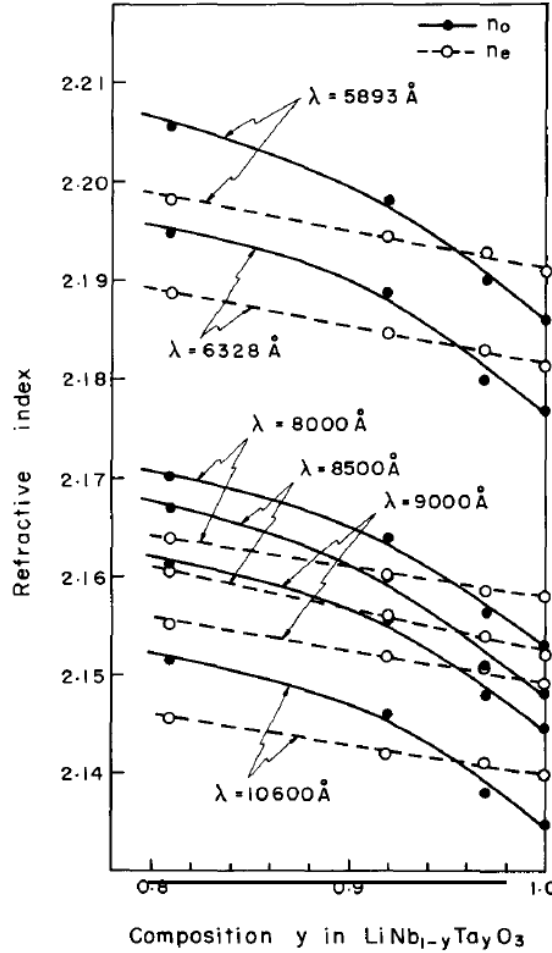


Figure 1-11 The measured refractive indices of CLNT as a function of composition [44].

More recently a range of different crystal growth methods have been investigated by Bartasyte et al [46]. This work included for the first time a consideration of the effect of the Li content on the properties of the LNT crystals. Crystals were made using the Czochralski, top seeded solution, floating zone and flux growth methods. It was concluded that both Czochralski and LiVO_3 (LV) flux grown crystals formed Ta-rich compared to the initial material and Li_2O was lost during the floating zone and top seeded solution growth methods. The growth using the LV flux was based on the phase diagram produced by Kondo et al, who used an LV flux for depositing LNT layers on LT substrates [47].

1.4.8 Twinning

The initial crystals of LN grown using the Czochralski technique contained visible twins and the twin plane was given as the (102) [4, 48]. Further investigation of the twinning in LN was performed by Blistanov et al which gave the twinning planes as (102), (-102) and the (-104) [49, 50]. The determination of the twin plane as the (102) has been shown to be incorrect and the (-102) twin plane has been confirmed by a range of authors [51–54]. The comprehensive investigation of the twinning in Czochralski grown LN by Park et al confirmed the twins are mechanical and not formed during the crystal growth. The symmetrically equivalent twin planes to the (-102) are the (012) and (1-12) and it can be expected for twins to form on any of these planes. The twinning of VTE treated LT crystals was studied by Glazer et al and confirmed the presence of twins consistent with the {-102} family of twin planes [55].

1.4.9 Density functional theory

A large number of density functional theory (DFT) calculations have been made on both LN and LT with an interest in calculating their electronic and optical properties. The band structure of LN and LT has been calculated using a number of different functionals and DFT codes and has resulted in a large range in the calculated direct band gap energy. Using the local-density approximation (LDA) on LN has resulted in values between 3.1 eV [56] and 3.52 eV [57] and between 3.3 eV [58] and 3.5 eV [59] with the generalised gradient approximation (GGA). These values have been compared to the experimentally measured value of 3.78 eV, measured by Dhar and Mansingh using optical transmission spectra [60]. One of the problems with calculations of the band structure using DFT is the systematic underestimation of the band gap and the agreement between the experimental value and calculated does not act to confirm to the validity of the calculation [61].

The previous DFT calculations have only used a single-particle picture, the effects of the self-energy of the system using the GW approximation (in GW the self-energy is given by the product of the Green's function G and the dynamically screened interaction W) were included by Thierfelder et al [62] and Rieffer et al [63], who also took electron-hole interactions into account, giving direct band gaps of 4.71 and 5.4 eV, respectively.

The discrepancy between the calculated direct band gaps using the GW approximation and the measured band gaps has been in part attributed to the effects of the electron-hole binding energy, which affects the measurement of the band gap using optical absorption methods. Due to this, it was suggested by Mamoun et al that the results of DFT calculations should be compared to well-known properties such as the refractive indices [64]. Their measurements made with the WIEN2k code [65], using the GGA and a scissor operator to increase the direct band gap from 3.5 to 4.9 eV, resulted in a close agreement between the calculated and experimentally-measured refractive indices.

Similar results have been calculated for LT, a band gap of 3.86 eV was calculated by Cabuk et al using LDA [66] and 3.71 eV by Riefer et al using GGA [67] using a single-particle picture. When the self-energy effects and the electron-hole interactions are taken into account, the the calculated band gap for LT is 5.65 eV [67].

DFT calculations on LNT have been made by Riefer et al [67] and Sanna et al [68] including the self-energy and electron-hole interactions. Riefer et al focused on calculating the optical properties across the compositional range: the calculated birefringence is plotted in figure 1-12 including the measured values by Wood et al [45].

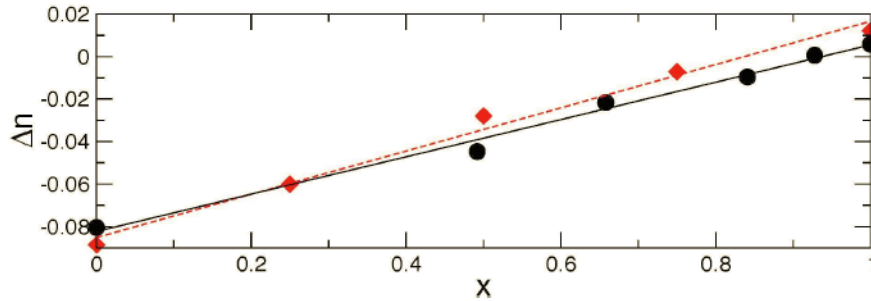


Figure 1-12 The calculated and measured birefringence as a function of LT-content given by Riefer et al [67] and [45], respectively. x is the Nb/Ta content according to the formula $\text{LiNb}_{1-x}\text{Ta}_x\text{O}_3$.

1.5 Aims of present work

The main aim of this body of work is to investigate the structure of LNT, LN and LT with a focus on when they have zero-birefringence. By combining structural measurements with birefringence measurements, it will be determined if the structure remains polar whilst being optically isotropic. Currently, the role of the structure in the optical

properties of LNT, LN and LT is poorly understood, with the temperature, Li content and LNT composition all affecting the optical properties. Structural measurements as a function of temperature, Li content and across the compositional range of LNT will increase the understanding of how the structural changes determine the optical properties. Structural measurements will be made on a large range of powder and single crystal samples.

Additionally, the absolute structure of CLT will be determined using X-ray diffraction measurements and a direct measurement of the piezoelectric d_{33} coefficient. This will be the first absolute structural determination of CLT which includes a direct measurement of the piezoelectric d_{33} coefficient and will be used to confirm the previous absolute structural determinations.

Finally, the refractive indices of the experimentally determined structures will be calculated using DFT calculations. These will focus on the structural changes as a function of temperature and include a series of calculations investigating the effects of each atom on the optical properties.

References

- [1] H. D. Megaw and C. N. W. Darlington, *Acta Crystallographica* **A31**, 161 (1975).
- [2] W. G. Cady, *Piezoelectricity* (Dover Publications, Inc, New York, 1964).
- [3] M. T. Dove, *Structure and dynamics: an atomic view of materials* (Oxford University Press, Oxford, 2003).
- [4] K. Nassau, H. J. Levinstein, and G. M. Loiacono, *Journal of Physics and Chemistry of Solids* **27**, 983 (1966).
- [5] K. Nassau, H. J. Levinstein, and G. M. Loiacono, *Journal of Physics and Chemistry of Solids* **27**, 989 (1966).
- [6] S. C. Abrahams, J. M. Reddy, and J. L. Bernstein, *Journal of Physics and Chemistry of Solids* **27**, 997 (1966).
- [7] S. C. Abrahams, W. C. Hamilton, and J. M. Reddy, *Journal of Physics and Chemistry of Solids* **27**, 1013 (1966).
- [8] S. C. Abrahams, H. J. Levinstein, and J. M. Reddy, *Journal of Physics and Chemistry of Solids* **27**, 1019 (1966).
- [9] S. C. Abrahams and J. L. Bernstein, *Journal of Physics and Chemistry of Solids* **28**, 1685 (1967).
- [10] S. C. Abrahams, W. C. Hamilton, and A. Sequeira, *Journal of Physics and Chemistry of Solids* **28**, 1693 (1967).

-
- [11] H. D. Megaw, *Acta Crystallographica Section A: Crystal Physics, Diffraction, Theoretical and General Crystallography* **24**, 583 (1968).
- [12] N. Niizeki, T. Yamada, and H. Toyoda, *Japanese Journal of Applied Physics* **6**, 318 (1967).
- [13] H. Boysen and F. Altorfer, *Acta Crystallographica Section B Structural Science* **50**, 405 (1994).
- [14] S. C. Abrahams, E. Buehler, W. C. Hamilton, and S. J. Laplaca, *Journal of Physics and Chemistry of Solids* **34**, 521 (1973).
- [15] Y. S. Kim and R. T. Smith, *Journal of Applied Physics* **40**, 4637 (1969).
- [16] H. D. Megaw, *Acta Crystallographica* **A24**, 589 (1968).
- [17] G. A. Smolenskii, N. N. Krainik, N. P. Khuchua, V. V. Zhadanova, and I. E. Mylnkova, *Physica Status Solidi (b)* **13**, 309 (1966).
- [18] J. G. Bergman, A. Ashkin, A. A. Ballman, J. M. Dziedzic, and H. J. Levinstein, *Applied Physics Letters* **12**, 92 (1968).
- [19] P. Lerner, C. Legras, and J. P. Dumas, *Journal of Crystal Growth* **3-4**, 231 (1968).
- [20] J. R. Carruthers, G. E. Peterson, M. Grasso, and P. M. Bridenbaugh, *Journal of Applied Physics* **42**, 1846 (1971).
- [21] R. L. Barns and J. R. Carruthers, *Journal of Applied Crystallography* **3**, 395 (1970).
- [22] A. A. Ballman, H. J. Levinstein, C. D. Capio, and H. Brown, *Journal of the American Ceramic Society* **50**, 657 (1967).
- [23] H. M. O'Bryan, P. K. Gallagher, and C. D. Brandle, *Journal of the American Ceramic Society* **68**, 493 (1985).
- [24] P. Bordui, R. Norwood, C. Bird, and G. Calvert, *Journal of Crystal Growth* **113**, 61 (1991).
- [25] S. Miyazawa and H. Iwasaki, *Journal of Crystal Growth* **10**, 276 (1971).
- [26] J. Kushibiki and Y. Ohashi, *IEEE Transactions on Ultrasonics, Ferroelectrics and Frequency Control* **53**, 385 (2006).
- [27] N. Iyi, K. Kitamura, F. Izumi, J. K. Yamamoto, T. Hayashi, H. Asano, and S. Kimura, *Journal of solid state chemistry* **101**, 340 (1992).

-
- [28] A. P. Wilkinson, A. k. Cheetham, and R. H. Jarman, *Journal of Applied Physics* **74**, 3080 (1993).
- [29] N. Zotov, H. Boysen, F. Frey, T. Metzger, and E. Born, *Journal of Physics and Chemistry of Solids* **55**, 145 (1994).
- [30] M. V. Hobden and J. Warner, *Physics Letters* **22**, 243 (1966).
- [31] D. S. Smith, H. D. Riccius, and R. P. Edwin, *optics communications* **17**, 332 (1976).
- [32] G. Boyd, W. Bond, and H. Carter, *Journal of Applied Physics* **38**, 1941 (1967).
- [33] D. F. Nelson and R. M. Mikulyak, *Journal of Applied Physics* **45**, 3688 (1974).
- [34] H. Iwasaki and T. Yamada, *Japanese Journal of Applied Physics* **7**, 185 (1968).
- [35] K. Z. Abedin and H. Ito, *Journal of Applied Physics* **80**, 6561 (1996).
- [36] M. Nakamura, S. Higuchi, S. Takekawa, K. Terabe, Y. Furukawa, and K. Kitamura, *Japanese Journal of Applied Physics* **41**, L465 (2002).
- [37] C. Baumer, D. Berben, K. Buse, H. Hesse, and J. Imbrock, *Applied Physics Letters* **82**, 2248 (2003).
- [38] A. W. Warner, M. Onoe, and G. A. Coquin, *The journal of the acoustical society of America* **42**, 1223 (1967).
- [39] B. Jaffe, W. R. Cook, and H. Jaffe, *Piezoelectric Ceramics* (Academic, London, 1971).
- [40] G. E. Peterson, P. M. Bridenbaugh, and P. Green, *The Journal of Chemical Physics* **46**, 4009 (1967).
- [41] K. Sugii, H. Koizumi, and S. Kondo, *Journal of Crystal Growth* **33**, 199 (1976).
- [42] T. Fukuda and H. Hirano, *Journal of Crystal Growth* **35**, 127 (1976).
- [43] F. Shimura and Y. Fujino, *Journal of Crystal Growth* **38**, 293 (1977).
- [44] F. Shimura, *Journal of Crystal Growth* **42**, 579 (1977).
- [45] I. G. Wood, P. Daniels, R. H. Brown, and A. M. Glazer, *Journal of physics. Condensed matter* **20**, 235237 (2008).

-
- [46] A. Bartasyte, A. M. Glazer, F. Wondre, D. Prabhakaran, P. A. Thomas, S. Huband, D. S. Keeble, and S. Margueron, *Materials Chemistry and Physics* **134**, 728 (2012).
- [47] S. Kondo, K. Sugii, S. Miyazawa, and S. Uehara, *Journal of Crystal Growth* **46**, 314 (1979).
- [48] A. W. Vere, *Journal of Materials Science* **3**, 617 (1968).
- [49] A. A. Blistanov, I. V. Nosova, and M. M. Tagieva, *Kristallografiya* **20**, 666 (1975).
- [50] A. A. Blistanov, I. V. Nosova, and M. M. Tagieva, *Kristallografiya* **21**, 217 (1976).
- [51] G. H. Azarbajane, *Journal of Crystal Growth* **7**, 327 (1970).
- [52] A. Kalantarian, G. Mayilyan, A. D. Gladun, and R. A. Vardanian, *Philosophical Magazine A* **76**, 319 (1997).
- [53] M. B. Park, K. Kitamura, K. Terabe, Y. Furukawa, Y. Ji, and E. Suzuki, *Journal of Crystal Growth* **180**, 101 (1997).
- [54] B. M. Park, K. Kitamura, Y. Furukawa, and Y. Ji, *Journal of the American Ceramic Society* **80**, 2689 (1997).
- [55] A. M. Glazer, N. Zhang, A. Bartasyte, D. S. Keeble, S. Huband, P. A. Thomas, I. Gregora, F. Borodavka, S. Margueron, and J. Hlinka, *Journal of Applied Crystallography* **45**, 1030 (2012).
- [56] I. Inbar and R. E. Cohen, *Physical review. B* **53**, 1193 (1996).
- [57] Q. Li, B. Wang, C. H. Woo, H. Wang, and R. Wang, *Journal of Physics and Chemistry of Solids* **68**, 1336 (2007).
- [58] H. A. Rahnamaye Aliabad and I. Ahmad, *Physica B: Condensed Matter* **407**, 368 (2012).
- [59] M. Veithen and P. h. Ghosez, *Physical Review B* **65**, 1 (2002).
- [60] A. Dhar and A. Mansingh, *Journal of Applied Physics* **68**, 5804 (1990).
- [61] M. T. Yin and M. L. Cohen, *Physical Review B* **26**, 5668 (1982).
- [62] C. Thierfelder, S. Sanna, A. Schindlmayr, and W. G. Schmidt, *Physica Status Solidi (C)* **7**, 362 (2010).

- [63] A. Riefer, S. Sanna, A. V. Gavrilenko, and W. G. Schmidt, IEEE Transactions on Ultrasonics, Ferroelectrics and Frequency Control **59**, 1929 (2012).
- [64] S. Mamoun, A. E. Merad, and L. Guilbert, Computational Materials Science **79**, 125 (2013).
- [65] P. Blaha, K. Schwartz, G. Madsen, D. Kvasnicka, and J. Luitz, *WIEN2k, An augmented plane wave plus local orbitals program for calculating crystal properties*, vol. 1 (Vienna, 2001), ISBN 3950103112.
- [66] S. Cabuk, International Journal of Modern Physics B **24**, 6277 (2010).
- [67] A. Riefer, S. Sanna, and W. G. Schmidt, Proceedings of ISAF-ECAPD-PFM 2012 (2012).
- [68] S. Sanna, A. Riefer, S. Neufeld, and W. G. Schmidt, Proceedings of ISAF-ECAPD-PFM 2012 (2012).

Experimental techniques and theory

2.1 Diffraction and refinement

2.1.1 Neutron and X-ray diffraction

A detailed description of the theory of diffraction is given in Giacovazzo and will not be repeated in this thesis [1]. A comparison between using neutrons or X-rays and a detailed analysis of the diffraction experiments will be given. The structure factor for X-ray diffraction is

$$F_k = \sum_j f_j \exp[2\pi i(hx_j + ky_j + lz_j)] \exp[-8\pi^2 \langle u_j \rangle^2 \sin^2 \theta / \lambda^2], \quad (2-1)$$

where f_j is the scattering factor for the j th atom, x_j , y_j and z_j are the positions of the j th atom and $\langle u_j \rangle^2$ is the mean-squared atomic displacement. $8\pi^2 \langle u_j \rangle^2 \sin^2 \theta / \lambda^2$ is often called the temperature factor because $\langle u_j \rangle^2$ is proportional to the temperature. The atomic displacements can be modelled isotropically or anisotropically, requiring one or six parameters, respectively.

The structure factor for neutron diffraction is the same, with the X-ray scattering factor replaced by the neutron scattering length (b_j). The neutron and X-ray scattering factors vary as a function of atomic number (Z) and scattering angle. The X-ray scat-

tering factor increases with increasing atomic number, whereas the neutron scattering factor does not follow a trend. This makes neutron diffraction a valuable technique for measuring the structure of materials containing low-Z content elements.

2.1.2 Diffractometers

A PANalytical X'Pert Pro multipurpose diffractometer (MPD) was used for room- and high-temperature powder diffraction measurements. This has a Bragg-Brentano geometry and is equipped with a germanium curved-Johansson monochromator providing $\text{CuK}\alpha_1$ radiation. A schematic diagram of a Bragg-Brentano diffractometer is shown in figure 2-1. The diffractometer is equipped with a PANalytical PIXcel detector, consisting of 255 separate channels to provide an active length of 3.347° . The incident beam optics consist of divergence slits and a beam mask. The divergence slit acts to reduce the axial divergence of the incoming beam and the beam mask reduces the horizontal width of the beam. The diffracted beam optics consist of an anti-scatter slit and soller slits to ensure only the desired diffracted signal is measured. The majority of measurements in this thesis have been made using one X-ray tube which has reduced in intensity by a factor of four over its three year lifetime. The decrease in the intensity of the X-ray beam also resulted in a decrease in the signal to noise ratio.

For single-crystal diffraction measurements, an Oxford Diffraction Gemini diffractometer was used. This system is based around a four-circle goniometer with a kappa geometry and is equipped with a $\text{MoK}\alpha$ X-ray source and a CCD detector. A diagram of this diffractometer is shown in figure 2-2 with the important features labelled. The four-circle kappa geometry allows both accurate changes in the crystal orientation and easy access to the crystal for extra devices such as the Oxford Cryosystems Cobra equipped on this machine.

2.1.3 Rietveld refinement

Rietveld refinement is a whole-pattern-fitting structural refinement method for analysis of powder diffraction measurements. The initial development of the procedure was made by Hugo Rietveld and is described in his seminal papers on the subject [2, 3]. In the Rietveld method a series of least-squares refinements are carried out until the best

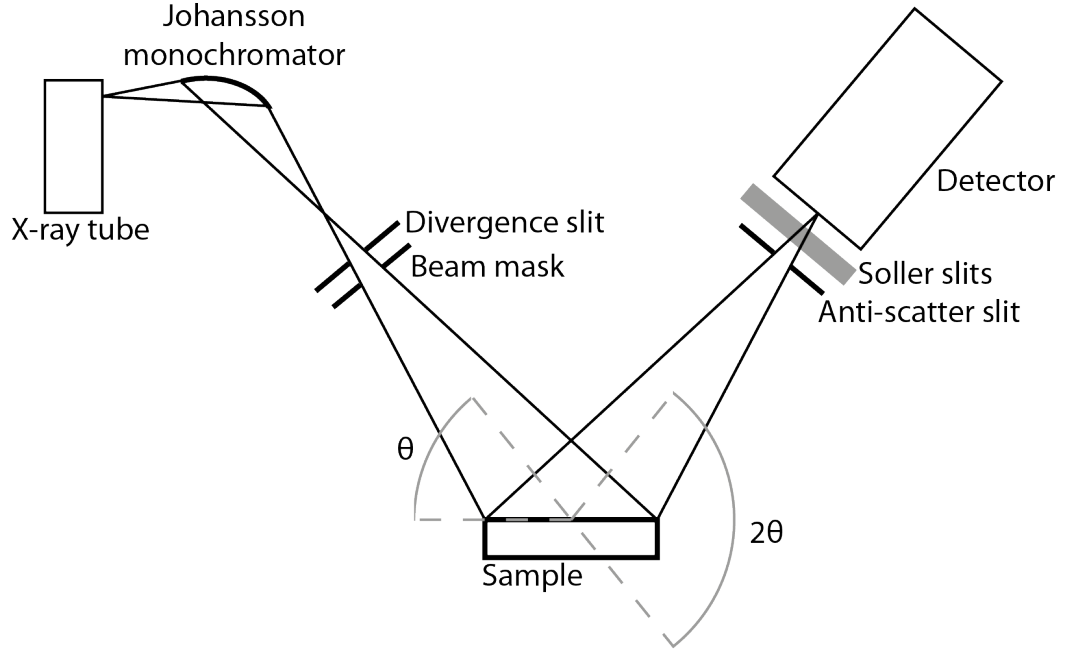


Figure 2-1 Schematic of Bragg-Brentano diffractometer equipped with a germanium curved-Johansson monochromator providing $\text{CuK}\alpha_1$ radiation.

fit between the measured and calculated diffraction patterns is attained. The calculated diffraction pattern is formed by refining the crystal structure, diffraction optics effects, instrumental factors and other specimen characteristics as required. During a least-squares refinement the quantity minimised is the residual, which is given by

$$S_i = \sum_i w_i (y_{oi} - y_{ci})^2, \quad (2-2)$$

where $w_i = 1/y_{oi}$ is the weighting factor for the observation, y_{oi} is the observed intensity of the i th step and y_{ci} is the calculated intensity of the i th step. The calculated intensity is given by

$$y_{ci} = sf \sum_K L_K |F_K|^2 \phi(2\theta_i - 2\theta_K) P_K A + y_{bi}, \quad (2-3)$$

where sf is the scale factor, K represents the Miller indices, h, k, l for a Bragg reflection, L_K contains Lorentz, polarisation and multiplicity factors, $\phi(2\theta_i - 2\theta_K)$ is the reflection profile function, P_K is the preferred orientation function, A is the absorption factor, F_K is the structure factor of the K th Bragg reflection and y_{bi} is the background intensity at the i th step [4].

The least-squares minimisation procedure leads to a set of equations based on the

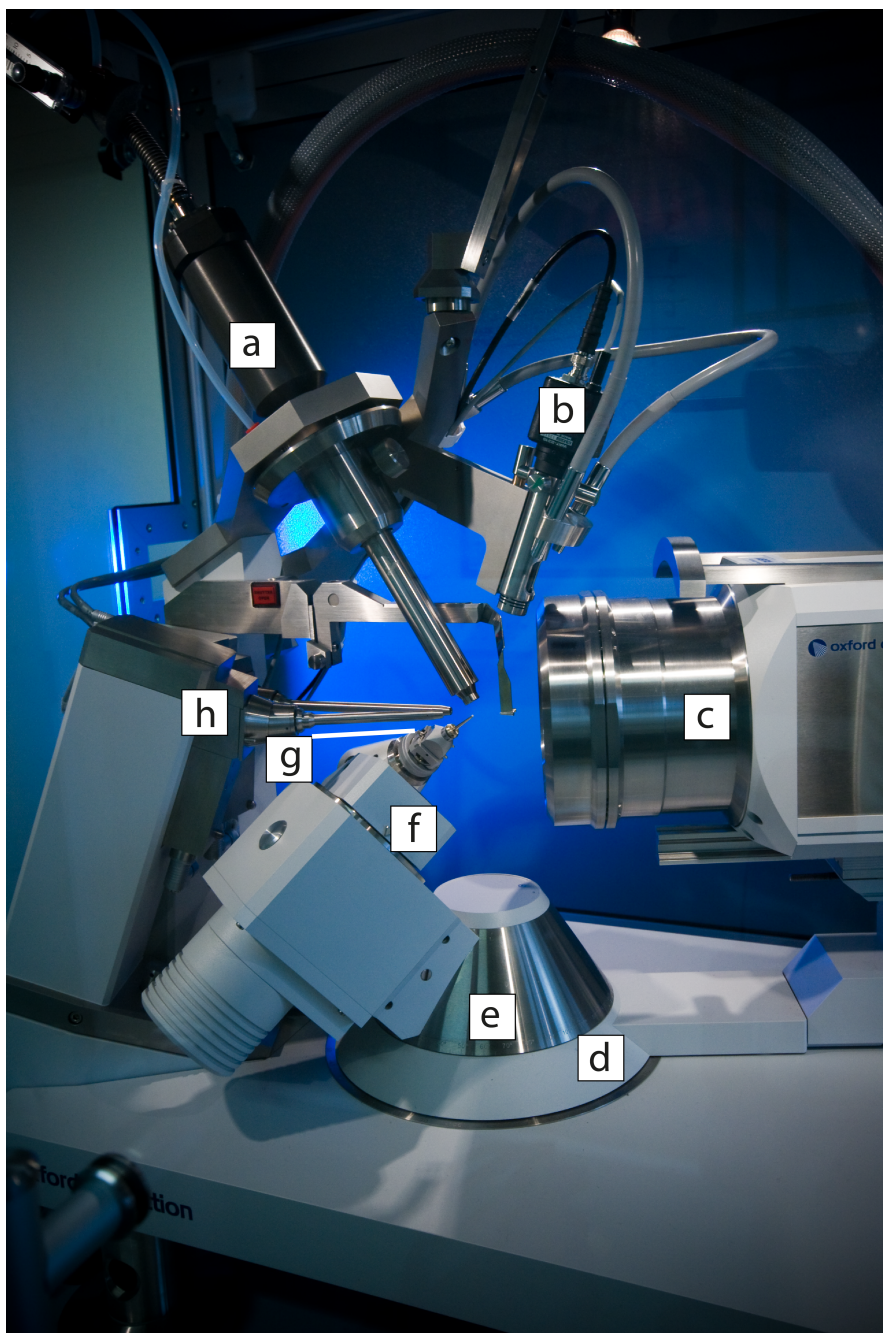


Figure 2-2 An Oxford Diffraction Gemini diffractometer used for single-crystal diffraction measurements. The labeled parts are (a) the Oxford Cryosystems Cobra for low-temperature measurements, (b) the video microscope for aligning crystals, (c) the CCD detector, (d) the 2θ circle of the detector, (e) the ω circle, (f) the κ circle, (g) the ϕ circle and goniometer head and (h) the X-ray tube and collimator.

derivatives of the calculated intensities with respect to each refinable parameter. These equations are solved by inversion of the normal matrix M_{jk} given by

$$M_{jk} = - \sum_i 2w_i \left[(y_{oi} - y_{ci}) \frac{\partial^2 y_{ci}}{\partial x_j \partial x_k} - \left(\frac{\partial y_{ci}}{\partial x_j} \right) \left(\frac{\partial y_{ci}}{\partial x_k} \right) \right], \quad (2-4)$$

where x_j and x_k are the refinable parameters. This matrix is an m by m matrix where m is the total number of refinable parameters. The non-linearity of the residual function means the change in the refinable parameters must be found following an iterative procedure and the change at each iteration is given by

$$\Delta x_k = \sum_j M_{jk}^{-1} \frac{\partial S_y}{\partial x_k}. \quad (2-5)$$

After each iteration the change in the refinable parameter is added to the initial value and the procedure is continued until a minimum has been found. Care has to be taken to ensure the minimum reached is a global minimum and not a local one. This requires the starting position of the refinement to be sufficiently close to the correct model.

A set of R-values similar to those used in single-crystal refinement have been developed for use in Rietveld refinements to determine how well the calculated structure has fitted the observed data. The commonly used R-values have been listed in table 2-1, where I_{oK} is the measured intensity of the k th Bragg peak and I_{cK} is the calculated intensity of the K th Bragg peak. The R_{wp} is the most meaningful of the R-values because the numerator is the residual being minimised and provides a good measure of the progress and quality of a refinement.

2.1.3.1 Refinable parameters

There are two types of refinable parameters in Rietveld refinement: those that describe the experimental setup and those that are sample specific. The instrumental variables include the geometry of the diffractometer, the incident beam properties and the detector effects. These are variables that should be pre-determined and fixed to the correct value during refinements. The two main parameters that need to be determined are the sample-height error and the zero-offset. A method to determine the correct zero-offset of a powder diffractometer using a standard reference material, such as CeO_2 , was developed by O'Connor et al [5]. The sample-height error and zero-offset both

Table 2-1 Definitions of the goodness-of-fit parameters for Rietveld refinement. M is the number of steps, P is the number of refinable parameters, I_{oK} is the measured intensity of the K th Bragg peak and I_{cK} is the calculated intensity of the K th Bragg peak.

Parameter	Definition
R-pattern	$R_p = \sqrt{\frac{\sum y_{oi} - y_{ci} }{\sum y_{oi} - y_{bi} }}$
R-weighted pattern	$R_{wp} = \sqrt{\frac{\sum w_i (y_{oi} - y_{ci})^2}{\sum w_i (y_{oi} - y_{bi})^2}}$
R-expected	$R_{exp} = \sqrt{\frac{M-P}{\sum w_i (y_{oi} - y_{bi})^2}}$
Goodness of fit	$GOF = \chi^2 = \sqrt{\frac{\sum w_i (y_{oi} - y_{ci})^2}{M-P}}$
R-Bragg	$R_{Bragg} = \frac{\sum I_{oK} - I_{cK} }{\sum I_{oK}}$

affect the 2θ position of the Bragg peaks and because of this are highly correlated during a refinement. By determining the correct zero-offset using the reference material, the height offset can be refined while keeping the zero-error fixed. The change in the sample height results in errors in the 2θ position and intensity of the measured Bragg peaks. The optics of the diffractometer are optimised for a specific sample height and the effects of changing this are shown in figure 2-3. These effects are taken into account in Rietveld refinement programs, which apply corrections to both the peak intensity and position. Sample variables consist of those modelling the Bragg reflections and a polynomial to model the background profile. A range of variables affect the size and shape of the Bragg peaks and these will be discussed in detail.

2.1.3.2 Peak shapes

A range of different peak shapes have been used to fit the measured Bragg peaks and the performance of these has been investigated by Young and Wiles [6]. The commonly used profiles are listed in table 2-2 [7]. The majority of peak shapes use a combination of Lorentzian and Gaussian profiles, producing a profile with a shape between the two. The split-Pearson VII provided the best fit to the Bragg peaks measured using powder XRD. The Pearson VII profile becomes a Lorentzian when $m = 1$ and a Gaussian as $m \rightarrow \infty$. The use of a split-profile allows the two sides of a Bragg peak to be fitted

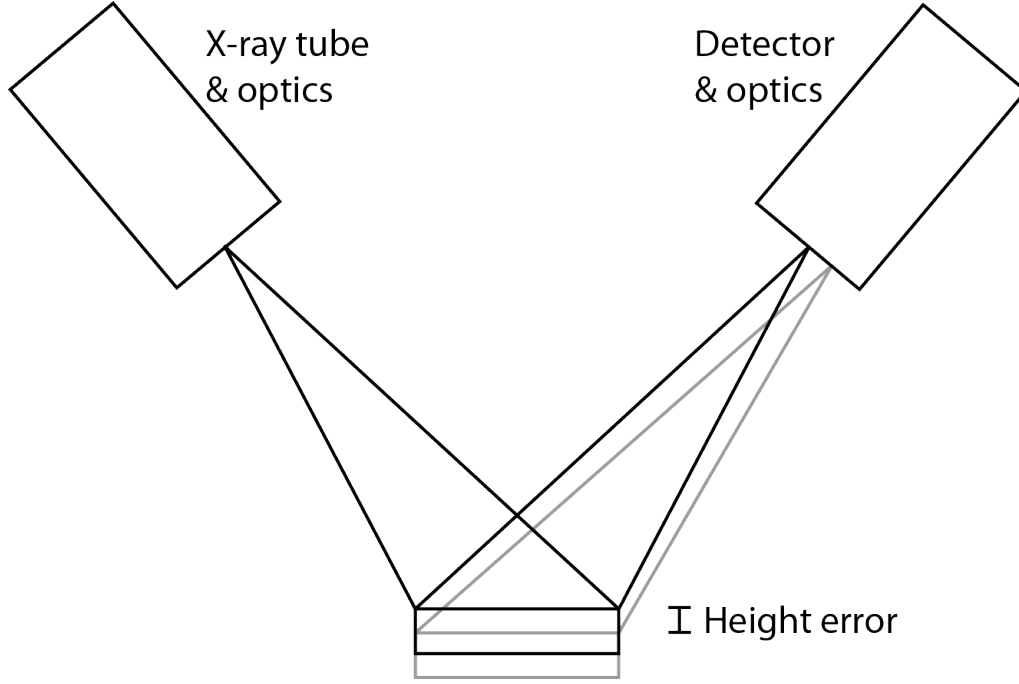


Figure 2-3 Schematic diagram showing illustrating the effect of sample height on the diffracted beam.

individually to model their asymmetry. The neutron diffraction data was fitted best by the modified Thompson-Cox-Hastings psuedo-Voigt (TCHZ), which can be varied between a Lorentzian and Gaussian shape using the mixing parameter η [8].

The Bragg peak's shape and FWHM varies as a function of 2θ and can be modelled with analytical expressions containing refinable parameters. The expressions for controlling the shape and width of the Pearson VII and TCHZ peaks are listed in table 2-3.

2.1.3.3 Preferred orientation

If the crystallites in a powdered sample are not randomly oriented there is a deviation of the Bragg peak intensities from their natural values. This effect is called preferred orientation and is treated in this work using the method of symmetrized harmonics developed by Jarvinen [9]. The effect of the preferred orientation on a Bragg peak is given by

$$P(K, \alpha) = \sum_{ij} C_{ij} Y_{ij}(\theta_K, \psi_K) P_i(\cos \alpha), \quad (2-6)$$

where C_{ij} are adjustable parameters, Y^{ij} are the symmetrized harmonics, (θ_K, ψ_K)

Table 2-2 Peak functions used in Rietveld refinement.

Peak function	Definition
Gaussian	$G(x) = \left(\frac{2\sqrt{\ln(2)/\pi}}{FWHM} \right) \exp\left(\frac{-4\ln(2)x^2}{FWHM^2} \right)$
Lorentzian	$L(x) = \left(\frac{2/\pi}{FWHM} \right) / \left(\frac{1+4x^2}{FWHM^2} \right)$
Pseudovoigt TCHZ	$F(x) = \eta L(x) + (1 - \eta)G(x)$
Split PearsonVII	$PVII_l = \left(1 + \left((2^{-ml} - 1) / wl^2 \right) x^2 \right)^{-ml} / N$
	$PVII_r = \left(1 + \left((2^{-mr} - 1) / wr^2 \right) x^2 \right)^{-mr} / N$
	$N = (1/2) \left[\frac{\Gamma(ml-1/2)}{\Gamma(ml) \sqrt{((2^{-ml}-1)/wl^2)}} + \frac{\Gamma(mr-1/2)}{\Gamma(mr) \sqrt{((2^{-mr}-1)/wr^2)}} \right]$
	$FWHM = wl + wr$

Table 2-3 Refinable FWHM expressions.

Peak function	width parameters
	$w_{l,r} = wa + wb \tan \theta + wc / \cos \theta$
Split PearsonVII	$m_{l,r} = 0.6 + ma + mb \tan \theta + mc / \cos \theta$
	wa, wb, wc, ma, mb, mc are refinable parameters
TCHZ	$FWHM = \left(\Gamma_G^5 + A\Gamma_G^4\Gamma_L + B\Gamma_G^3\Gamma_L^2 + C\Gamma_G^2\Gamma_L^3 + D\Gamma_G\Gamma_L^4 + \Gamma_L^5 \right)^{0.2}$
	$A = 2.69269, B = 2.42843, C = 4.47163, D = 0.07842$
	$\Gamma_G = \left[U \tan^2 \theta + V \tan \theta + W + Z / \cos^2 \theta + (1 - \zeta) \Gamma_a^2 \right]^{0.5}$
	$\Gamma_L = X \tan \theta + Y / \cos \theta + \zeta \Gamma_a$
	U, V, W, X, Y, Z are refinable parameters
	$\eta = E (\Gamma_L / FWHM) - F (\Gamma_L / FWHM)^2 + G (\Gamma_L / FWHM)^3$
	$E = 1.33603, F = 0.47719, G = 0.1116$

Table 2-4 S_{HKL} restrictions for trigonal crystal systems in a hexagonal setting.

Crystal system	Anisotropic strain parameters
Trigonal (Hexagonal setting)	$S_{400} = S_{040} = S_{310}/2 = S_{130}/2 = S_{220}/3$
	$S_{202} = S_{022} = S_{112}$
	S_{004}
	$S_{301}/2 = -S_{031}/2 = S_{211}/3 = -S_{121}/3$

are the spherical coordinates of the normal to the (hkl) plane, $P_i(\cos \alpha)$ is a Legendre polynomial and α is the angle between the diffraction vector and the polar axis. In the Bragg-Brentano geometry $\alpha = 0$ and $P_i(\cos \alpha) = 1$.

2.1.3.4 Anisotropic peak broadening

The effects of anisotropic peak broadening are included using the method developed by Stephens which allows a distribution of the reciprocal lattice variables for the crystallites in the powder [10]. The matrix $M_K = 1/d^2$ is used to model the effects of the distribution. It is assumed that the distribution of the reciprocal lattice variables in the crystallites is Gaussian and gives a variance in M_K of

$$\sigma^2(M_K) = \sum_{HKL} S_{HKL} h^H k^K l^L, \quad (2-7)$$

where the terms in S_{HKL} are defined for $H + K + L = 4$. This results in 15 parameters to model the effects of anisotropic peak broadening for a triclinic case. The symmetry of the crystal system restricts the possible values of S_{HKL} and a trigonal crystal with hexagonal coordinates will have values according to table 2-4.

Using the Bragg equation, the contribution of the anisotropic peak broadening is given by

$$\Gamma_a = \left[\sigma^2(M_K) \right]^{1/2} \tan \theta / M_K. \quad (2-8)$$

The anisotropic broadening terms have been included in the equations to calculate the FWHM of the TCHZ peak shape in table 2-3, where the parameter ζ has been introduced to control the Lorentzian or Gaussian shape of the anisotropic broadening.

2.1.4 Single-crystal structure refinement

A range of structure solution methods are available to use on single-crystal diffraction measurements and detailed descriptions of these are available in a range of textbooks [1, 11]. These methods were not required for analysis of LNT structures because the previously determined structures of LN and LT provide an adequate starting point to refine the structure directly. The refinement program used in this thesis is SHELX, which was developed by Sheldrick [12].

Single-crystal diffraction measurements record the intensity of the Bragg reflections and before refining the structure in SHELX the measured data has a range of corrections applied to it. Reflections can be discarded if they do not follow the Laue symmetry or should be systematically absent. The effects of absorption are also taken into account, following the analytical method developed by Clark and Reid [13]. The absorption correction is given by the transmission factor,

$$T = 1/V \int_V \exp(-\mu L) dV, \quad (2-9)$$

where μ is the absorption coefficient in cm^{-1} , L is the total path length of scattered X-rays in cm and V is the crystal volume in cm^3 , subdivided into Howells polyhedra. Each Howells polyhedra is formed such that the incident and scattered beams both enter and exit from a single face.

The corrected intensities (F_o^2) of each specific Bragg peak, along with the h , k and l values provide the input for SHELX. The minimised quantity in the least-squares fitting is the difference between the measured and calculated F^2 values. The quality of the refinement is given by a series of R-factors shown in table 2-5. The R_{int} and R_σ values provide information about the merging (i.e., the averaging of equivalent reflections) of the measured data before a refinement. The R_{obs} , $wR2$ and GOF are used to assess how well the refined structure matches the measured data, with the R_{obs} value commonly quoted in the literature.

Table 2-5 Definitions of the goodness-of-fit parameters for single-crystal refinement.

Parameter	Definition
R-internal	$R_{int} = \frac{\sum F_{oi}^2 - \langle F_{ci}^2 \rangle }{\sum F_{oi}^2}$
R-sigma	$R_{\sigma} = \frac{\sum \sigma F_{oi}^2}{\sum F_{oi}^2}$
R-observed	$R_{obs} = \frac{\sum F_{oi} - F_{ci} }{\sum F_{oi} }$
R-weighted	$wR2 = \sqrt{\frac{\sum w(F_{oi}^2 - F_{ci}^2)^2}{\sum w(F_o^2)^2}}$
Goodness of fit	$GOF = \chi^2 = \sqrt{\frac{\sum w_i(F_{oi}^2 - F_{ci}^2)^2}{M-P}}$

2.2 Birefringence measurements

2.2.1 Optical theory

The transmission of two orthogonally polarised light waves through a uniaxial crystal results in a phase difference δ between the two waves. This phase difference is given by

$$\delta = \frac{2\pi}{\lambda} \Delta n L, \quad (2-10)$$

where λ is the wavelength of the light and L is the thickness of the material.

2.2.2 Rotating polariser method

The method of measuring the birefringence in this thesis is the rotating polariser method, the setup of this method is shown in figure 2-4. This method was developed by Wood et al and was an improvement on previous methods by making multiple measurements at different polariser (or analyser) angles to form each image [14]. Monochromatic light is produced by the combination of a white-light source and a wavelength-filter, which then passes through the rotating polariser. The polarised light then travels through the sample before reaching the analyser. The analyser consists of a quarter wave plate followed

by a linear polariser and the measured intensity of this system is given by

$$I = \frac{1}{2}I_0 [1 + \sin 2(\omega\tau - \phi) \sin \delta], \quad (2-11)$$

where ω is the frequency of rotation of the polariser and τ is the time. The angle the polariser rotates through in a given time is given by $\omega\tau$. This equation can be expressed as

$$I = \frac{1}{2}I_0 + \frac{1}{2}I_0 \sin \delta \cos 2\phi \sin 2\omega\tau - \frac{1}{2}I_0 \sin \delta \sin 2\phi \cos 2\omega\tau, \quad (2-12)$$

and solved using repeated measurements of the intensity with the polariser at different angles. Using a least-squares fitting technique, I_0 , ϕ and $|\sin \delta|$ can be calculated [15]. The Metripol system used for these measurements is equipped with a CCD camera comprised of a 640 by 800 pixel array. Equation 2-12 can be solved for each pixel to produce 640 by 800 pixel images of the I_0 , ϕ and $|\sin \delta|$.

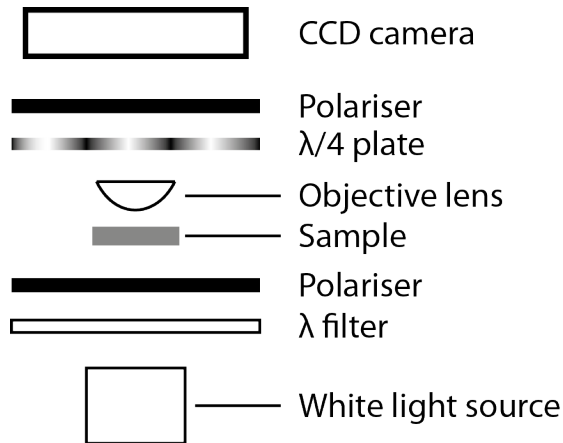


Figure 2-4 The experimental setup of the Metripol system. Monochromatic light passes through a rotating polariser before reaching the sample. It then passes through an analyser, which consists of a quarter wave plate followed by a polariser before reaching the detector.

The measured $|\sin \delta|$ signal for a crystal which has a linear change in birefringence in response to temperature is shown in figure 2-5. The birefringence is zero when the temperature is 100 °C and this corresponds to a trough in the measured $|\sin \delta|$, which oscillates between 0 and 1, with the peaks and troughs corresponding to a δ of $(2n + 1)\pi/2$ and $n\pi$, respectively.

In general, a separate measurement of the absolute birefringence is used to determine the correct zero-birefringence point, however, the rotating polariser technique can easily be used to determine the zero-birefringence point on materials that have a small

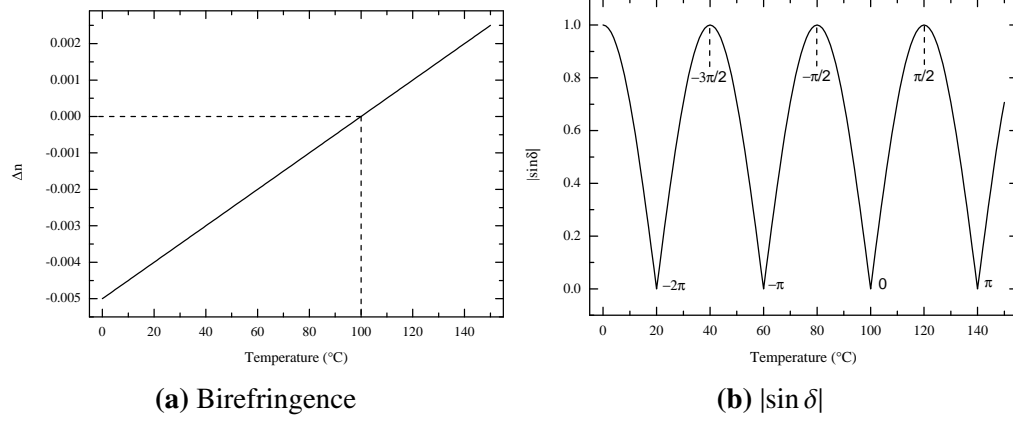


Figure 2-5 In (a) a linearly increasing birefringence as a function of temperature and (b) the $|\sin \delta|$ that would be measured by the Metripol system. Values of δ for each peak and trough are labelled in (b) and the zero-birefringence temperature by the dashed line in (a).

variation in birefringence as a function of wavelength. The zero-birefringence trough in the measured $|\sin \delta|$ signal will be at the same temperature in measurements made with different wavelengths of light, whereas the troughs at $n\pi$ will be in different positions due to the dependence of δ on the wavelength of light used.

2.3 Second harmonic generation

2.3.1 Nonlinear optics

A nonlinear optical effect occurs when the optical properties of a material are affected by the light propagating within. One of the possible nonlinear optical effects is second-harmonic generation, which was discovered by Franken et al [16] following the demonstration of a working laser by Maiman in 1960 [17]. The introduction of the laser provided a high-intensity source of coherent light, which allowed observable nonlinear optical effects to be measured for the first time. In linear optics the induced polarisation in the material is linearly dependent upon the electric field strength and is given by

$$\mathbf{P}(t) = P_0 + \epsilon_0 \chi^{(1)} \mathbf{E}(t), \quad (2-13)$$

where P_0 is the spontaneous polarisation for a ferroelectric material, $\chi^{(1)}$ is the linear susceptibility [18]. The nonlinear response can be described by expressing the

polarisation as a Taylor series in the field strength, this gives

$$\mathbf{P}(t) = P_0 + \epsilon_0 \left(\chi^{(1)} \mathbf{E}(t) + \chi^{(2)} \mathbf{E}^2(t) + \chi^{(3)} \mathbf{E}^3(t) + \dots \right), \quad (2-14)$$

$\chi^{(2)}$ and $\chi^{(3)}$ are the second- and third-order nonlinear optical susceptibilities, respectively. In this work we will only take into account the nonlinear effects caused by the second-order optical susceptibility. Second-order nonlinear effects are only possible in non-centrosymmetric crystal systems. In a centrosymmetric crystal system a reversal of the optical electric field from \mathbf{E} to $-\mathbf{E}$ must also result in a reversal of the polarisation to $-\mathbf{P}$. This is not possible in the even terms of the Taylor expanded series and means for centrosymmetric crystal systems, the even-order susceptibilities are zero.

The effects of the second-order susceptibility can be calculated by applying light with an electric field given by $\mathbf{E}(t) = \epsilon_0 (\mathbf{E}_0 e^{-i\omega t} + \mathbf{E}_0^* e^{i\omega t})$. The induced polarisation is

$$\mathbf{P}(t) = P_0 + \epsilon_0 \chi^{(2)} \left(\mathbf{E}_0^2 e^{-2i\omega t} + 2|\mathbf{E}_0|^2 + \mathbf{E}_0^{*2} e^{2i\omega t} \right). \quad (2-15)$$

This produces two nonlinear optical effects: second-harmonic generation characterised by $\mathbf{P}(2\omega) = \chi^2 \mathbf{E}_0^2 e^{-2i\omega t}$ and optical rectification given by $\mathbf{P}(0) = 2\chi^2 |\mathbf{E}_0|^2$. In second-harmonic generation a polarisation is induced with twice the frequency of the applied electric field. This polarisation will in turn produce an electric field with a frequency twice that of the input field. Optical rectification results in the generation of a static electric field inside a nonlinear material.

The generation of a second-harmonic signal can be used as way to determine whether or not a material is centrosymmetric. The experimental setup for these measurements consists of a Nd:YAG laser ($\lambda = 1.064 \mu\text{m}$) and a furnace to allow measurements up to 750°C . The incoming laser beam is split to provide a measurement of the incoming laser intensity with a photodiode and a separate beam to interact with the sample. A second harmonic signal of 532 nm is emitted isotropically by the sample and a photomultiplier tube (PMT) placed behind an interference filter and a 532 nm filter is used to measure its intensity.

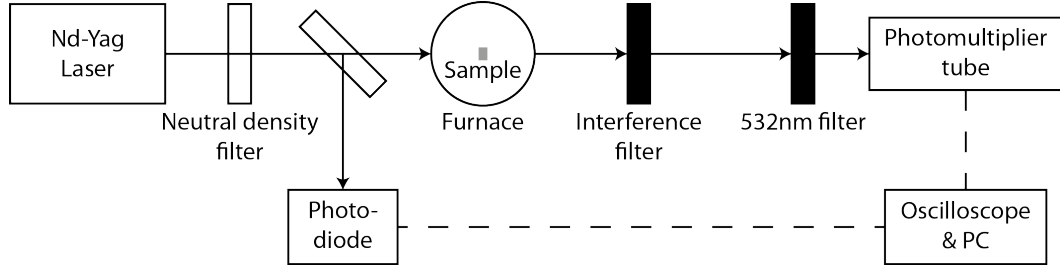


Figure 2-6 The experimental setup for SHG measurements. The 1064 nm laser is split with one beam going to the sample and the other to a photodiode to measure the intensity. Following the sample an interference filter and 532 nm filter ensure only the SHG signal is measured by the PMT.

2.4 Density functional theory

We require a solution to the quantum many body problem, the Hamiltonian for this system is:

$$\begin{aligned} \hat{H} = & -\frac{\hbar^2}{2} \sum_i \frac{\nabla_{\mathbf{R}_i}^2}{M_i} - \frac{\hbar^2}{2} \sum_i \frac{\nabla_{\mathbf{r}_i}^2}{m_e} - \frac{1}{4\pi\epsilon_0} \sum_{i,j} \frac{e^2 Z_i}{|\mathbf{R}_i - \mathbf{r}_j|} \\ & + \frac{1}{8\pi\epsilon_0} \sum_{i \neq j} \frac{e^2}{|\mathbf{r}_i - \mathbf{r}_j|} + \frac{1}{8\pi\epsilon_0} \sum_{i \neq j} \frac{e^2 Z_i Z_j}{|\mathbf{R}_i - \mathbf{R}_j|} \end{aligned} \quad (2-16)$$

The mass of the nucleus is M_i and the mass of an electron is m_e and they are at positions \mathbf{R}_i and \mathbf{r}_i respectively. The first term is the kinetic energy operator for the nuclei and the second for the electrons. The other terms are due to the Coulomb interaction between the electrons and nuclei.

2.4.1 The Born-Oppenheimer approximation

The nuclei are considered to be static in space and the electrons are in instantaneous equilibrium around them [19]. This simplifies the system, as the kinetic energy of the nuclei become zero, which makes the first term zero in equation 2-16. The static nature of the nuclei also reduces the Coulomb interaction between them to a constant. The resulting Hamiltonian of the system is now comprised of terms for the kinetic energy of the electron gas, the potential energy due to the electron-electron interactions and the potential energy of the electrons in the potential of the nuclei:

$$\hat{H} = \hat{T} + \hat{V} + \hat{V}_{ext}. \quad (2-17)$$

2.4.2 The Kohn-Sham equations

Hohenberg and Kohn [20] suggested that the total energy of the system is given exactly as a functional of the ground state electron density, ρ such that

$$\langle \Psi | \hat{H} | \Psi \rangle = E[\rho] . \quad (2-18)$$

The exact form of the functional is unknown and DFT requires accurate approximations to enable calculations. This was simplified by Kohn and Sham who introduced the exchange-correlation functional, E_{xc} , which is the difference between the total energy calculated using the Hartree-Fock method ($E_H[\rho]$) and exact total energy. The equation for the total energy then becomes

$$E[\rho] = E_k[\rho] + E_H[\rho] + E_{xc}[\rho] + E_{ext}[\rho] , \quad (2-19)$$

where, $E_k[\rho]$ is the single-particle kinetic energy and $E_{ext}[\rho]$ is the energy due to the external potential of the nuclei. This approach then requires approximations for the exchange-correlation functional; the two common ones are the LDA and the GGA. In the LDA, the electron density is divided into infinitesimally small volumes with constant density and has the same exchange-correlation energy as an identical volume filled with a homogeneous electron gas. The exchange-correlation functional is then given by

$$E_{xc}[\rho] = \int \rho(\mathbf{r}) \epsilon_{xc}(\rho(\mathbf{r})) d\mathbf{r} . \quad (2-20)$$

In the GGA the $\epsilon_{xc}(\rho)$ is now also a function of the magnitude of the gradient of the density, $\epsilon_{xc}(\rho, |\nabla\rho|)$.

2.4.3 Solving the Kohn-Sham equations

The ground state energy can now be determined by solving a series of non-interacting single-particle equations. The Kohn-Sham equation is

$$\hat{H}_{KS} \phi_i(\mathbf{r}) = (\hat{T}_0 + \hat{V}_H + \hat{V}_{xc} + \hat{V}_{ext}) \phi_i(\mathbf{r}) = \epsilon_i \phi_i(\mathbf{r}) , \quad (2-21)$$

where $\phi_i(\mathbf{r})$ are single-particle Kohn-Sham orbitals, \hat{T}_0 is the kinetic energy operator, \hat{V}_H is the Hartree potential, \hat{V}_{xc} is the exchange-correlation potential, \hat{V}_{ext} is the

Coulomb potential due to the nuclei and ϵ_i are the Kohn-Sham eigenvalues. The ground-state energy of an N-electron system is given by

$$\rho(\mathbf{r}) = \sum_{i=1}^N \phi_i(\mathbf{r})^* \phi_i(\mathbf{r}), \quad (2-22)$$

where $\phi_i(r)$ are the N lowest-energy solutions of the Kohn-Sham equation. Both \hat{V}_H and \hat{V}_{xc} depend on ρ , this means that a self-consistent solution to equations 2-21 and 2-22 is required for a calculation. This requires a solution to the Kohn-Sham equation to produce Kohn-Sham orbitals that also reproduce the initial ρ . The iterative procedure for such a calculation is shown in figure 2-7. In order to solve these equations a basis set ϕ_i is introduced and the coefficients c_n are found such that the Kohn-Sham orbitals can be expressed in the basis set:

$$\phi_i = \sum_n c_n \phi_n. \quad (2-23)$$

The choice of basis is determined by the computational capabilities; a larger and more complex basis set will result in a more accurate calculation but at the cost of increased computational time required.

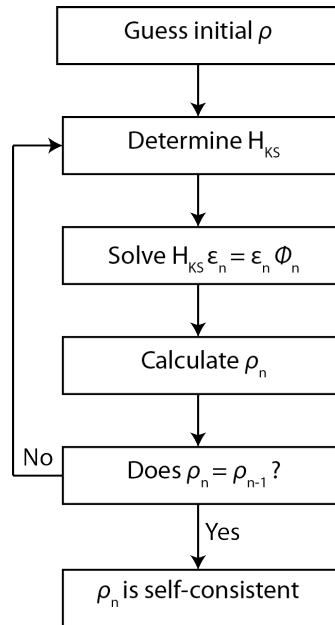


Figure 2-7 Flow chart describing the iterative procedure for self-consistent solutions of Kohn-Sham equations, based on figure 1.1 in Cottenier [21].

2.4.4 The full potential LAPW method

The linearised augmented plane wave (LAPW) method, as implemented in the WIEN2k code makes use of a two part basis set. This consists of atom-like wavefunctions close to the atomic nucleus and plane waves between. A detailed introduction to the LAPW method has been given by Cottenier [21] and Singh [22] and a brief overview will be given in this thesis.

The unit cell is divided into two regions: non-overlapping spheres at the atomic positions and the interstitial region that separates them. Inside the atomic sphere the basis set consists of a linear combination of radial functions multiplied by spherical harmonics

$$\phi_{\mathbf{k}_n} = \sum_{lm} [A_{lm,\mathbf{k}_n} u_l(\mathbf{r}, E_l) + B_{lm} \dot{u}_l(\mathbf{r}, E_l)] Y_{lm}(\mathbf{r}) , \quad (2-24)$$

where $u_l(\mathbf{r}, E_l)$ is the solution to the radial Schrödinger equation for energy E_l and $\dot{u}_l(\mathbf{r}, E_l)$ is the energy derivative of u_l evaluated at energy E_l . A_{lm} and B_{lm} are coefficients that are determined by requiring the basis functions between the sphere and the interstitial region to have the same value and gradient at the interface. \mathbf{k}_n is given by $\mathbf{k}_n = \mathbf{k} + \mathbf{K}_n$, where \mathbf{k} is the wave vector inside the first Brillouin zone and \mathbf{K}_n are the reciprocal lattice vectors. In the WIEN2k code the cutoff parameter for the basis set is $R_{MT}K_{MAX}$, where R_{MT} is the smallest atomic sphere radius and K_{MAX} is the magnitude of the largest \mathbf{K}_n vector.

The interstitial region uses a plane wave basis set given by

$$\phi_{\mathbf{k}_n} = \frac{1}{\sqrt{\omega}} e^{i\mathbf{k}_n \cdot \mathbf{r}} . \quad (2-25)$$

A third basis set called a ‘local orbital’ (LO) can be added to improve the flexibility of the calculation and allow the treatment of semicore and valence states in one energy window. The LO is \mathbf{k}_n independent and consists of two radial functions at different energies and one energy derivative. The LO basis is given by

$$\phi_{lm}^{LO} = [A_{lm} u_l(\mathbf{r}, E_{1,l}) + B_{lm} \dot{u}_l(\mathbf{r}, E_{1,l}) + C_{lm} u_l(\mathbf{r}, E_{2,l})] Y_{lm}(\mathbf{r}) \quad (2-26)$$

where A_{lm} , B_{lm} and C_{lm} are determined such that ϕ_{lm}^{LO} has zero value and gradient at the sphere boundary.

In WIEN2k, the LAPW method is used concurrently with the APW+lo method to reduce the total computation time required. The APW+lo method is similar to LAPW and is used for atoms that have a small sphere size and can be used in conjunction with LO's in the same way as the LAPW method. The choice of LAPW, APW+lo and whether an LO is required is determined automatically by the WIEN2k code.

2.4.5 Optical properties from DFT calculations

An extension to the WIEN2k code was provided by Ambrosch-Draxl et al which allows the calculation of the linear optical properties of materials using the LAPW method. A detailed description of the method used for this is given by Ambrosch-Draxl and Sofo [23]. The optical response of the system to incoming light is calculated using the random phase approximation (RPA), giving an approximation to calculate the complex dielectric tensor. The refractive index can then be calculated from the dielectric tensor using

$$n_{\alpha\alpha}(\omega) = \sqrt{\frac{|\epsilon_{\alpha\alpha}(\omega)| + \text{Re}\epsilon_{\alpha\alpha}(\omega)}{2}}, \quad (2-27)$$

where $\epsilon_{\alpha\alpha}$ is the dielectric tensor, α is the direction in the crystal and ω is the frequency.

References

- [1] C. Giacovazzo, *Fundamentals of Crystallography* (Oxford University Press, Oxford, 2011).
- [2] H. M. Rietveld, *Acta Crystallographica* **22**, 151 (1967).
- [3] H. M. Rietveld, *Journal of Applied Crystallography* **2**, 65 (1969).
- [4] R. A. Young, *The Rietveld Method* (Oxford University Press, Oxford, 2002).
- [5] B. H. O'Connor, D. Y. Li, and B. A. Hunter, *Advances in X-ray Analysis* **44**, 96 (2001).
- [6] R. Young and D. Wiles, *Journal of Applied Crystallography* **15**, 430 (1982).
- [7] *Topas Academic Technical Reference V4.0* (2006).
- [8] P. Thompson, D. E. Cox, and J. B. Hastings, *Journal of Applied Crystallography* **20**, 79 (1987).
- [9] M. Järvinen, *Journal of Applied Crystallography* **26**, 525 (1993).
- [10] P. W. Stephens, *Journal of Applied Crystallography* **32**, 281 (1999).
- [11] J. P. Glusker and K. N. Trueblood, *Crystal structure analysis* (Oxford University Press, Oxford, 2010).
- [12] G. M. Sheldrick, *Acta Crystallographica* **A64**, 112 (2008).
- [13] R. C. Clark and J. S. Reid, *Acta Crystallographica* **A51**, 887 (1995).

- [14] I. G. Wood and A. M. Glazer, *Journal of Applied Crystallography* **13**, 217 (1980).
- [15] A. M. Glazer, J. G. Lewis, and W. Kaminsky, *Proceedings: Mathematical, Physical and Engineering Sciences* **452**, 2751 (1996).
- [16] P. A. Franken, A. E. Hill, C. W. Peters, and G. Weinreich, *Physical Review Letters* **7**, 118 (1961).
- [17] T. H. Maiman, *Nature* **187**, 493 (1960).
- [18] R. W. Boyd, *Nonlinear Optics* (Academic Press, San Diego, 2008).
- [19] M. Born and J. Oppenheimer, *Ann. Physik* **84**, 457 (1927).
- [20] P. Hohenberg and W. Kohn, *Physical Review* **155**, 864 (1964).
- [21] S. Cottenier, *Density Functional Theory and the family of (L) APW-methods: a step-by-step introduction* (freely available at <http://www.wien2k.at/reg-user/textbooks>, 2013), 2nd ed., ISBN 9789080721517.
- [22] D. J. Singh and L. Nordstrom, *Planewaves, pseudopotentials and the LAPW-method* (Springer Science, 2006), 2nd ed.
- [23] C. Ambrosch-Draxl and J. O. Sofo, *Computer Physics Communications* **175**, 1 (2006).

CHAPTER 3

Powder diffraction study of $\text{LiNb}_{1-x}\text{Ta}_x\text{O}_3$

3.1 Sample preparation

Powder samples of LNT were synthesised across the compositional range using a solid state sintering process. The raw materials used were Li_2CO_3 (99.9 %), Nb_2O_5 (99.999 %) and Ta_2O_5 (99.8 %). The powders were weighed in the correct stoichiometric ratio to produce a total mass of 15 g. The mixed powders were ball-milled in isopropanol with alumina balls for 20 h and then placed in a drying oven to remove the isopropanol. The dried powder was then sealed in a platinum crucible and sintered at 1160 °C for 130 h using a heating and cooling rate of 180 °C h⁻¹. A large sintering time ensured the complete reaction between the initial materials to produce phase-pure LNT powders. Following the sintering, the LNT powder was ground using an agate pestle and mortar. A range of samples across the full range from LN to LT with steps in composition of 10 mol % and samples every 2 mol % between LNT91 and LNT99 were produced.

3.2 Room-temperature X-ray powder diffraction

Room-temperature X-ray scans on the LNT powders were performed using the PANalytical X'Pert Pro MPD. Scans were between 5 and 135° in 2 θ with a step size of

0.0066° and a total measurement time of between 7 and 15 h. A 10 mm beam mask was used in conjunction with a sample holder that had a sample area with a diameter of 10 mm.

In order to make a visual comparison between the scans, they were scaled to make the intensity of the (012) peak at 23° in 2θ the same for all measurements. The XRD measurements on LNT powders across the composition range are shown in figure 3-1. PANalytical's Highscore Plus software was used to remove the background and correct for the change in positions of the peaks because of the sample displacement. The scaled measurements in figure 3-1 show a 50 % decrease in intensity for all peaks except the (012), (024), (036) and the (048) as the composition of the powder becomes less than 60 mol % LT. This decrease in intensity shows that the powdered samples have formed with a large amount of preferred orientation related to the [012] direction. Repeat grinding of the powders did not reduce the preferred orientation of the crystallites.

Rietveld refinement of the XRD data was performed using TOPAS Academic [1]. For each composition a consistent order in which the parameters were allowed to refine was followed:

1. Initial estimates for the lattice parameters and the Megaw parameters were provided based on the work of Abrahams et al [2, 3]. The Nb and Ta occupancies were set to the ratio of the initial material, the zero-offset was set to zero and the isotropic thermal parameters were set to one and not refined. In the first refinement only the lattice parameters, the peak shape and the sample displacement were allowed to vary.
2. This was followed by including the Megaw parameters and the simple axial model into the refinement.
3. The spherical harmonic parameters modelling the preferred orientation were then refined for samples with less than 70 mol % LT.
4. Next the Stephens parameters were included to model the anisotropic peak broadening.
5. The isotropic thermal parameters for the Li, Nb, Ta and O atoms were introduced into the refinement at the same time.

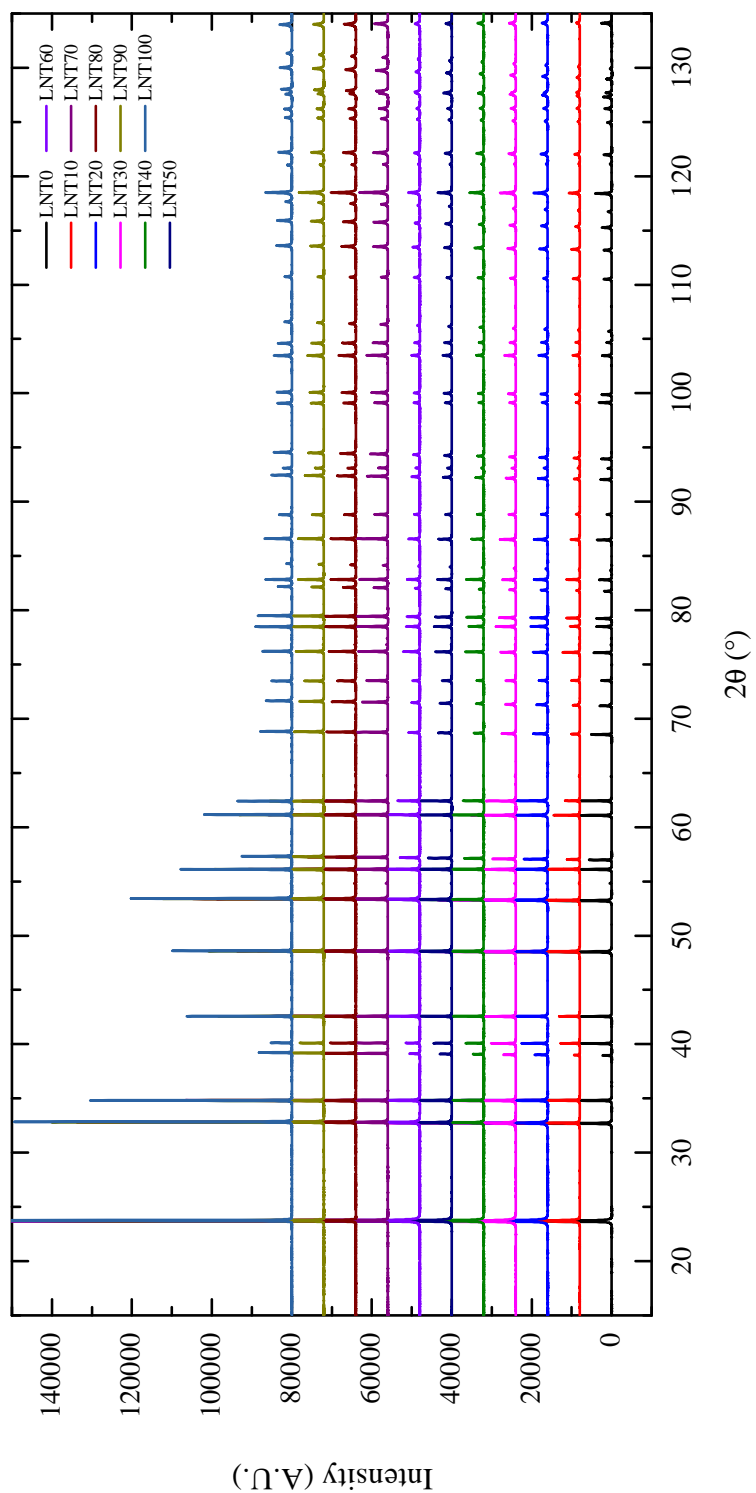


Figure 3-1 XRD measurements on LNT powders across the compositional range.

6. Finally the zero-offset of the diffractometer was included to check the stability of the refinement.

The use of the spherical harmonic terms to fit the preferred orientation allows its effect on each peak to be quantified. The scale factors applied to the peaks below 70° in 2θ for the samples with an LT content from 0 to 70 mol % are in table 3-1. The peaks with a scale factor greater than 1.45 are coloured red to show the common sets of reflections with a high degree of preferred orientation. For the samples with less than 70 mol % LT the dominant direction of the preferred orientation is the [012] as visible in scans plotted in figure 3-1. The samples with greater than 70 mol % LT do not have any preferred orientation and all crystallites are randomly distributed across all directions. The preferred orientation in the samples has a large effect on the intensity of the measured Bragg peaks, which affects the refinement of the Megaw parameters and the isotropic thermal parameters. The spherical harmonic terms to fit the preferred orientation are highly correlated with these parameters and cause the refined values to be unreliable.

The Rietveld refinement of the LNT powder with 100 mol % LT is shown in figure 3-2. The measured data are displayed using red diamonds and the fit to them is given by the black line. The difference between the measured and calculated intensity of the diffraction pattern is given by the green line and the Bragg peak positions for the refined structure are marked by the blue lines. A visual inspection of the calculated and measured patterns shows a good fit provided by the Rietveld refinement. The difference data show that the peak positions are correct and the peak shapes have been well described. The refinement of LNT100 has an R_p of 9.374 %, R_{wp} of 14.683 %, GOF of 1.489 and R_{Bragg} of 1.817 %. Similar values were returned by all refinements across the compositional range.

The preferred orientation within the samples does not affect the refinement of the lattice parameters because they are determined by the positions of the peaks and not their intensities. The refined a and c lattice parameters of the LNT powders as a function of the composition are shown in figure 3-3. The errors in the lattice parameters are from the estimated standard deviations (esd's) produced by Topas Academic during the refinement. The non-linear change in the a lattice parameter shows that LNT does not follow Vegard's law. This is consistent with previous measurements of the a lattice

Table 3-1 Scale factors applied to each Bragg peak in the Rietveld refinement by the spherical harmonics used to model the preferred orientation. The red text corresponds to a scale factor of 1.45 or greater.

h	k	l	Scale factor applied to peak as a function of LT content							
			0 %	10 %	20 %	30 %	40 %	50 %	60 %	70 %
0	1	2	1.65	2.31	1.46	1.84	1.95	1.58	1.72	0.98
1	0	4	1.01	0.82	0.90	0.82	0.77	0.84	0.84	0.95
1	1	0	1.04	1.00	0.93	0.89	0.88	0.92	0.99	1.01
0	0	6	0.68	0.59	0.85	0.79	0.85	0.84	0.66	0.97
1	1	3	0.93	1.01	1.01	0.97	1.06	0.98	1.01	1.05
2	0	2	0.83	0.71	0.90	0.86	0.85	0.97	0.85	0.99
0	2	4	1.65	2.31	1.46	1.84	1.95	1.58	1.72	0.98
1	1	6	1.03	0.89	0.98	0.94	0.90	0.95	0.94	1.00
2	1	1	0.93	0.86	0.91	0.85	0.83	0.92	0.88	1.01
1	2	2	1.03	1.16	1.04	1.07	1.10	1.02	1.10	1.02
0	1	8	0.78	0.63	0.90	0.81	0.73	0.87	0.80	0.97
2	1	4	0.83	0.74	0.91	0.83	0.88	0.89	0.91	1.04
0	3	0	0.78	0.60	0.90	0.85	0.76	0.92	0.74	0.99
1	2	5	1.23	1.58	1.21	1.35	1.45	1.24	1.30	1.02
2	0	8	1.01	0.82	0.90	0.82	0.77	0.84	0.84	0.95
1	0	10	0.78	0.75	0.89	0.80	0.79	0.87	0.71	0.94
1	1	9	0.93	0.80	0.94	0.85	0.77	0.90	0.85	0.97
2	2	0	1.04	1.00	0.93	0.89	0.88	0.92	0.99	1.01
2	1	7	0.93	0.69	0.90	0.83	0.83	0.85	0.89	1.02
3	0	6	1.65	2.31	1.46	1.84	1.95	1.58	1.72	0.98
0	3	6	0.93	0.66	0.88	0.86	0.86	0.87	0.99	1.01
2	2	3	0.93	1.02	0.97	0.92	0.97	0.94	1.00	1.03
1	3	1	0.93	0.87	0.95	0.94	0.89	0.94	0.93	1.01
3	1	2	0.86	0.76	0.90	0.83	0.81	0.93	0.82	1.00
1	2	8	1.24	1.33	1.15	1.23	1.24	1.17	1.19	1.01
0	2	10	1.04	0.92	1.03	1.01	0.90	1.03	1.03	0.99
1	3	4	1.17	1.51	1.18	1.33	1.39	1.19	1.31	1.01
0	0	12	0.68	0.59	0.85	0.79	0.85	0.84	0.66	0.97
3	1	5	0.84	0.72	0.90	0.83	0.87	0.91	0.91	1.02
2	2	6	0.93	1.01	1.01	0.97	1.06	0.98	1.01	1.05
0	4	2	0.93	0.94	1.02	1.08	1.02	1.03	1.01	1.00
2	1	10	0.98	0.78	0.92	0.83	0.78	0.86	0.85	0.98
4	0	4	0.83	0.71	0.90	0.86	0.85	0.97	0.85	0.99
1	1	12	0.84	0.74	0.91	0.81	0.74	0.88	0.78	0.96
1	3	7	1.40	1.88	1.32	1.55	1.66	1.38	1.47	1.01
3	2	1	1.00	0.94	0.92	0.87	0.86	0.92	0.94	1.01
2	3	2	1.01	1.03	0.97	0.94	0.94	0.94	1.02	1.02
1	2	11	1.09	1.00	1.04	1.03	0.95	1.04	1.03	0.99
3	1	8	0.90	0.64	0.88	0.82	0.83	0.84	0.92	1.02
2	2	9	1.01	0.95	1.00	0.98	1.01	0.98	0.99	1.03
3	2	4	0.89	0.89	0.93	0.85	0.90	0.92	0.92	1.03
4	1	0	0.86	0.71	0.91	0.86	0.79	0.92	0.81	1.00

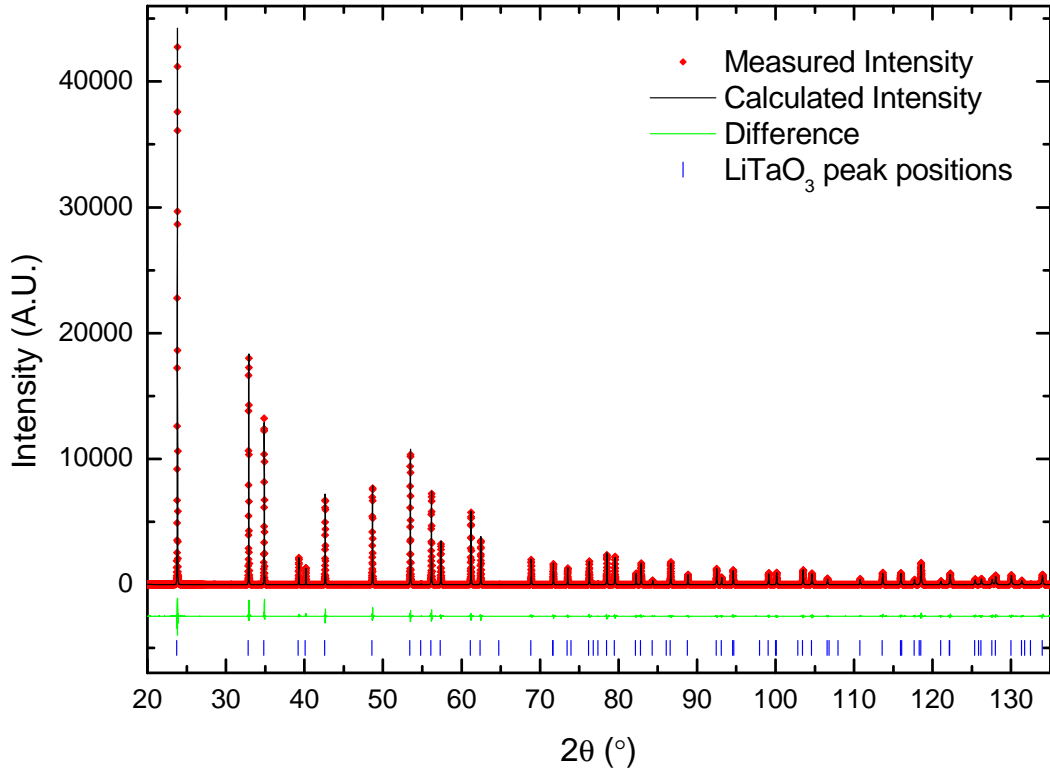


Figure 3-2 Rietveld refinement of LNT powder made with 100 % LT. The measured diffraction pattern is given by the red points, the calculated intensities by the black line and the difference between them by the green line. The blue lines give the positions of the Bragg peaks of the refined structure.

parameter made on samples of LNT. The red line shows a fit to the data using a bowing parameter to quantify the extent of the deviation from a linear trend. The bowing parameter is $-0.0036 \pm 0.0008 \text{ \AA}$, which agrees with the previously calculated value of $-0.003 \pm 0.003 \text{ \AA}$ [4]. The reduced error on this measurement is due to a larger number of samples used across the compositional range. The bowing parameter calculated from the fit to the c lattice parameters in figure 3-3b is $-0.009 \pm 0.002 \text{ \AA}$ which is less than the previously measured value of $-0.016 \pm 0.003 \text{ \AA}$ [4]. The difference between these two values is due to a greater number of samples at low-LT content in this study compared to the previous work.

For the samples with an LT content of 70 mol % and higher, which do not have preferred orientation, the atomic positions and the Megaw parameters calculated from them are refined. The Nb/Ta displacement increases as the amount of Nb increases and is shown in figure 3-4a. The Ta displacement for the stoichiometric powder was measured to be $0.198 \pm 0.004 \text{ \AA}$ which agrees with $0.20 \pm 0.01 \text{ \AA}$ calculated using neutron

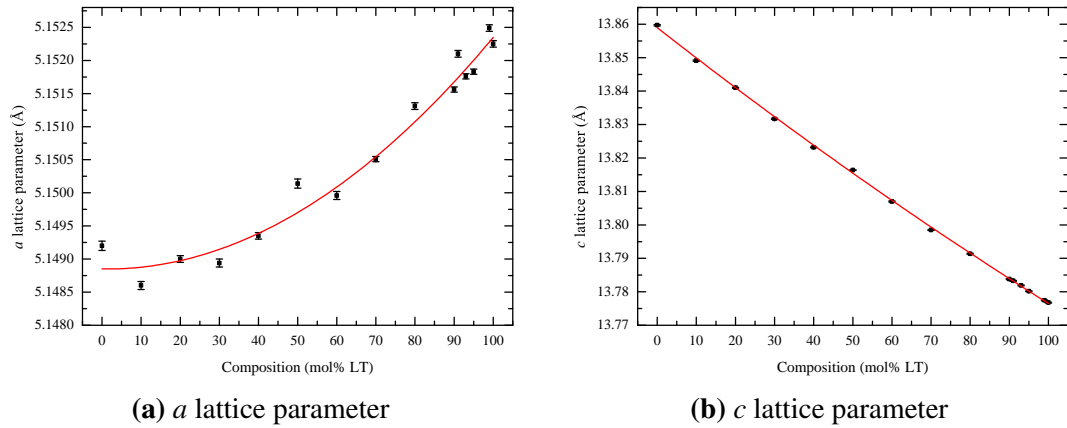


Figure 3-3 The (a) *a* and (b) *c* lattice parameters as a function of the LT content of the LNT powders. A quadratic fit using a bowing parameter is given by the red line. The errors are the esd's given by Topas Academic in the Rietveld refinement.

diffraction on a single crystal of SLT [3]. As the amount of LN is increased in the powders, the displacement of the Nb/Ta increases linearly attaining $0.240 \pm 0.002 \text{ Å}$ for LNT70. Applying a linear fit and extrapolating the line to LN, the displacement of an SLN sample is estimated to be 0.346 Å , which is considerably higher than the value of $0.27 \pm 0.01 \text{ Å}$ measured using neutron diffraction on an SLN crystal [5]. This suggests either the change in the Nb/Ta displacement is not linear across the compositional range or that the small range of measured values is too small to provide a reliable value for the gradient of the changing displacement.

The displacement of the Li in figure 3-4b shows a peak around LNT90 with a linear change above and below this. This trend and the refined values are unreliable because of the small scattering factor of X-rays by Li atoms. The esd's given by Topas academic are an underestimate of the errors in measuring Li positions using XRD, however the displacement for SLN is calculated to be $0.58 \pm 0.01 \text{ Å}$, which is consistent with the value of $0.60 \pm 0.02 \text{ Å}$ calculated with neutron diffraction [3].

The variation in the O octahedra as a function of the composition is measured using the distortion of the octahedra and the tilt angle. The refined octahedral distortion is plotted in figure 3-4c. All the measured values are negative with the majority of values scattered around -0.0028 and two samples; LNT70 and LNT99 have lower values of -0.0041 ± 0.0002 and -0.0041 ± 0.0002 , respectively. These are likely erroneous points and the distortion remains roughly constant across the compositional range in-

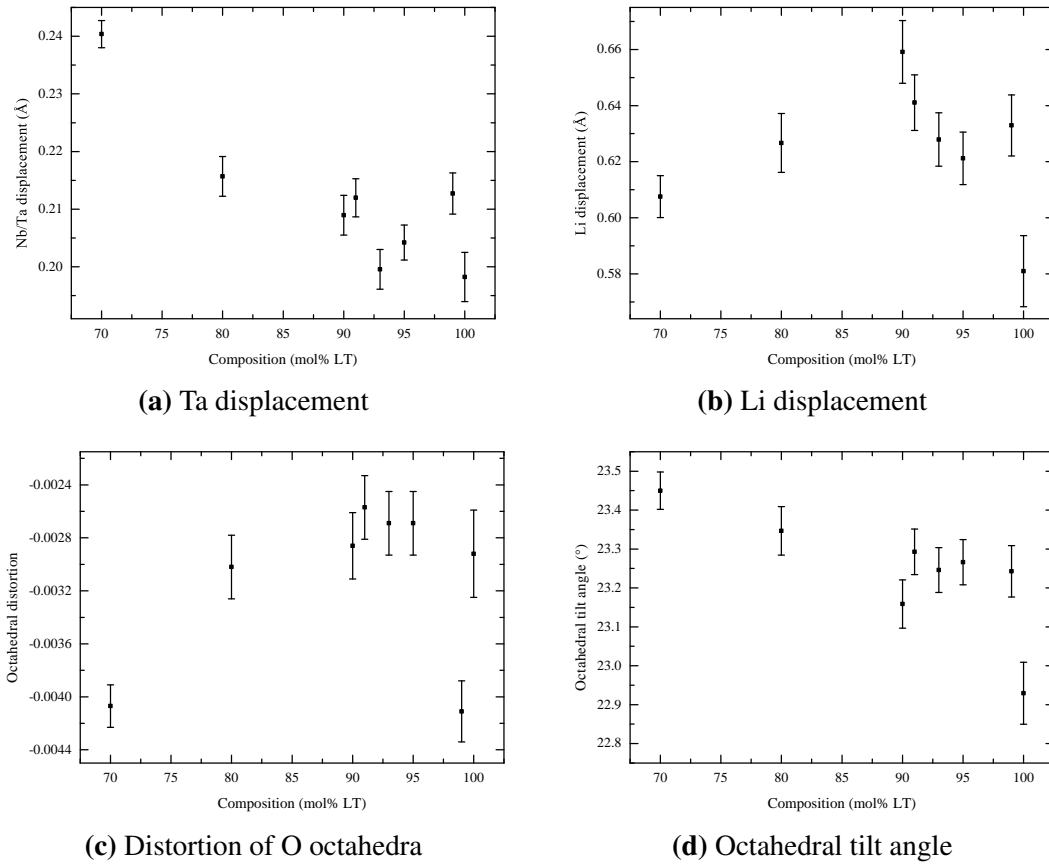


Figure 3-4 Parameters from Rietveld refinement of LNT powders with LT-content greater than 60 mol % LT. The (a) Ta displacement, (b) Li displacement, (c) octahedral distortion and (d) octahedral tilt angle are shown.

vestigated. The values measured on the single crystals of SLT and SLN are -0.0026 and -0.0028 respectively [3, 5]. The errors on the refined powder XRD values are of a similar size to the difference between these two values and confirms that the lower values are erroneous.

The tilt angle of the octahedra as a function of composition is plotted in figure 3-4d. The tilt of the SLT sample was measured to be $22.93 \pm 0.08^\circ$, which agrees well with the previously measured value on an SLT crystal of 22.9° [3]. As the amount of LN in the powder increases the tilt angle increases linearly attaining a value of $23.45 \pm 0.05^\circ$ for LNT70. The tilt measured on an SLN crystal by Abrahams et al was 23.1° , which suggests the octahedral tilt does not continue to increase linearly across the composition and a larger range of results are needed to understand the changing octahedral tilt between SLN and SLT [5].

3.3 High-temperature X-ray powder diffraction

For high-temperature runs, an Anton Paar HTK1200N oven was used in conjunction with the PANalytical MPD. Alumina sample holders, 16 mm in diameter and with a depth of either 4 or 8 mm were used depending on the amount of sample available. For all measurements the penetration depth of the X-rays into the powder was less than 4 mm and the measured diffraction patterns did not contain peaks from the alumina of the sample holders. A heating rate of 6°C min^{-1} was used and a 10 min dwell before each measurement to ensure a homogeneous temperature distribution throughout the sample. A typical measurement consisted of an initial scan at room temperature between 20 and 120° in 2θ with a total counting time of 3 h. This scan was then repeated every 40°C between 60 and 820°C for a total of 21 scans. The total time required was roughly 65 h and the counting time of the scans was varied slightly depending on how much time was available for the measurements.

Powder samples with compositions of 92, 94, 96, 98, 99 and 100 mol% LT were synthesised using the same method as in section 3.1. Rietveld refinements of the data were performed following the procedure given below:

1. Initial estimates for the room-temperature lattice parameters and Megaw parameters were calculated using the fitted data in section 3.1 and the previously refined parameters from the preceding temperature were used as the initial values for high-temperature scans. The Nb and Ta occupancies were set to the ratio of the initial materials, the zero offset was set to zero and the isotropic thermal parameters to one and not refined. An initial refinement allowing only the lattice parameters, the peak shape and the sample displacement to vary was performed.
2. The Megaw parameters and the simple axial model were then refined.
3. The isotropic thermal parameters for the Li, Nb, Ta and O atoms were included in the refinement.
4. The zero-offset of the diffractometer was then allowed to vary to check the stability of the refinement.

Anisotropic peak broadening parameters were not included in refinements of high-temperature scans because of the reduced intensity of the measured data. The inclusion

of the Stephens parameters did not improve the quality of the fit to the data and only increased the overall number of parameters in the refinement. The refinement of the scan at 25 °C on SLT had an R_p of 17.395 %, R_{wp} of 12.339 %, GOF of 1.41 and R_{Bragg} of 1.76 %. Similar values were attained for each sample at all temperatures measured.

3.3.1 Lattice parameters

The refined c lattice parameters as a function of temperature are shown in figure 3-5 with the black data below the phase transition fitted to a fourth-order polynomial and the red data above to a second-order polynomial. The c lattice parameter increases with increasing temperature above room temperature and reaches a maximum close to 400 °C for all compositions studied. Above this temperature it begins decreasing until the Curie point of the sample and increases in the paraelectric phase. This complicated variation in the c lattice parameter is due to the combination of the thermal expansion of the lattice with temperature and the decreasing displacement of the Ta atom from the centre of its oxygen octahedra. The displacement of the Ta atom from the refinements are plotted in figure 3-6 and the displacement decreases for all samples as the temperature increases. The data show a change in the gradient of the displacement between 300 and 500 °C coinciding with the peak in the c lattice parameter; the decrease in the Ta displacement results in a larger change in the size of the O octahedra than the thermal expansion of the lattice and the c lattice parameter decreases.

The refined a lattice parameters of the LNT100 sample are shown in figure 3-7a and have an almost linear increase with temperature. The data have been fitted with a linear trend and the residual between this fit and the data is plotted in figure 3-7b. The plot of the residual shows that the increase in the a lattice parameter is nonlinear below the paraelectric phase and the expansion is different above and below the phase transition. The black data points below the transition have been fitted by a fourth-order polynomial and the red data points by a second-order polynomial. The expansion of the a lattice parameter is determined by the oxygen octahedra; the combined changes in the tilt angle and increasing size of the octahedra contribute to produce the nearly linear increase.

The calculated octahedral tilt from the refined O positions is shown for each sample in figure 3-8. The tilt angle of the oxygen octahedra decreases with increasing tempera-

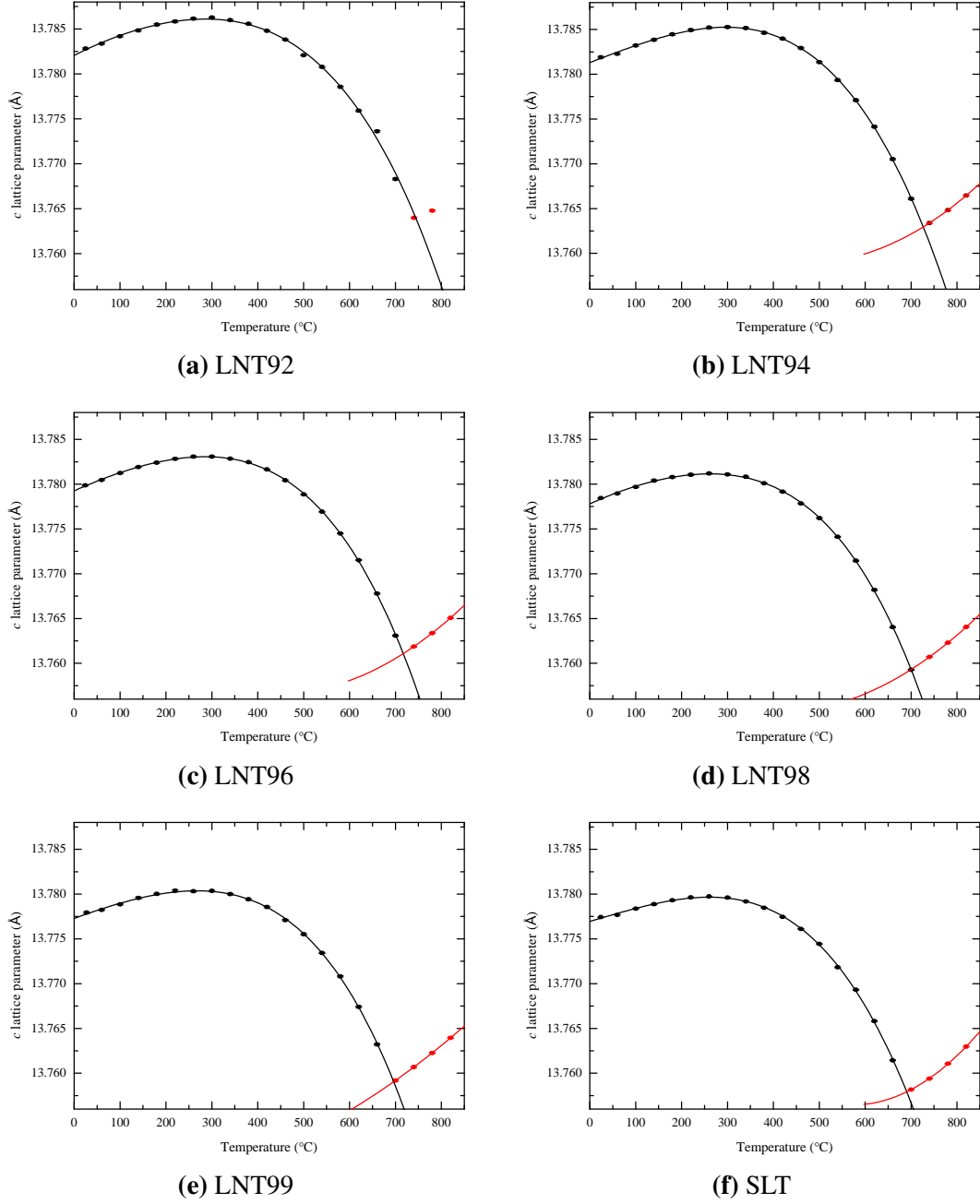


Figure 3-5 *c* lattice parameters as a function of temperature for Ta-rich LNT samples. Polynomial fits applied to the data above and below the phase transition are given by the red and black lines respectively.

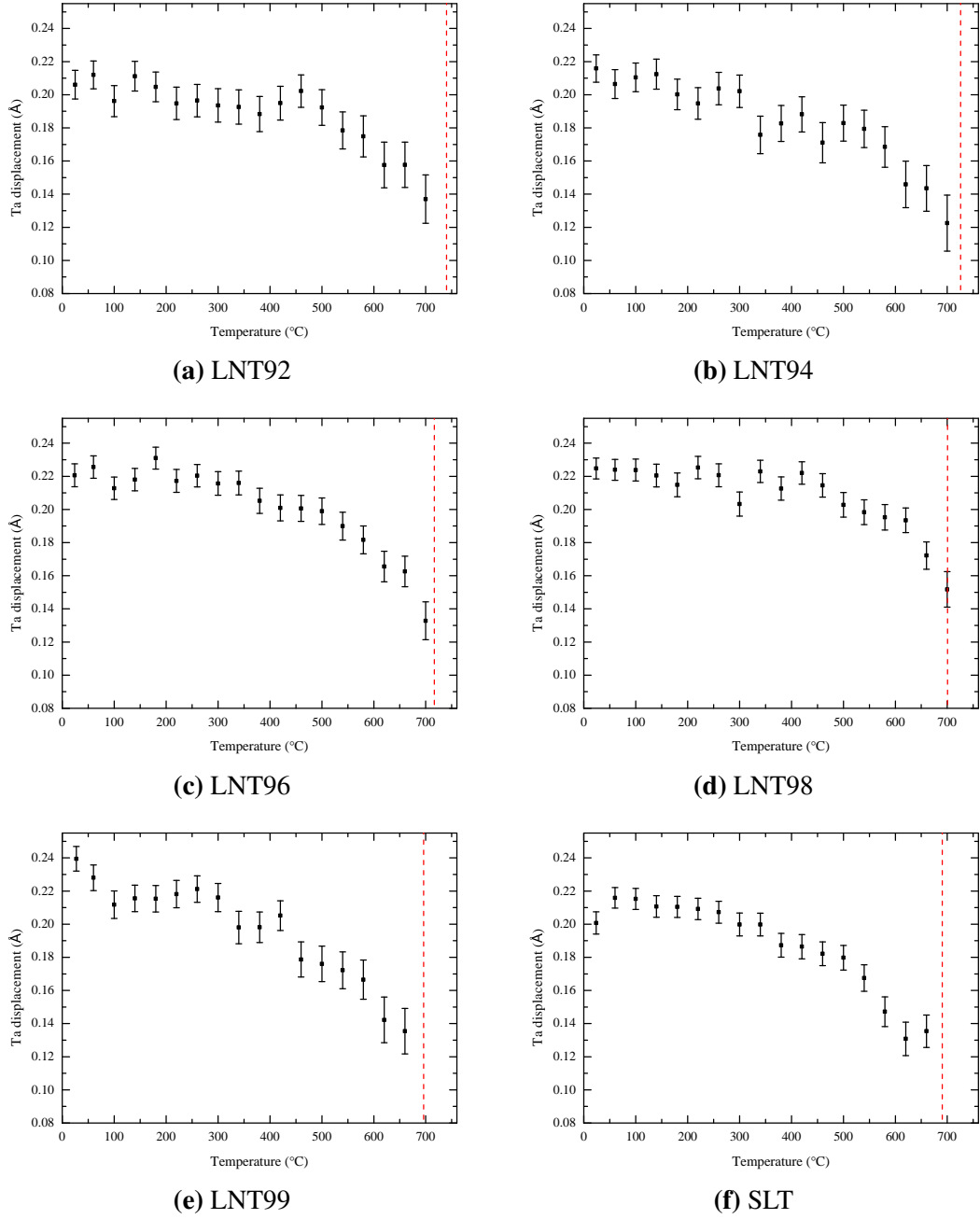


Figure 3-6 Ta displacement as a function of temperature for Ta-rich samples of LNT. The Curie temperature is given by the dashed red line.

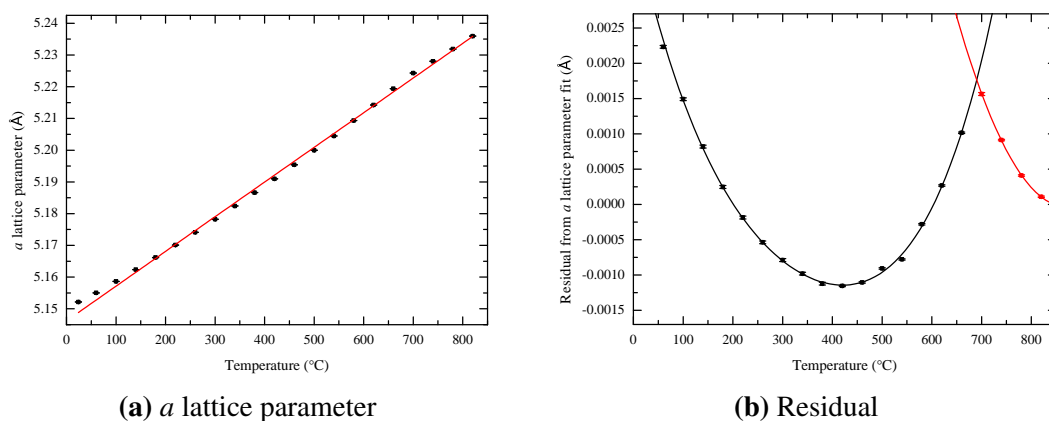


Figure 3-7 The (a) a lattice parameter as a function of temperature with a linear fit given by the red line and (b) the residual between the data and the linear fit. The residual data is coloured black and fitted with a fourth-degree polynomial below the phase transition and coloured red and fitted with second-degree polynomial above the transition.

ture for all samples. If the size of the oxygen octahedra stayed constant with increasing temperature, the decreasing tilt would result in an increase in the a lattice parameter. The determination of the distortion of the octahedra is not possible using short scans on a lab-based X-ray diffractometer; the uncertainties in measuring the distortion are too large to measure a trend with temperature, however the distortion parameter is negative for all samples in the temperature range investigated.

The effect of the size and distortion of the octahedra can be investigated by measuring the contact lengths between the O atoms that form the octahedra. The lengths of the oxygen triad on the top and the bottom of the octahedra are shown in figure 3-9b and are labelled L1 and L2 respectively. The triad with length L1 is the closest to the Ta atom. The measured lengths of L1 and L2 are plotted in figure 3-10, the error values are calculated from the errors in the refined O positions. The L1 length is larger than the L2 length, which is expected from the negative distortion parameter. The trend in L1 and L2 cannot be determined because of the inability to accurately refine the distortion of the octahedra. The changing size of the octahedra can be measured by calculating the average size of the triads as a function of temperature. This is given by the green data in figure 3-10 and shows that the size of the octahedra increases with temperature. In the paraelectric phase, the inversion symmetry means the O octahedra cannot be distorted and the triads above and below the Ta atom are the same. The triad length in the paraelectric phase is given by the red data in figure 3-10 and it follows the same trend

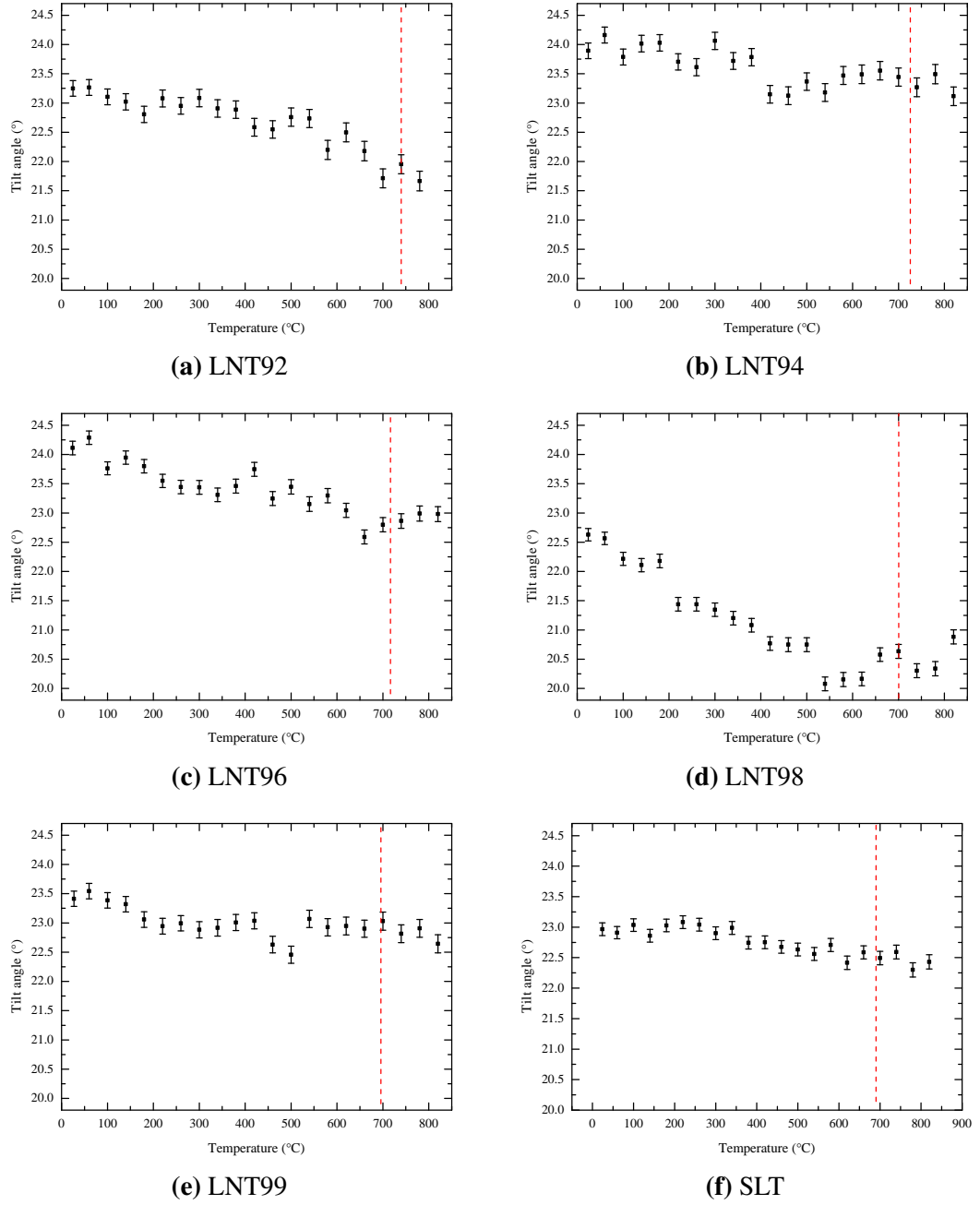


Figure 3-8 Ta displacement as a function of temperature for Ta-rich samples of LNT. The Curie temperature is marked by the dashed red line.

as the average triad length in the ferroelectric phase. This expansion combined with the rotation of the octahedra results in the increase in the measured a lattice parameter.

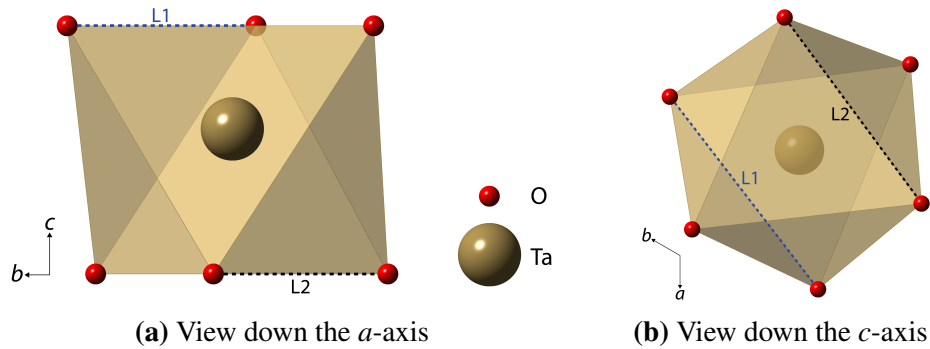


Figure 3-9 The oxygen octahedra when viewed along (a) the a -axis and down the c -axis. The bonds between the O atoms in the octahedra are marked by a blue dotted line for the upper face and a black dotted line for the lower face and are labelled L1 and L2, respectively.

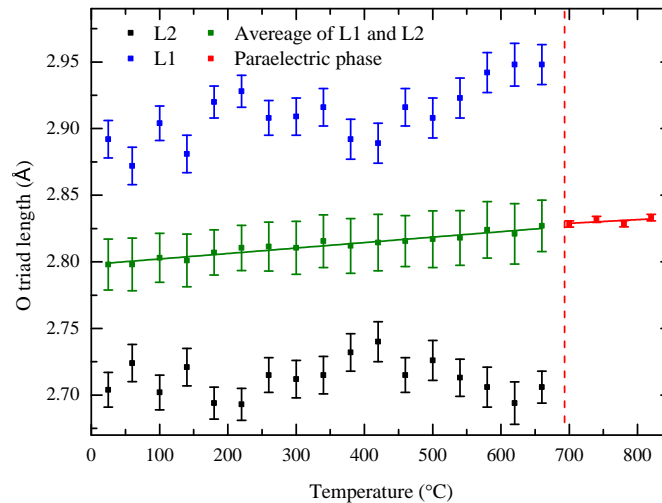


Figure 3-10 Triad lengths of LNT100 as a function of temperature. Below the Curie point, the lengths L1, L2 and the average of the two are shown by the blue, black and green points respectively and the red data show the triad length above the phase transition.

3.3.2 Curie point

By calculating the temperature of the intersection between the polynomial fits to the c lattice parameter in figure 3-5, the temperature of the Curie point can be measured. The plot of the residual between the a lattice parameter of LNT100 and a linear fit to it in figure 3-7b can also be used to calculate the Curie temperature in an analogous way to

using the c lattice parameter. The residual of a linear fit to the a lattice parameters for the high-Ta content samples is shown in figure 3-11. The same non-linear increase in the a lattice parameter below the phase transition was measured in all samples.

The Curie point as a function of composition from averaging the calculated values from both the c lattice parameters and the residuals of the a lattice parameter fits are shown in figure 3-12. The error bars on the values are calculated from the combined errors in measuring the Curie point from the XRD measurements and the accuracy of the sample furnace. It was not possible to fit a polynomial above the phase transition to the data collected on LNT92 because of a failed scan at 820 °C. This made it difficult to determine if the point at 740 °C (as can be seen in figures 3-5a and 3-11a) was above or below the phase transition. The linear fit to the Curie temperatures in figure 3-12 did not include the point measured on LNT92 and this point is plotted with error bars covering the possible range of values around 740 °C. The Curie point for SLT was measured to be 690 ± 3 °C which agrees with the previous value of 690 °C, measured by Barns et al using dielectric measurements on a range of crystals pulled from Li-rich melts [6]. The addition of Nb increases the Curie point linearly in the range of the high-LT content samples investigated. This is consistent with previous measurements showing a linear increase towards the Curie point of 1200 °C of LN, as determined on sintered LNT powders using dielectric measurements by Peterson et al [7].

3.4 Low-temperature X-ray powder diffraction

For low-temperature measurements a Bruker D5005 diffractometer in Bragg-Brentano geometry, producing Cu $K\alpha$ radiation, and equipped with an Oxford Cryosystems Phenix cryostat was used. A typical scan was measured between 21 and 135° in 2θ with a step size of 0.02° and a total counting time of 8 h. The intensity produced by the Bruker diffractometer is much lower than that of the PANalytical MPD. This means that parameters based on the intensity of a peak in the Rietveld refinement on the scans at low temperature are unreliable, however the positions of the peaks are not affected by this and the lattice parameters can be reliably measured.

Samples with LNT compositions of 80, 94, 96, 98 and 99 mol% LT were studied at low temperature to investigate the effect on the lattice below room temperature.

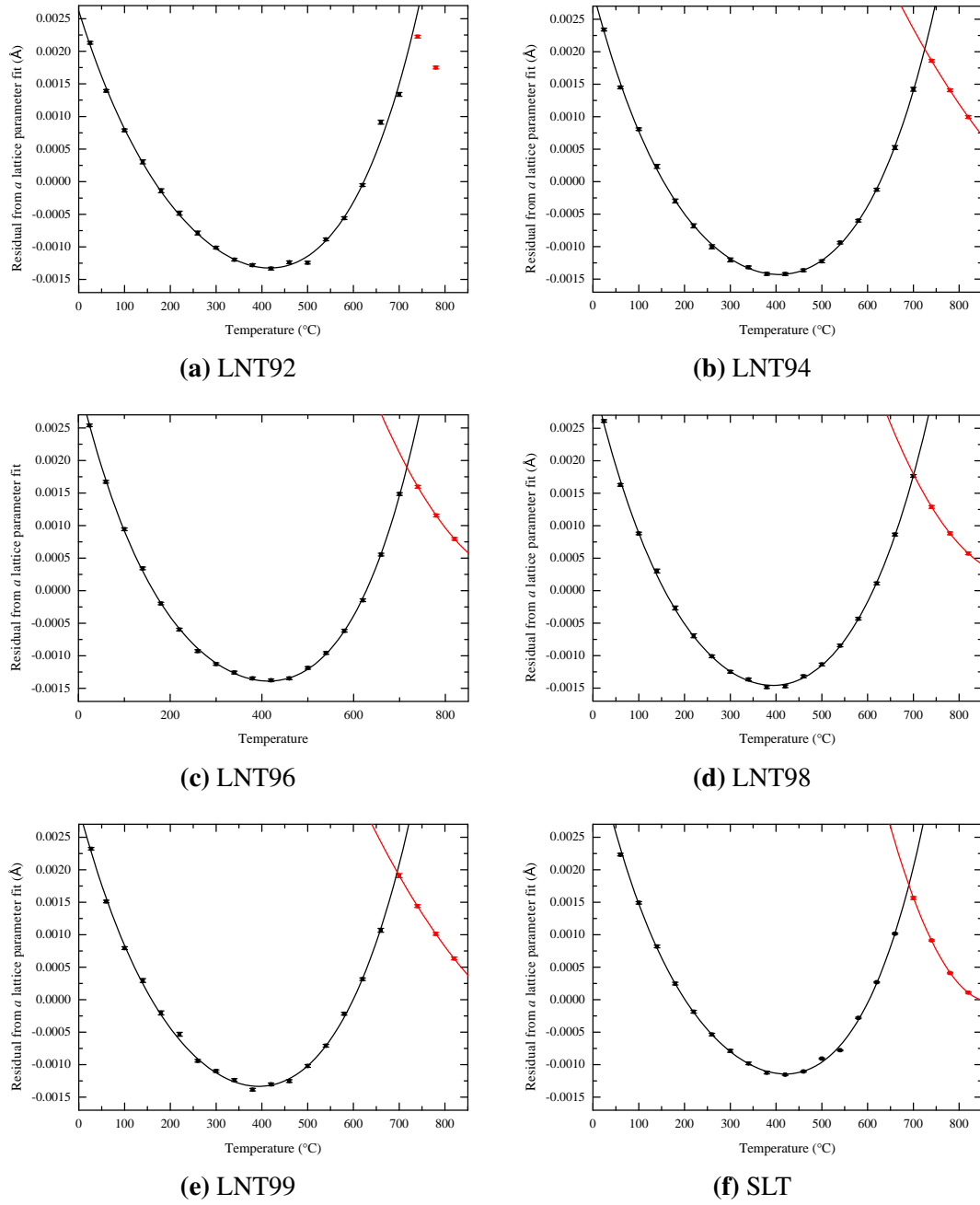


Figure 3-11 Residual from a linear fit to the a lattice parameters as a function of temperature for Ta-rich LNT samples. Polynomial fits applied to the data above and below the phase transition are given by the red and black lines respectively.

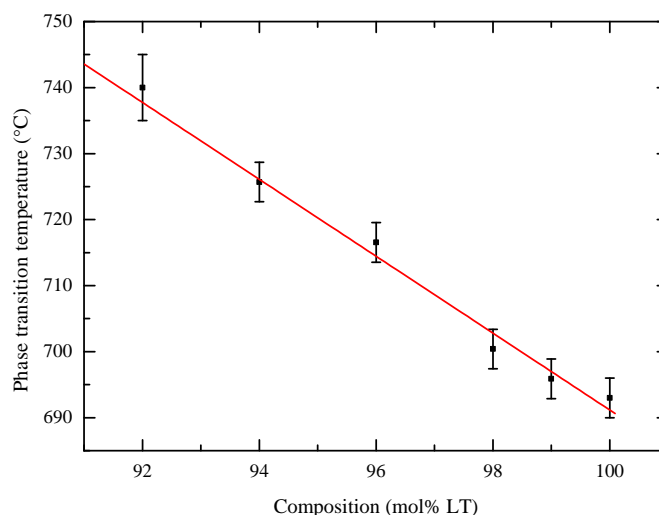


Figure 3-12 High-temperature phase transition as a function of LT content in the LNT sample. The error bars are calculated from the combined errors in measuring the phase transition using the XRD data and the accuracy of the furnace.

Scans were taken every 20 °C between 17 and –233 °C. Rietveld refinements of the low-temperature scans were performed following the same procedure as used in the refinements of the high-temperature scans in section 3.3. The sample displacement and the zero-offset of the diffractometer were calculated using the room-temperature lattice parameters from section 3.2. The lattice parameters were fixed and the sample height and zero-offset were refined, the refined zero-offset was then used for all other refinements. The refinement of the LNT94 scan at 17 °C is shown in figure 3-13. This refinement had an R_p of 9.901 %, R_{wp} of 7.624 %, gof of 1.29 and R_{Bragg} of 1.881 %.

3.4.1 Lattice parameters

The calculated a lattice parameters from the refinements as a function of temperature are plotted in figure 3-14a and the c lattice parameter in 3-14b. For all samples investigated, the lattice parameters vary continuously as the temperature decreases and tend towards a constant value. The a lattice parameter for LNT94 from –230 °C to 820 °C using the two different diffractometers is shown in figure 3-14c. The dashed black line marks the point between the measurements made on the Bruker D5005 and the PANalytical MPD and there is a small offset in the refined lattice parameters between these. This is due to the the method used to determine the correct sample height and zero-offset. The zero-offset on the Bruker D5005 diffractometer is calculated using the refined lattice parameters

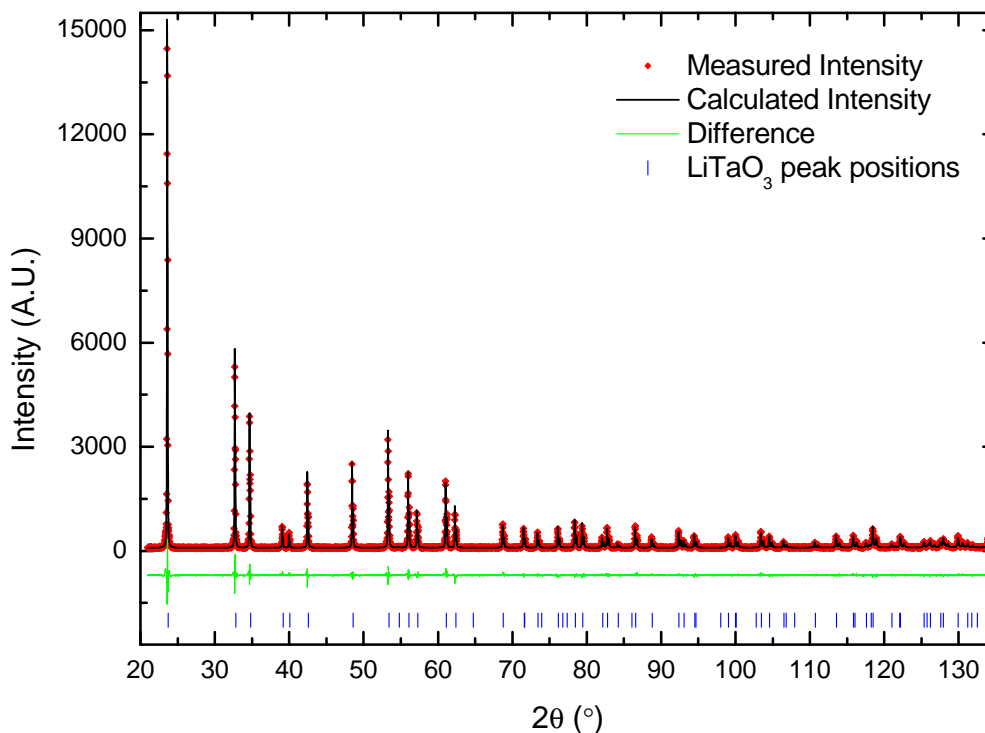


Figure 3-13 Rietveld refinement of the measurement at 17 °C on LNT94 using the Bruker D5005 diffractometer. The measured diffraction pattern is given by the red points, the calculated intensities by the black line and the difference between them by the green line. The blue lines give the positions of the Bragg peaks of the refined structure.

from the room-temperature measurements on the PANalytical MPD and this results in a small error. The zero-offset and the sample height could have been accurately determined using a scan of CeO_2 and following the procedure given by O'Connor et al [8]. This would require a scan of CeO_2 before each low-temperature run, adding to the total time required for all the measurements. The calibration of the diffractometer using the CeO_2 scan was not used because a small offset between the values measured on each machine did not affect the trend in the data and allowed all the scans for each sample to be made in 5 days.

3.5 Conclusions

The structure of LNT has been investigated across the compositional range at room temperature and between -230 and 820 °C for samples with high-Ta content. It has been shown that the lattice parameters vary smoothly and continuously across the compositional range and for samples with greater than 70 mol % Ta content, the Nb/Ta displace-

ment and the octahedral tilt also vary continuously with a change in composition.

The variation in the lattice parameters with temperature has been shown to be continuous from -230°C until the sample becomes paraelectric at high temperatures. The response of the lattice to increasing temperature has been explained by the change in the Nb/Ta displacement and the size and tilt of the O octahedra. Measurements of the birefringence on SLT crystals by Bäumer et al have shown that they become zero-birefringent at 100°C and Glazer et al showed that the addition of Nb increased the temperature of the zero-birefringence point [9, 10]. The high-temperature powder diffraction measurements have been used to investigate the structural changes as each LNT sample passes through this zero-birefringence point and they have confirmed that the structure remains polar and that the zero-birefringence is not due to a phase change.

The compositional and high-temperature measurements show that the Ta displacement and the tilt angle of the O octahedra are correlated; the Nb/Ta displacement and the octahedral tilt angle both decrease with increasing temperature and both increase as the quantity of Nb in the sample is increased.

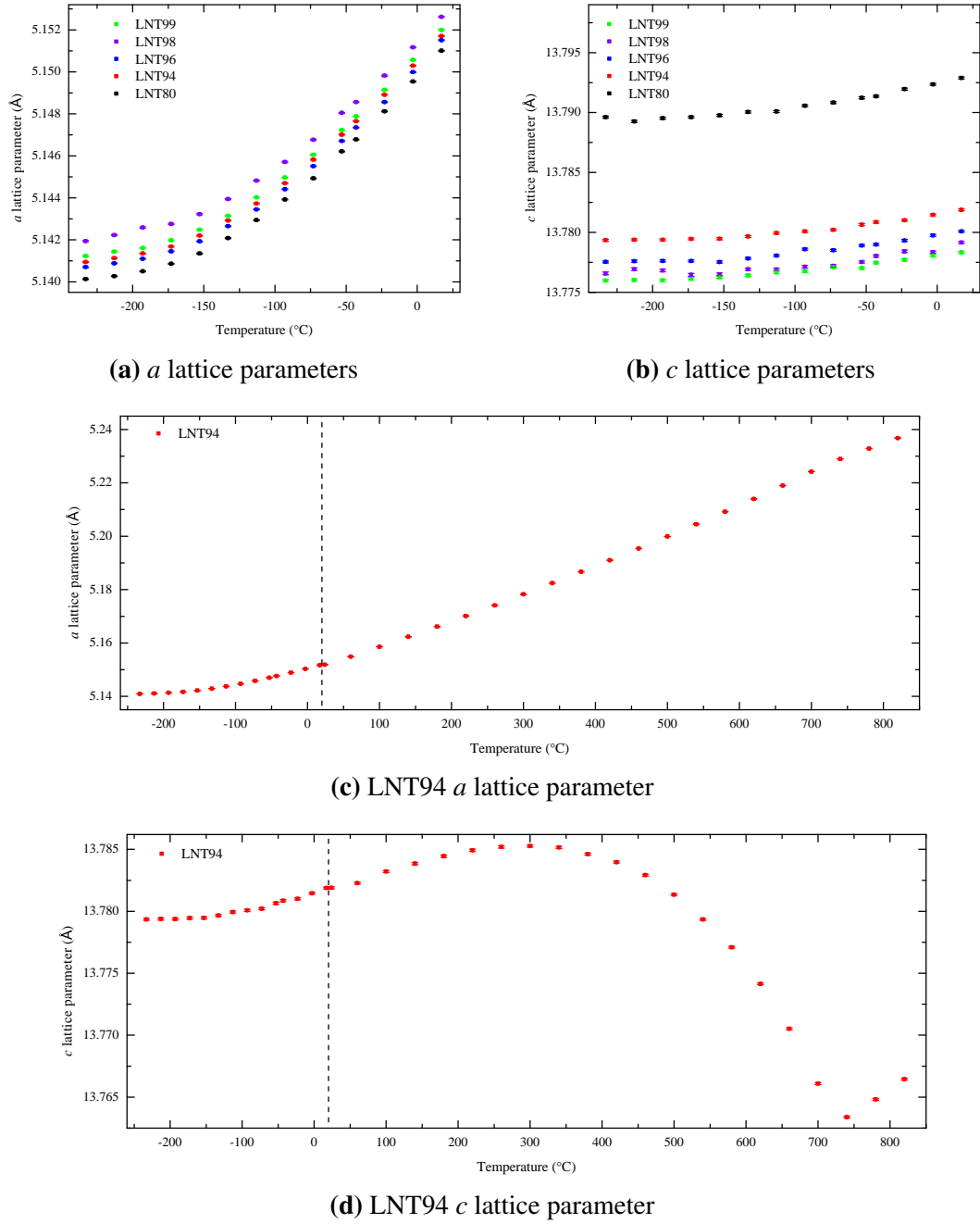


Figure 3-14 The (a) a lattice parameter and (b) c lattice parameter as a function of temperature below room temperature and the variation in the (c) a lattice parameter and (d) c lattice parameter of LNT94 from -230 to 820 °C. The dashed black line separates the measurements made on the two diffractometers.

References

- [1] A. Coelho, *Topas-academic v4.1* (2007), <http://www.topas-academic.net/>.
- [2] S. C. Abrahams and J. L. Bernstein, *Journal of Physics and Chemistry of Solids* **28**, 1685 (1967).
- [3] S. C. Abrahams, W. C. Hamilton, and A. Sequeira, *Journal of Physics and Chemistry of Solids* **28**, 1693 (1967).
- [4] A. Bartasyte, A. M. Glazer, F. Wondre, D. Prabhakaran, P. A. Thomas, S. Huband, D. S. Keeble, and S. Margueron, *Materials Chemistry and Physics* **134**, 728 (2012).
- [5] S. C. Abrahams, W. C. Hamilton, and J. M. Reddy, *Journal of Physics and Chemistry of Solids* **27**, 1013 (1966).
- [6] R. L. Barns and J. R. Carruthers, *Journal of Applied Crystallography* **3**, 395 (1970).
- [7] G. E. Peterson, J. R. Carruthers, and A. Carnevale, *The Journal of Chemical Physics* **53**, 2436 (1970).
- [8] B. H. O'Connor, D. Y. Li, and B. A. Hunter, *Advances in X-ray Analysis* **44**, 96 (2001).
- [9] C. Baumer, D. Berben, K. Buse, H. Hesse, and J. Imbrock, *Applied Physics Letters* **82**, 2248 (2003).
- [10] I. G. Wood, P. Daniels, R. H. Brown, and A. M. Glazer, *Journal of physics. Condensed matter* **20**, 235237 (2008).

CHAPTER 4

Powder diffraction study of $\text{Li}_y\text{Ta}_{1-y}\text{O}_3$

4.1 XRD measurements

4.1.1 Room-temperature measurements

A range of powder LT samples with varying Li concentrations were made to investigate the formation of the Li-rich phase and the effect of the non-stoichiometry on the structure of LT. These samples were provided by Ausrine Bartasyte and the raw materials used for the production of LT powders were Li_2CO_3 (99.9 %) and Ta_2O_5 (99.9 %). The mixed powders were ball-milled in isopropanol with alumina balls for 20 h, before being dried and pressed into pellets and calcined for 72 h at 1160 °C. This was followed by a final sintering at 1160 °C for 48 h to ensure a complete reaction between the starting materials. Samples with a range of Li_2CO_3 content between 48 and 54 mol % of the initial materials were produced. Measurements were also made on the SLT sample from section 3.1 and a CLT sample with 48.6 mol % Li_2O made using the single-firing method at 1160 °C for 130 h.

Room-temperature X-ray scans on the LT powders were performed using the PANalytical MPD and are shown in figure 4-1. The measurements on the powders with Li contents of 48, 49 and 50 mol % Li_2O form Li-deficient LT structures without the production of a second phase and the samples with greater than 50 mol % Li_2O form two

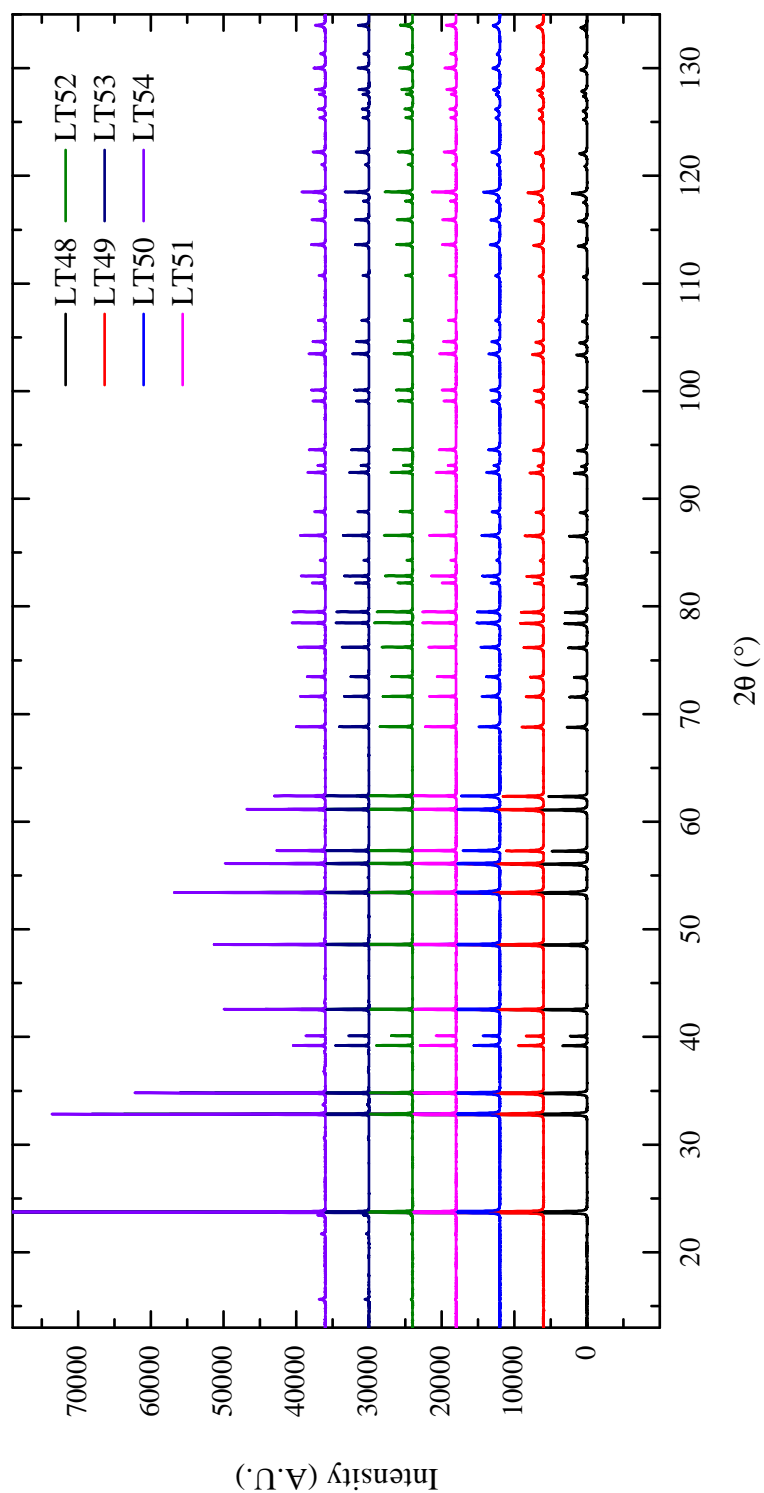


Figure 4-1 XRD measurements on LT powders made with 48 to 54 mol % Li_2O in the initial material.

phases; stoichiometric LT and the Li-rich phase Li_3TaO_4 (L3T). The amount of L3T in the samples increases as the amount of Li_2O increases above the stoichiometric ratio. Diffraction from the L3T phase is visible at low angles in figure 4-1 and the measured peaks are marked with arrows in the expanded section in figure 4-2a. This shows the intensity of the peaks from the L3T phase increase as the amount of Li_2O in the sample increases, with the phase being absent for samples made with the initial materials in the stoichiometric ratio.

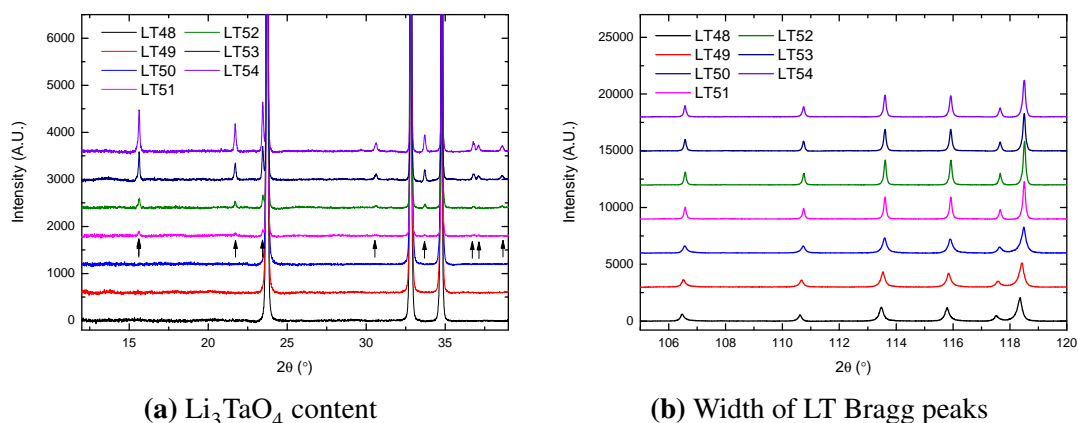


Figure 4-2 XRD measurements on LT powder samples focusing on (a) extra peaks due to formation of Li_3TaO_4 and (b) the effect of composition on the peak width. Bragg peaks from the L3T are marked with arrows.

The width of the peaks is dependent on the composition of the material; there is a decrease in the FWHM when the Li-content becomes sufficient enough to produce stoichiometric LT. This is shown in figure 4-2b. The width of the peaks for the LT48, LT49 and LT50 samples are visibly wider than the peaks of LT51, LT52, LT53 and LT54. To measure the widths of the peaks the data have been fitted with an asymmetric split-Pearson VII profile, allowing an accurate fit to the asymmetrical Bragg peak shape. The fit of the (012) Bragg peak in SLT is shown in figure 4-3a and FWHM's of the (012), (-114) and (116) for all the samples are plotted in figure 4-3b. This shows that when there is enough Li_2O , LT forms with full stoichiometry and has a reduced FWHM compared to the Li-deficient LT. The loss of Li_2O during sintering and calcining means that SLT is only formed when the initial materials have an excess of Li_2O . The single-firing method does not suffer from a loss of Li_2O and SLT is made using the initial powders mixed in a stoichiometric ratio.

Rietveld refinements of the measured diffraction data were performed using Topas

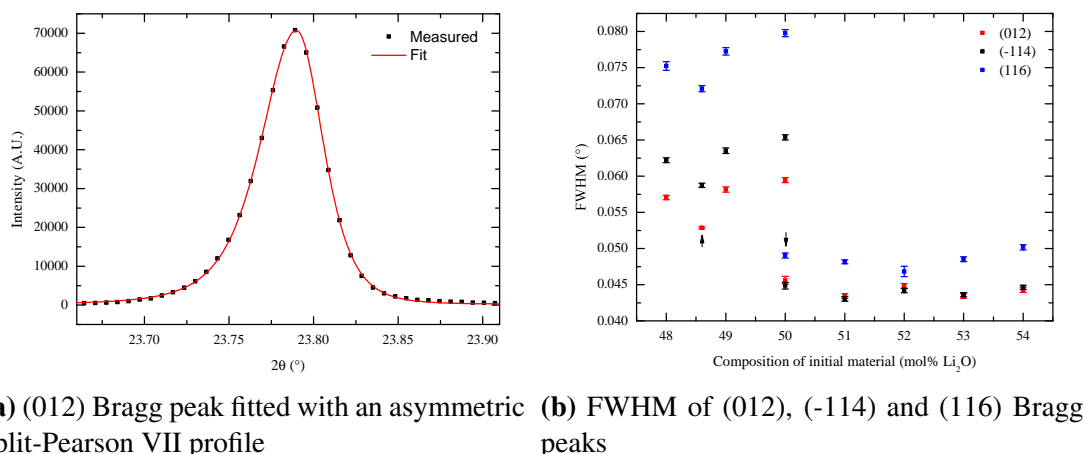


Figure 4-3 In (a) the (012) Bragg peak of LT51 fitted with an asymmetric Pearson VII profile and (b) the FWHM as a function of Li_2O content of the (012), (-114) and (116) Bragg peaks, given by the red, black and blue points, respectively. Samples made using the single firing method are marked by the arrows.

Academic and following the method for the refinement of room-temperature scans on LNT in section 3.2 [1]. The refinements were made assuming a stoichiometric composition because the XRD measurements are insensitive to the positions of Li atoms and incapable of refining a defect model of the structure. For the samples containing the L3T phase, the structure of L3T was refined at the same time as the LT structure. The refinement of LT54 is shown in figure 4-4 with the positions of the peaks from the refined LT and L3T structures marked by the blue and orange vertical lines, respectively. The amount of L3T in the samples is small compared to the amount of LT which dominates the diffraction pattern. The addition of the L3T phase can be clearly seen in the expanded section of the refinement and the close agreement between the fit and measured intensity confirms the second-phase as L3T.

The weight percent of each phase is calculated in the refinement and can be used to calculate the mol % of L3T in the sample. The calculated L3T content, plotted as a function of the amount of Li_2O in the initial material is in figure 4-5a. The amount of L3T formed if there was no loss of Li_2O during sintering is given by the red line and the expected content assuming 1 mol % and 2 mol % of Li_2O is lost are given by the blue and orange lines, respectively. The amount of Li_2O lost during sintering varies as the composition changes and can be calculated using the refined Li_3TaO_4 content and assuming that no Ta_2O_5 is lost. This is plotted against the composition of the initial

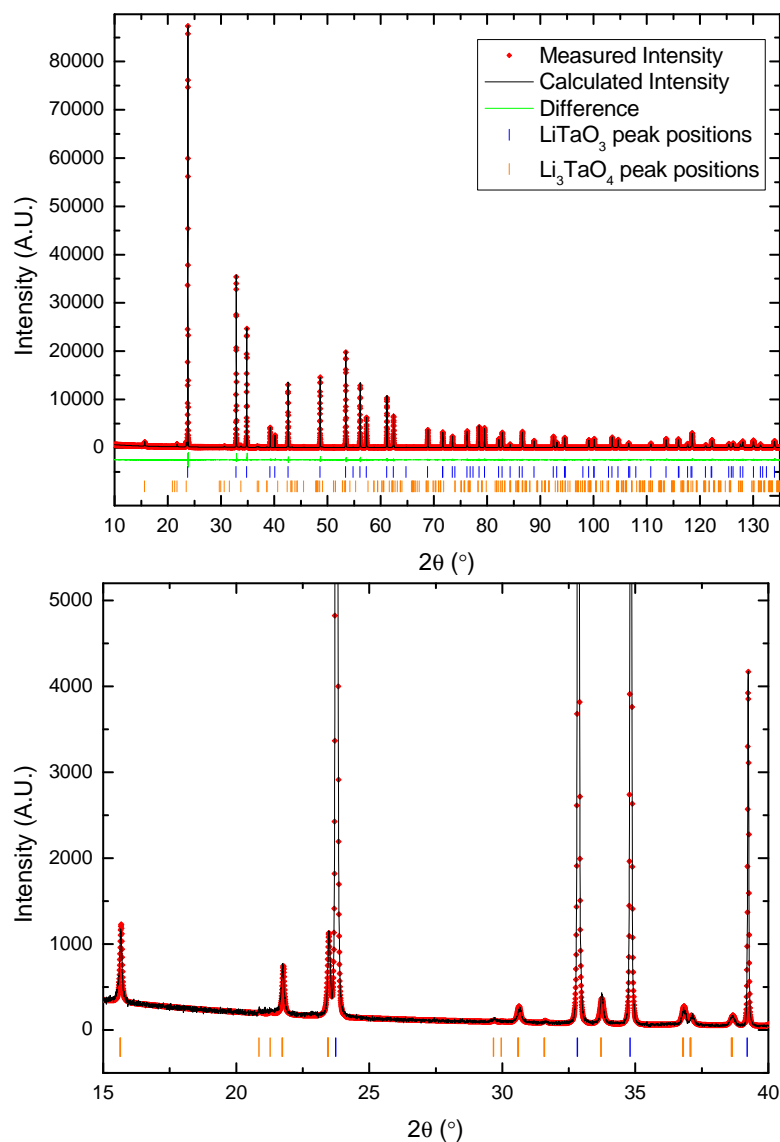


Figure 4-4 Rietveld refinement of LT54 powder, with the measured data denoted by red diamonds, the refined pattern by the black line and the difference between them by the green line. The positions of the Bragg peaks from the refined LT and L3T structures are marked by the vertical blue and orange lines, respectively.

materials in figure 4-5b. It is reasonable to assume that the amount of Li_2O lost is dependent on the composition and will increase as the Li-content increases. A linear fit to the Li_2O loss without including the value measured for LT52 is given in figure 4-5b. The Li_2O loss measured for LT52 is large and including it in the fit results in a trend that predicts that Li_3TaO_4 would not be formed when the initial material has 51 mol % Li_2O . The fit to the values excluding LT52 can be used to estimate the Li_2O loss in the samples that haven't formed Li_3TaO_4 . The actual composition of LT50 is 49.8 ± 0.2 mol % Li_2O and the amount of Li_2O lost is expected to be zero for samples

with less than 49.5 mol % Li_2O in the initial material. The error in the composition of the LT samples is large because of the assumption that the Li_2O lost during heating will vary linearly and the use of only three points for the fit.

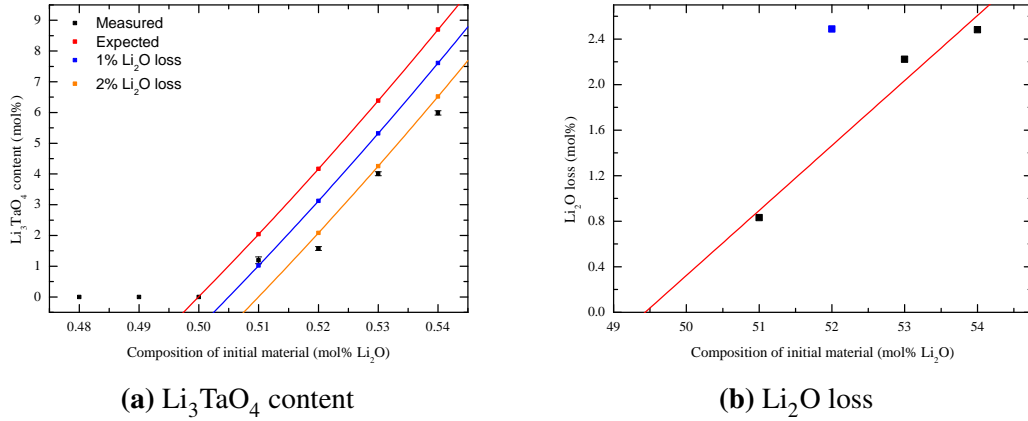


Figure 4-5 In (a) the measured amount of L3T formed in samples as a function of the amount of Li_2O in the initial materials. With the expected amount with 0, 1 and 2 % of the Li_2O lost given by the red, blue and orange lines, respectively. In (b) the calculated amount of Li_2O lost is plotted against the composition of the initial materials.

The refined lattice parameters of the LT for each sample are plotted against the corrected Li_2O content in figures 4-6a and 4-6b. The corrected Li_2O content is equal to the initial content minus the the amount lost during firing. For the samples that have not had a correction applied to their composition, only the error bars on the left side are included because the largest source of error is the loss of Li_2O which cannot result in an increase in the composition. Both the a and c lattice parameters become constant above 50 mol % Li_2O , which shows that stoichiometric LT is formed and any excess Li_2O is used to form L3T. The point at 50 mol % Li_2O is the LT powder sample made in the previous section on LNT powders. The lack of L3T in this sample and its similar lattice parameters to the samples containing greater than 50 mol % Li_2O mean that the LT sample produced using the single-firing method in section 3.1 has not lost any Li_2O during heating. The measured FWHM of all the LNT powders agree with those measured on the stoichiometric samples and not those of the Li-deficient samples. This confirms that the LNT samples are stoichiometric and there was no loss of Li_2O during heating.

The a lattice parameter decreases linearly towards the stoichiometric value as the amount of Li_2O in the Li-deficient LT is increased. This is consistent with previous

measurements of the congruent crystals which have a higher a lattice parameter than those of stoichiometric crystals [2]. The c lattice parameter also decreases linearly, but becomes less than the stoichiometric value when the composition is 49 mol % Li_2O .

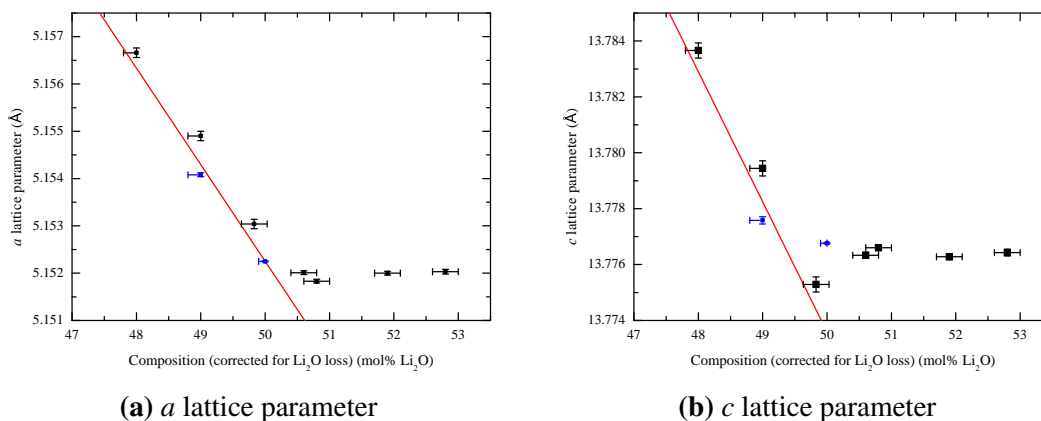


Figure 4-6 The (a) a and (b) c lattice parameters as a function of the Li_2O content in the LT samples. Samples made using the single firing method are blue and the errors in the values are from the esd's given by the Rietveld refinement.

The refined displacement of the Ta from the centre of the O octahedra is plotted in figure 4-7a. A small variation in the displacement occurs for stoichiometric LT samples above 50 mol % Li_2O . These small variations are not within errors and suggest the errors on the Ta position are larger than those given by the esd's of the refinement when there are two phases. Between 48 and 50 mol % the displacement increases linearly as the composition increases towards the stoichiometric value. The refinement of the position of the Li atom is unreliable because of the poor scattering of X-rays; however, the value for LT powders is consistent with that of the LNT powders. The plot of the Li displacement in figure 4-7b has a dip in the displacement as the amount of Li_2O is increased towards the stoichiometric ratio.

The response of the O octahedra to the changing Li concentration of the samples is shown in figure 4-8. The refinements of the powder diffraction data do not provide a precise value for the distortion of the octahedra as can be seen by the large variation across the composition. However, the distortion is small and negative which is consistent for both measurements on LNT and LT samples.

There is a decrease in the tilt angle in the Li-deficient compositions of 48, 49 and 49.8 mol % Li_2O compared to the samples with 50 mol % or greater. This is a decrease

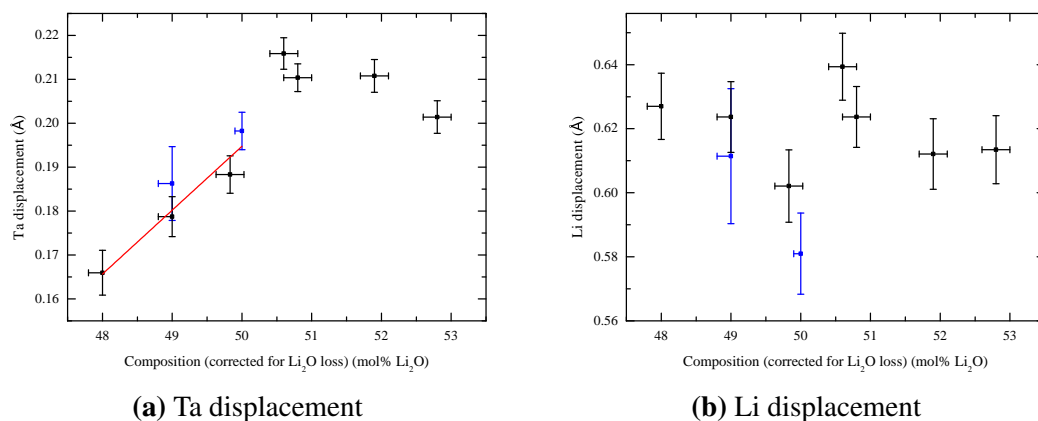


Figure 4-7 The (a) displacement of the Ta from the centre of the O octahedra and (b) displacement of Li from the O plane as a function of the Li_2O in the sample.

of roughly 0.25° which is greater than the associated errors in the refined values, suggesting the octahedra is affected by the decrease in Li_2O content. The tilt angle of the octahedra decreases while the Ta displacement decreases, this is similar to the relationship in the LNT powders where the increase in the quantity of Nb results simultaneously in an increase in the Nb/Ta displacement and octahedral tilt.

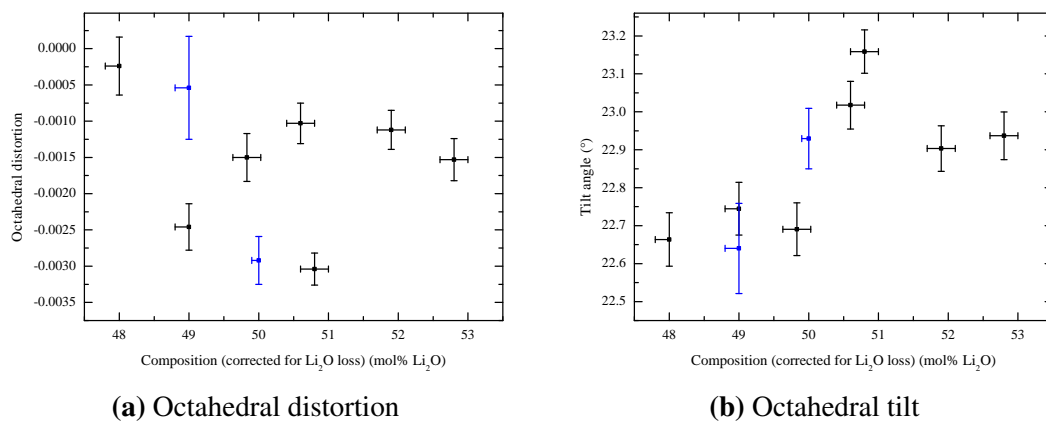


Figure 4-8 The (a) octahedral distortion and (b) tilt as a function of the composition of the LT sample.

4.1.2 High-temperature measurements

4.1.2.1 Lattice parameters

High-temperature diffraction measurements using the PANalytical MPD and the Anton Paar sample furnace have been made on LT samples. The same procedure as used in section 3.3 for making the XRD measurements and refining the structure was followed. The refined c lattice parameter for the LT samples is shown in figure 4-9. The c lattice parameters of the LT samples have the same variation with temperature measured on the LNT samples; an initial peak around 200 °C to 300 °C followed by a decrease before the Curie point. The calculated a lattice parameters have been fitted with a linear trend and the residual is plotted in figure 4-10. An abrupt change in the residual occurs at the Curie point similar to the measurements on LNT samples.

4.1.2.2 Curie point

The effect of the decrease in the amount of Li in the LT sample results in a reduction in the phase transition temperature. The phase transition as a function of composition is given in figure 4-11. A similar trend between the composition and the phase transition temperature was measured by Bordui et al using dielectric measurements on Czochralski-grown single crystals [3]. The gradient of the linear trends differ and the results of these measurements suggest a higher phase transition temperature for a given composition than that given by Bordui et al. Previously, a range of measurements have given the Curie point of CLT to be between 598 and 608 °C with an in-depth study by Kushibiki et al measuring a value of 603.0 °C and a composition of 48.46 mol % Li_2O [2, 4, 5]. The phase transition temperature of 603 °C would correspond to a composition of 48.3 ± 0.2 mol % Li_2O in this study, and agrees with the precisely determined composition of CLT by Kushibiki et al.

4.1.2.3 Atomic positions

The refined Ta displacement for the varying LT composition samples is plotted in figure 4-12 and decreases with temperature towards the Curie point. The variation in the displacement is similar for all compositions of LT studied and also for the LNT samples. The octahedral tilt angle decreases for LT compositions as the temperature increases and

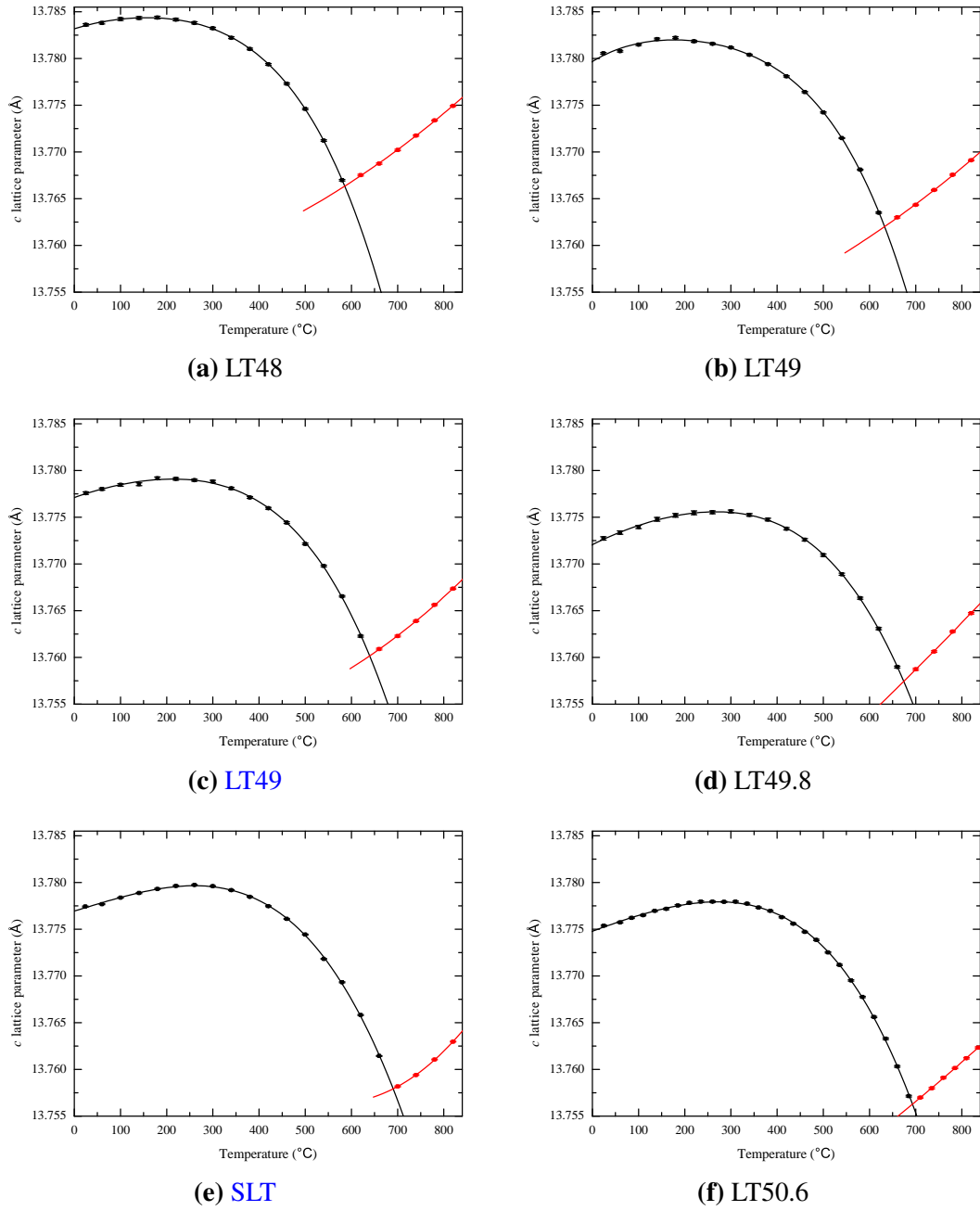


Figure 4-9 The c lattice parameter for each LT concentration as a function of temperature. The points below the phase transition are black and polynomial fits to these data are given by the black line. The red squares are the points above the phase transition and the red line is a polynomial fit to them.

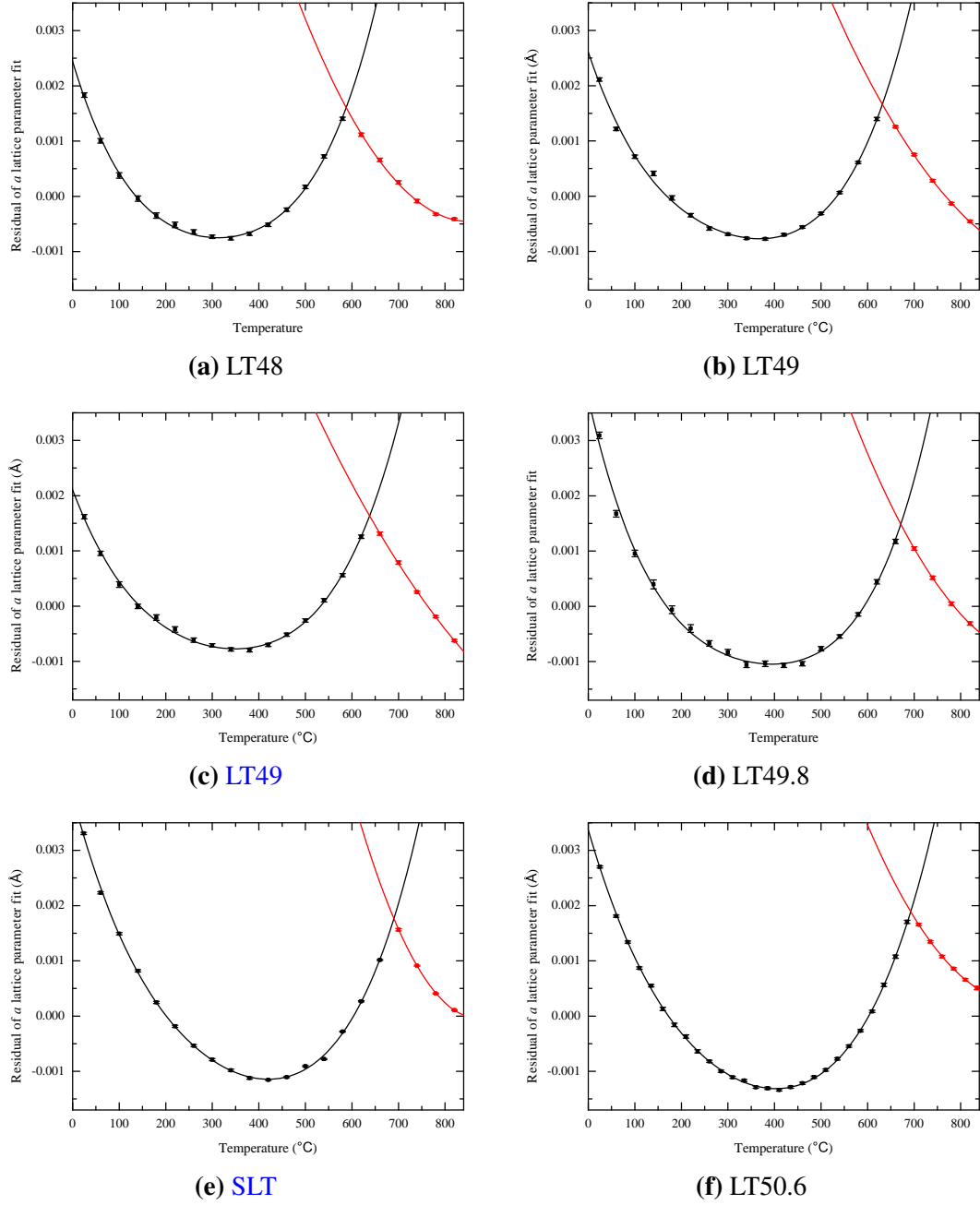


Figure 4-10 The a lattice parameter for each LT concentration as a function of temperature. The points below the phase transition are black and polynomial fits to these data are given by the black line. The red squares are the points above the phase transition and the red line is a polynomial fit to them.

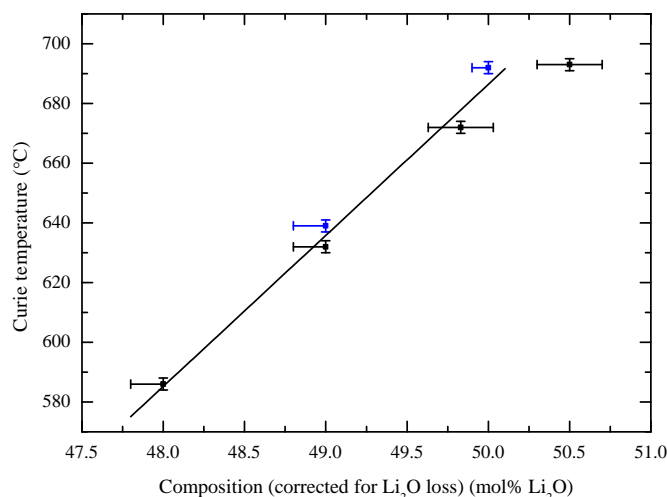


Figure 4-11 High-temperature phase transition as a function of Li_2O content of the LT sample. The error bars are calculated from the combined errors in measuring the phase transition using the XRD data and the accuracy of the furnace.

is shown in figure 4-13. The tilt angle decreases in the ferroelectric phase and above the Curie point.

4.2 Isotopically enriched SLT

4.2.1 Introduction

Neutron diffraction is an important tool for studying the structures of oxide materials, because of the extra information gathered on light elements when compared to using X-ray diffraction. The SLT powder used for this experiment was made using Li_2CO_3 which has been isotopically enriched to be 99.99 % ^7Li , this was to compensate for the large absorption coefficient of ^6Li . The coherent scattering length for ^7Li is -2.22 fm, for Ta is 6.91 fm and for O is 5.803 fm, which means the scattering is not dominated by one element as it is by Ta in X-ray diffraction. A stoichiometric sample was made using the single-firing method used in section 3.1.

4.2.2 XRD measurements

High-temperature measurements were performed using the PANalytical MPD and the Anton Paar sample furnace to calculate the Curie point and check the Li content of the

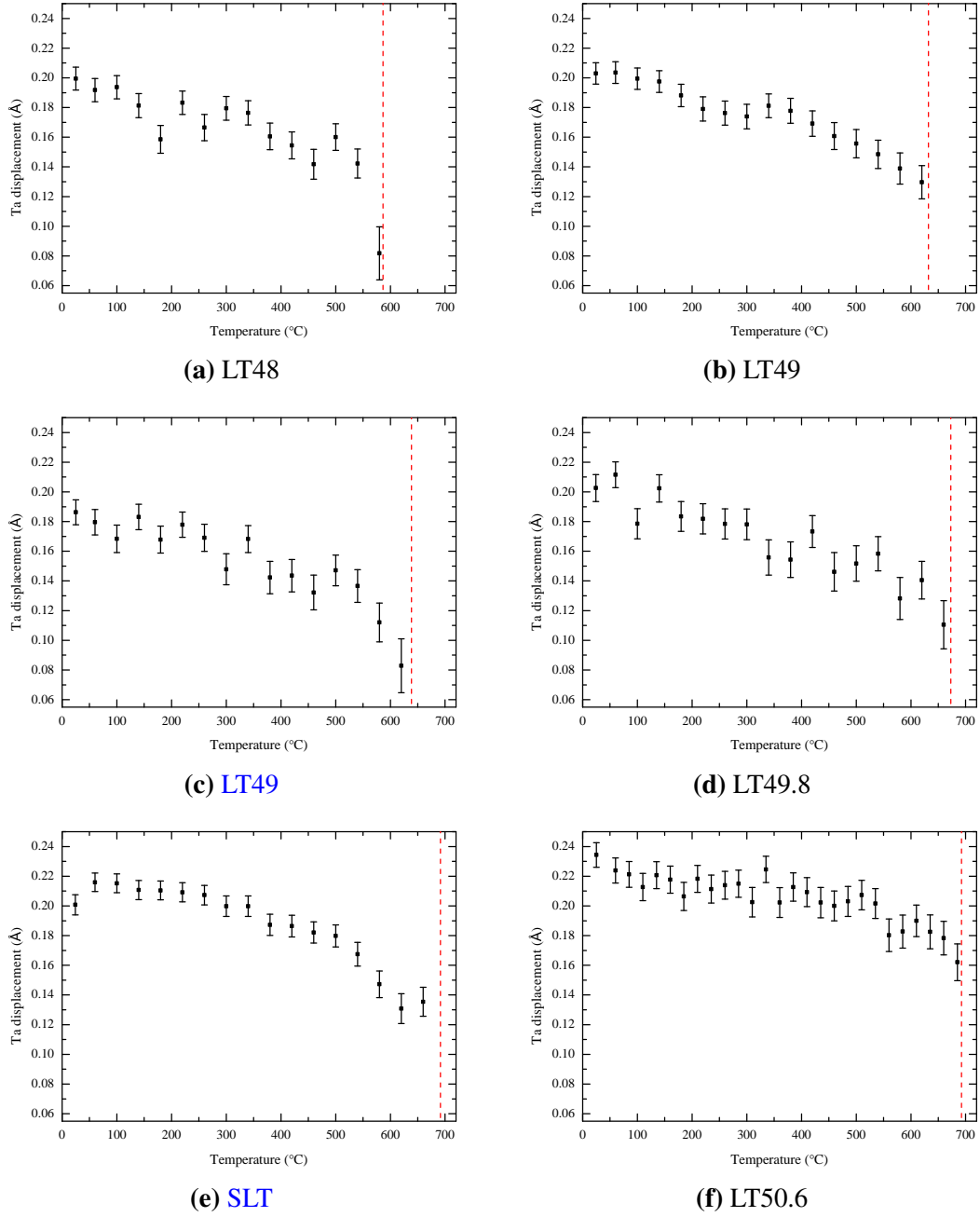


Figure 4-12 The Ta displacement for each LT concentration as a function of temperature. The Curie point is marked by the dashed red line.

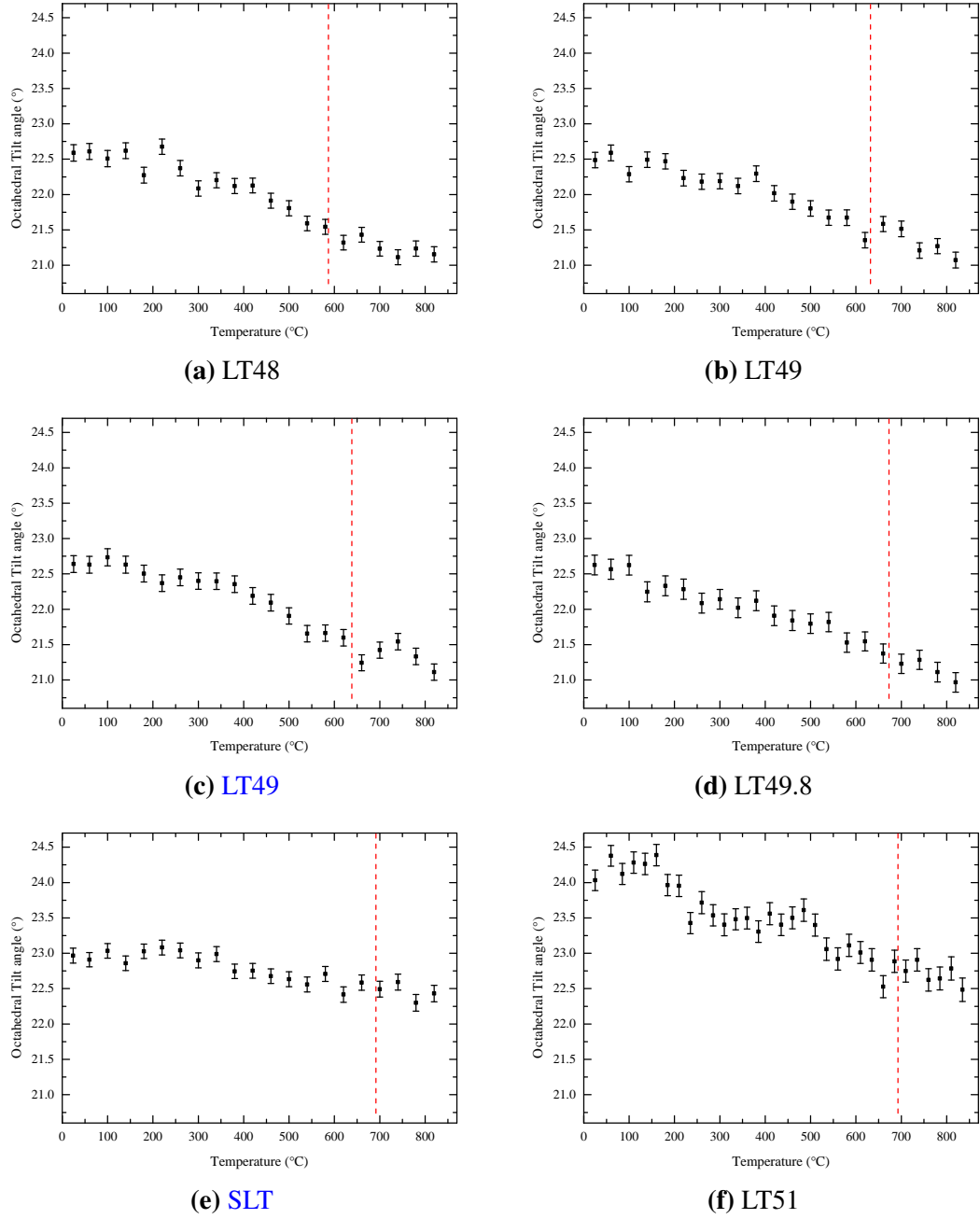


Figure 4-13 The octahedral tilt angle as a function of temperature for a range LT concentrations. The Curie point is marked by the dashed red line.

sample. Measurements made every 40 °C between 60 and 820 °C were refined using the same procedure for high-temperature XRD measurements on LNT and LT powder samples.

The refined c lattice parameters and residuals of a linear fit to the a lattice parameters are plotted in figure 4-14. The intersection between the polynomial fits gives a Curie point of 654 ± 3 °C. This is less than the expected value of 690 °C for SLT and using the results of section 4.1.2.2 the actual composition is 49.36 ± 0.06 mol % Li_2O . This sample has lost a large amount of Li_2O during firing and has resulted in a composition between the congruent and stoichiometric extremes. The FWHM of the (012) peak is $0.053 \pm 0.001^\circ$ in 2θ , and according to figure 4-3 is consistent with the sample having lost Li_2O during heating. The equipment used in making this sample was the same as used for previous LNT samples, which did not show a loss of Li_2O during heating. This suggests either the platinum crucible was poorly sealed or the use of the enriched ^7Li resulted in an increased loss of Li_2O .

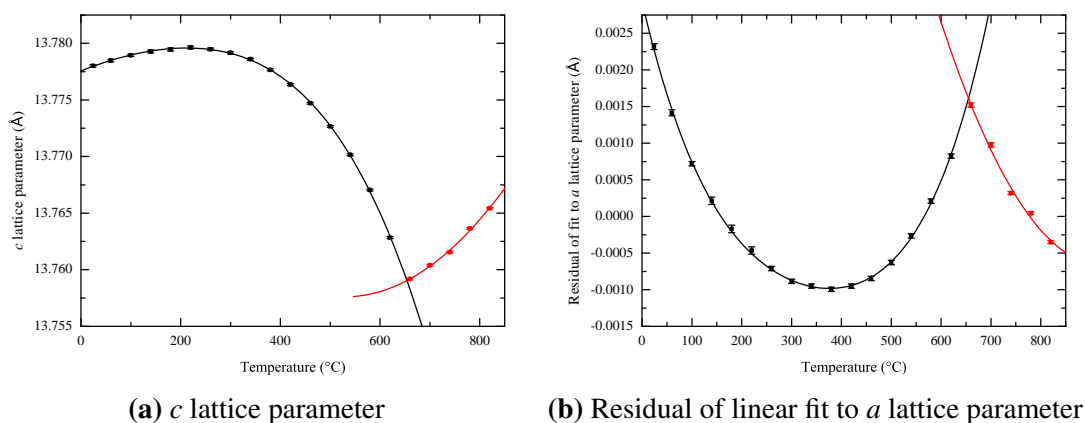


Figure 4-14 The (a) c lattice parameter and (b) residual of a linear fit to the a lattice parameter as a function of temperature. Data below the phase transition are black and fitted with a fourth-order polynomial. The red data above the phase transition are fitted with a second-order polynomial.

4.2.3 Neutron diffraction measurements

Variable-temperature measurements were performed with a fixed neutron source at the Institute Laue-Langevin (ILL), in Grenoble, France. The ILL uses a nuclear reactor to produce a high flux of neutrons for a range of different experiments. The D2B beam-line consists of a Ge[115] crystal monochromator which can be rotated to provide a

range of different wavelengths for the experiments. The optimum wavelength for the diffractometer is 1.594 Å. It is well aligned and produces the highest neutron flux. The detector consists of 128 ^3He counting tubes, spaced 1.25° apart. A full diffraction pattern between 5 and 165° in 2θ is recorded after moving the detector through $25 \times 0.05^\circ$ steps, and each scan is repeated to improve the counting statistics.

A cryofurnace with a temperature range of 5 to 525 K was used for the experiments on the LT49.36 sample. Scans were made above room temperature, in the range of 27 to 172°C . A large vanadium can filled with roughly 15 g of sample was used for the measurements. Ten repeated scans were made at each temperature, resulting in a total measurement time of 2 h.

A room-temperature XRD powder pattern collected using the PANalytical MPD diffractometer was refined to calculate the lattice parameters. The refined lattice parameters from this calculation were then used in a refinement of the room-temperature neutron data to calculate the zero-offset and the wavelength of the D2B diffractometer. The background in the neutron measurements was modelled using ten small Gaussian peaks and at each temperature the positions of the individual peaks and an overall scale factor governing the size of the peaks was refined. Figure 4-15 shows the refinements of the XRD and neutron data collected at room temperature. Structural models including Li vacancies and Ta atoms on the Li site did not change the refined lattice parameters or atomic positions and resulted in an incorrect value for the amount of Li in the structure. Because of this the structural refinements were performed assuming the composition was stoichiometric.

A precise order in which the parameters were allowed to refine was followed for each temperature to keep each refinement consistent, this procedure is described below:

1. The neutron wavelength was set to 1.5934 Å and the zero-offset to -0.03424° using the room-temperature XRD measurement.
2. The lattice parameters and atomic positions were set to the refined values at the previous temperature and an initial refinement was then performed with only the background, peak shapes and lattice parameters allowed to vary.
3. This was followed by refining the atomic positions and the simple axial model for both sets of data.

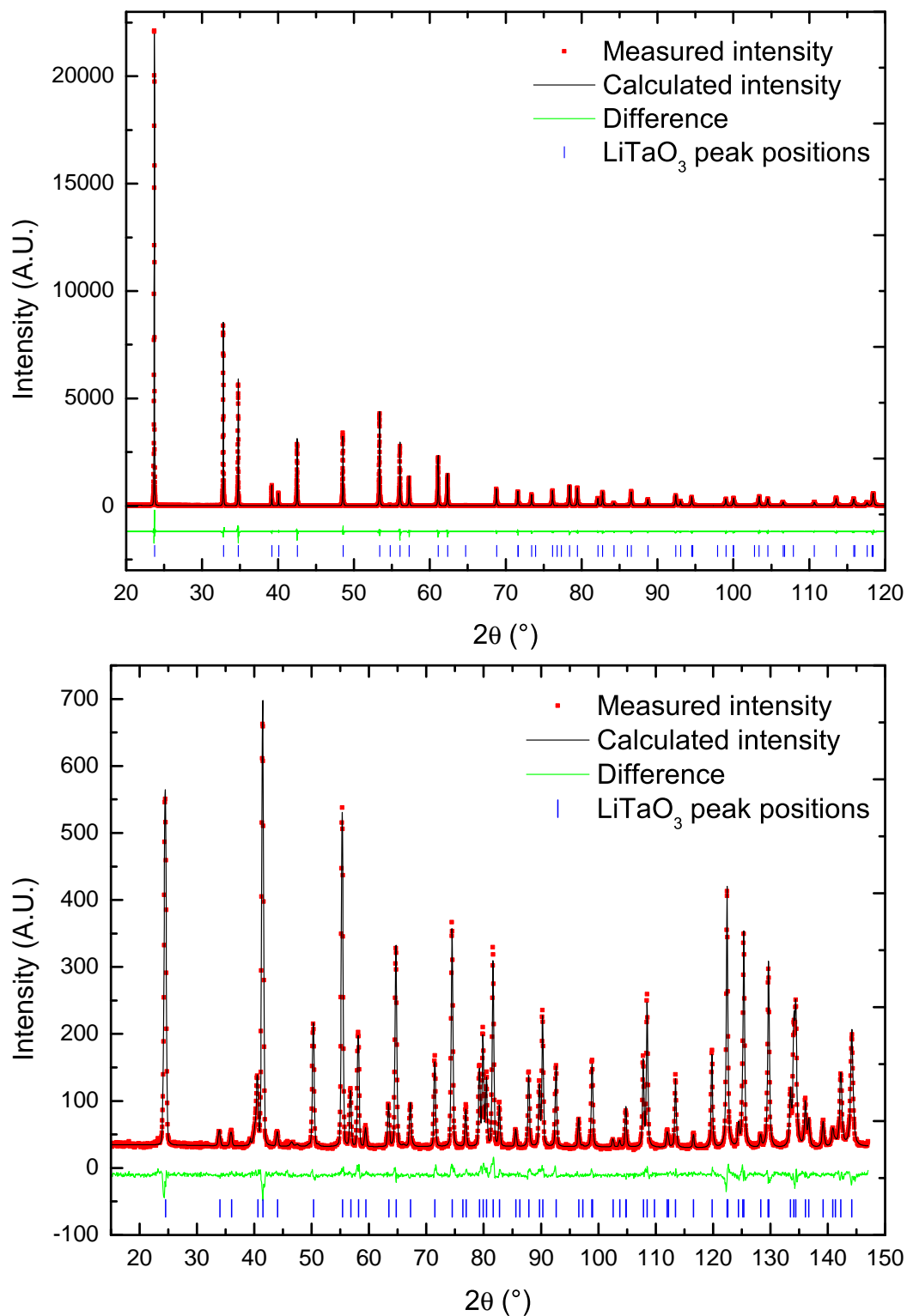


Figure 4-15 Rietveld refinement on LT49.36 for (a) the XRD measurement and (b) the neutron diffraction measurement. The observed data are plotted in red, the calculated in black and the difference between them is green. The blue points mark the positions of the Bragg peaks of the refined structure.

4. Next the Stephens parameters were included.
5. Finally the isotropic thermal parameters of the Li, Ta and O atoms were included in the refinement.

4.2.4 Lattice parameters

The lattice parameters from the refinements are plotted in figure 4-16. The a and c lattice parameters show the expected nearly linear increase with temperature and agree with the room-temperature value calculated previously using only XRD measurements on samples made with the natural abundance of Li isotopes.

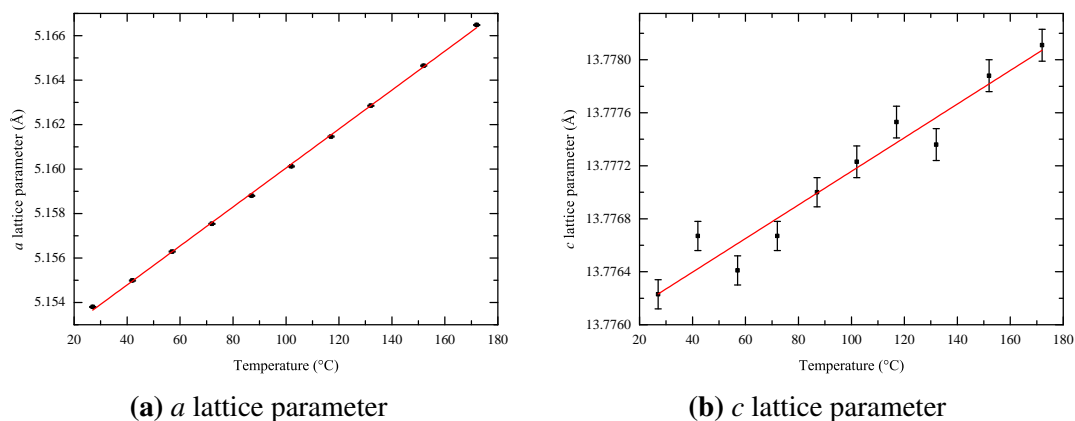


Figure 4-16 The (a) a lattice parameter and (b) c lattice parameter plotted as a function of temperature. The error bars were calculated from the esd's via Topas Academic.

4.2.5 Atomic positions

The displacement of the Li atom as a function of temperature is plotted in figure 4-17a and decreases linearly as the temperature increases. The room-temperature value is 0.601 ± 0.004 Å calculated from the neutron diffraction measurements and is in the range of 0.58 to 0.64 Å measured using XRD measurements on LT samples. This confirms that measurements using XRD cannot be used to calculate a trend in the Li position as a function of composition or temperature; however, the refined values agree with those refined using neutron diffraction.

As the temperature increases, the displacement of the Ta atom decreases linearly in the temperature range studied. The refined displacement is plotted in figure 4-17b

and is consistent with the measurements of the Ta displacement using XRD. The room-temperature displacement calculated for LT49.36 is $0.195 \pm 0.002 \text{ \AA}$ and agrees well with the XRD measurements in figure 4-7a which suggests the value should be between 0.18 and 0.20 \AA .

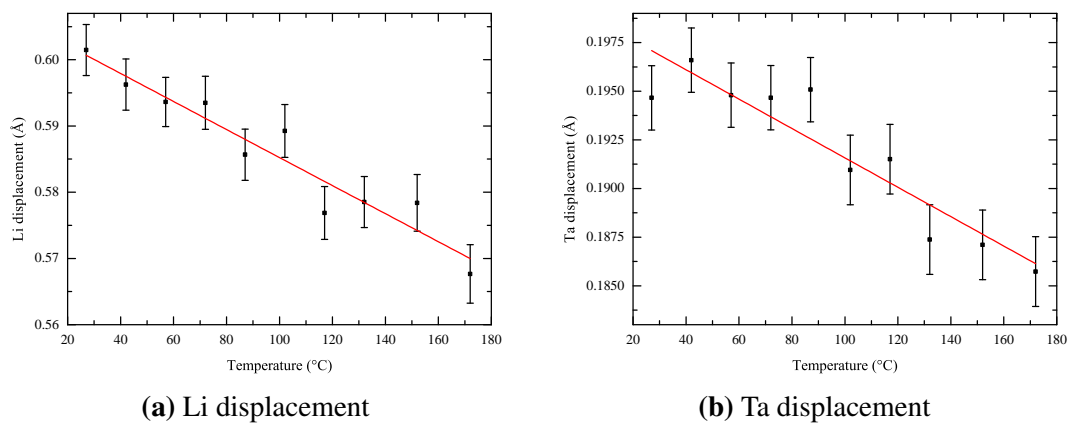


Figure 4-17 The displacement of the (a) Li atom from the O triad at $z = 0.25$ along the c axis and (b) Ta atom from the centre of the O octahedra.

The distortion of the O octahedra is plotted in figure 4-18a. The measured values are between -0.00235 and -0.0025 and the errors on the values are of a similar size, which means a trend in the distortion with temperature cannot be measured. The octahedral tilt decreases with temperature, as expected from the XRD measurements and is plotted in figure 4-18b. In the temperature range investigated the octahedra rotate linearly, which is consistent with measurements using XRD on both LT and LNT samples.

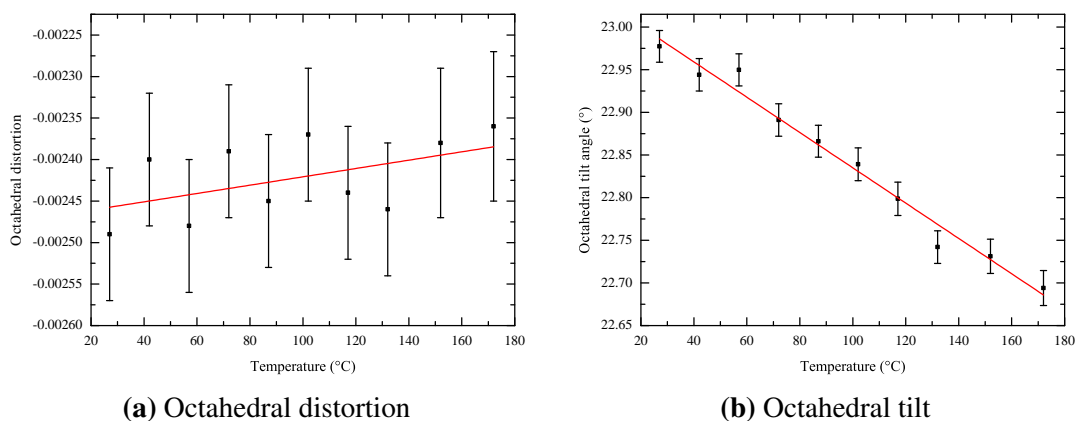


Figure 4-18 The (a) O octahedral distortion and (b) octahedral tilt angle as a function of temperature.

4.2.6 Bond lengths

The O-O, O-Li and O-Ta bond lengths describe how the structure varies as the temperature increases. The precise determination of the octahedral distortion allows a value for bond lengths involving an O atom to be calculated. The O triad lengths of the upper and lower faces of the octahedra are shown in figure 4-19a and labelled L1 and L2, respectively. The calculated values for L1 and L2 along with their average are plotted in figure 4-20. The upper triad, which is the closest to the Ta atom is the larger of the two and both increase in size with temperature. The effect of the distortion is removed in the averaged size of the two triads and confirms that the size of the octahedra is increasing with temperature.

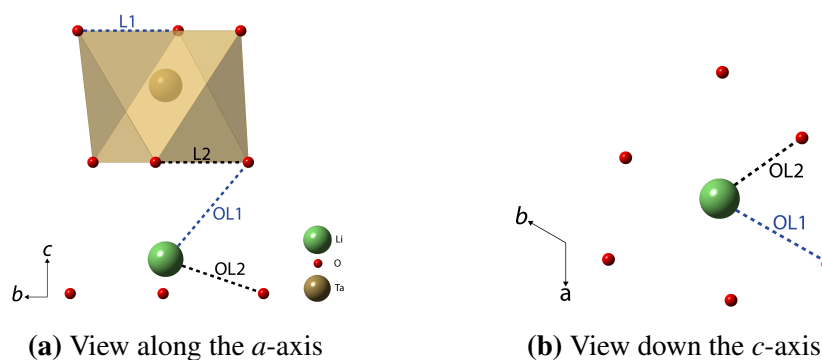


Figure 4-19 The O octahedra when viewed along (a) a -axis and (b) down the c -axis. The bonds between the O atoms in the octahedra are marked by a blue dotted line for the upper face and a black dotted line for the lower face and are labelled L1 and L2, respectively.

The O-Li bond lengths are shown in figure 4-19 and are labelled OL1 for the bond length between the O in the lower triad and OL2 for the bond length to the O atom in the plane located at $z = 0.25$ along the c axis. The calculated values are plotted in figure 4-21 and both increase with temperature. This is due to the increasing size of the octahedra and the decrease in the Li displacement, resulting in a larger rate of increase for the OL1 bond length than the OL2.

The O-Ta bond lengths are plotted in figure 4-22 and are between the Ta atom and the O in the upper triad and the Ta and the O in the lower triad. The displacement of the Ta from the centre of the O octahedra decreases with temperature and results in an increase in the bond length to the O atoms in the upper triad and a decrease to the O atoms in the lower triad.

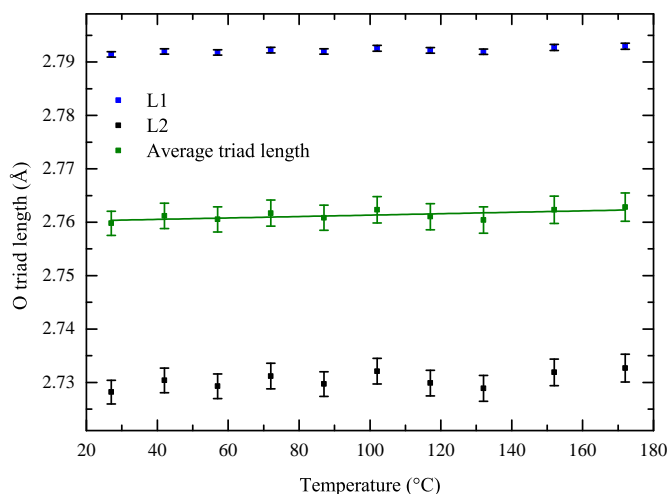


Figure 4-20 Triad lengths as a function of temperature. The lengths L1, L2 and their average are shown by the blue, black and green points, respectively.

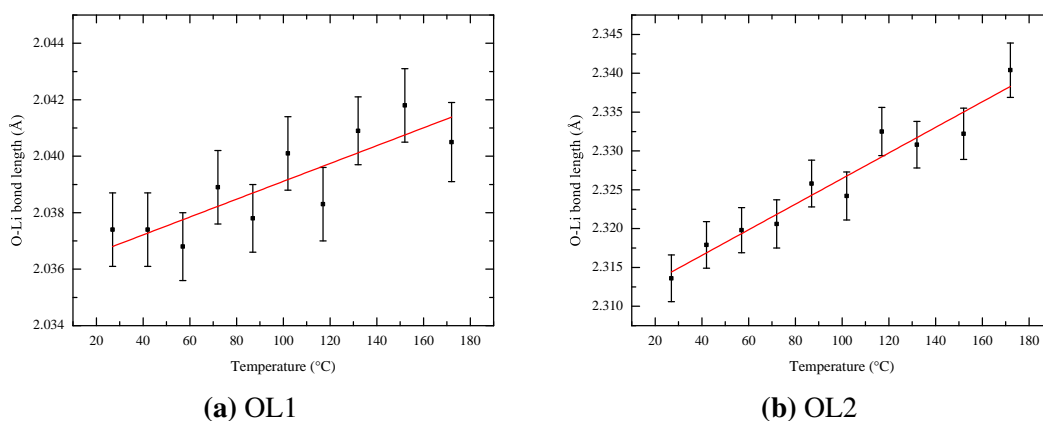


Figure 4-21 The Li-O bond length as a function of temperature for (a) O atom in the lower plane and (b) O in the upper plane.

4.3 Conclusions

The structure of Li-deficient LT has been studied between 48 and 50 mol % between room temperature and 820 °C using XRD measurements and between room temperature and 172 °C using neutron diffraction. It has been shown that the lattice parameters increase as the amount of Li is reduced below the stoichiometric ratio with a small initial decrease in the c lattice parameter. The FWHM of a Bragg peak measured on an LT powder sample can be used to confirm if it is Li deficient or stoichiometric.

The decrease in the amount of Li results in a decrease in the Ta displacement and the octahedral tilt. The Nb/Ta displacement and the octahedral tilt are linked and respond in a consistent way to changes in the the Li content, Nb/Ta content and temperature. Any

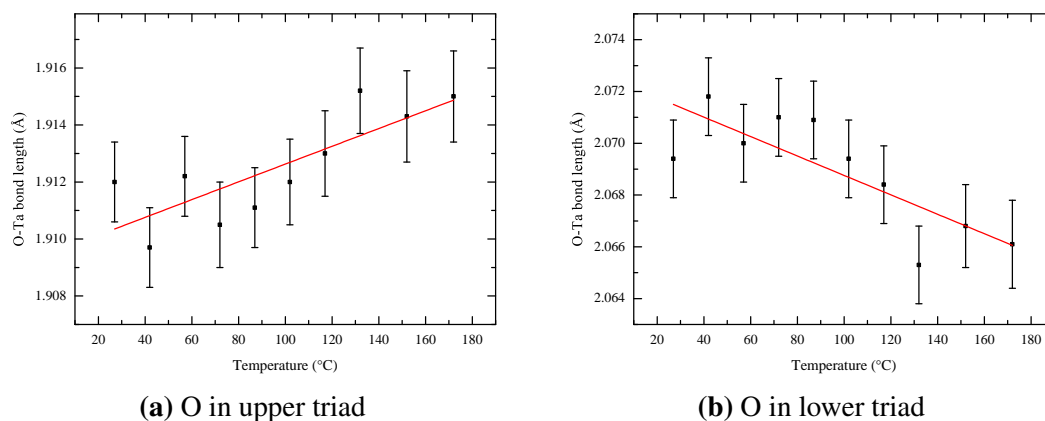


Figure 4-22 O-Ta bond lengths as a function of temperature with (a) O atom in the upper triad and (b) O atom in the lower triad.

decrease or increase in the Nb/Ta displacement is matched with a decrease or increase in the octahedral tilt.

The Curie point decreases in temperature and can be used as a measurement of the composition of LT. These measurements combined with those on LNT powders provide an understanding of the effect of both the Nb/Ta ratio and the Li content on the Curie point of LNT crystals.

References

- [1] A. Coelho, *Topas-academic v4.1* (2007), <http://www.topas-academic.net/>.
- [2] R. L. Barns and J. R. Carruthers, *Journal of Applied Crystallography* **3**, 395 (1970).
- [3] P. F. Bordui, R. G. Norwood, C. D. Bird, and J. T. Carella, *Journal of Applied Physics* **78**, 4647 (1995).
- [4] I. Bhaumik, S. Ganesamoorthy, R. Bhatt, A. K. Karnal, V. K. Wadhawan, P. K. Gupta, K. Kitamura, S. Takekawa, and M. Nakamura, *Journal of Applied Physics* **103**, 014108 (2008).
- [5] J. Kushibiki and Y. Ohashi, *IEEE Transactions on Ultrasonics, Ferroelectrics and Frequency Control* **53**, 385 (2006).

Single-crystal measurements

5.1 Experimental details

5.1.1 Single-crystal X-ray diffraction

Crystals of a good size and quality were polished to form crack free plates with a thickness between 200 and 450 μm . This plate is then cut into a cuboidal shape using a scalpel and attached to the end of a glass fibre with epoxy resin. The glass fibre was held in place on the goniometer using wax. All single-crystal diffraction measurements were performed on an Oxford diffraction Gemini diffractometer using $\text{MoK}\alpha$ radiation. Two different settings for the X-ray generator were used for the measurements: a high-intensity mode which also generated $\lambda/2$ X-rays and a mode with lower intensity which did not include $\lambda/2$ X-rays. A tension of 50 kV and 50 mA was used for the high-intensity mode and 33 kV and 35 mA was used for the lower intensity measurements. In crystals containing mechanical twins, the extra reflections from the $\lambda/2$ X-rays made it difficult to assign a lattice to the peaks from the twin. For crystals containing twins and providing sufficient time was available for the measurement, the lower intensity mode was used. Each data collection covered a full sphere to a resolution of 0.6 \AA and each collection was around 40 s depending on the total time available for the experiment. The overall time used for each experiment was between 16 and 64 h. Oxford Diffraction

tion's CrysAlisPro software was used for the initial data analysis which consisted of measuring the positions and intensities of the recorded peaks and fitting a lattice to the data.

Once a unit cell has been fitted to the data, unwarp images of the reciprocal lattice planes can be constructed. These images allow for the presence of twins within the crystal to be easily evaluated. Simulated $hk0$, $h0l$ and $0kl$ reciprocal space unwarp images are shown in figure 5-1 including the extra peaks from twinning in the (012) plane. The peaks from the main component are shown in black and the peaks from the twin component are red. For twinning in this plane, the $hk0$ and $h0l$ unwarp images do not contain any visible peaks due to the twinning. The effect of the twinning can be seen in the $0kl$ unwarp which contains a large number of weaker peaks from the twin. The reciprocal space unwarp images constructed using the twin lattice show that for certain orientations of the twin lattice strong peaks from the main crystal are measured. The space group was determined in CrysAlisPro and the collected intensities were corrected using the analytical method of Clark and Reid [1].

5.1.2 Energy dispersive X-ray spectroscopy

Energy dispersive X-ray spectroscopy (EDX) measurements were used to check the Nb and Ta content and the incorporation of impurities such as V in the LV flux grown crystals. Crystals were sputter-coated with carbon to reduce the charge build-up in the electron beam and allow EDX measurements. To further reduce the charge build-up silver paste was applied to the side of each crystal to improve the connection between the surface and the sample holder. The extra peaks measured because of the carbon coating are lower in energy than those of Nb and Ta and do not affect the the determination of their compositional ratio. EDX measurements were performed on a Zeiss Supra 55VP FEG SEM using the EDAX Genesis software.

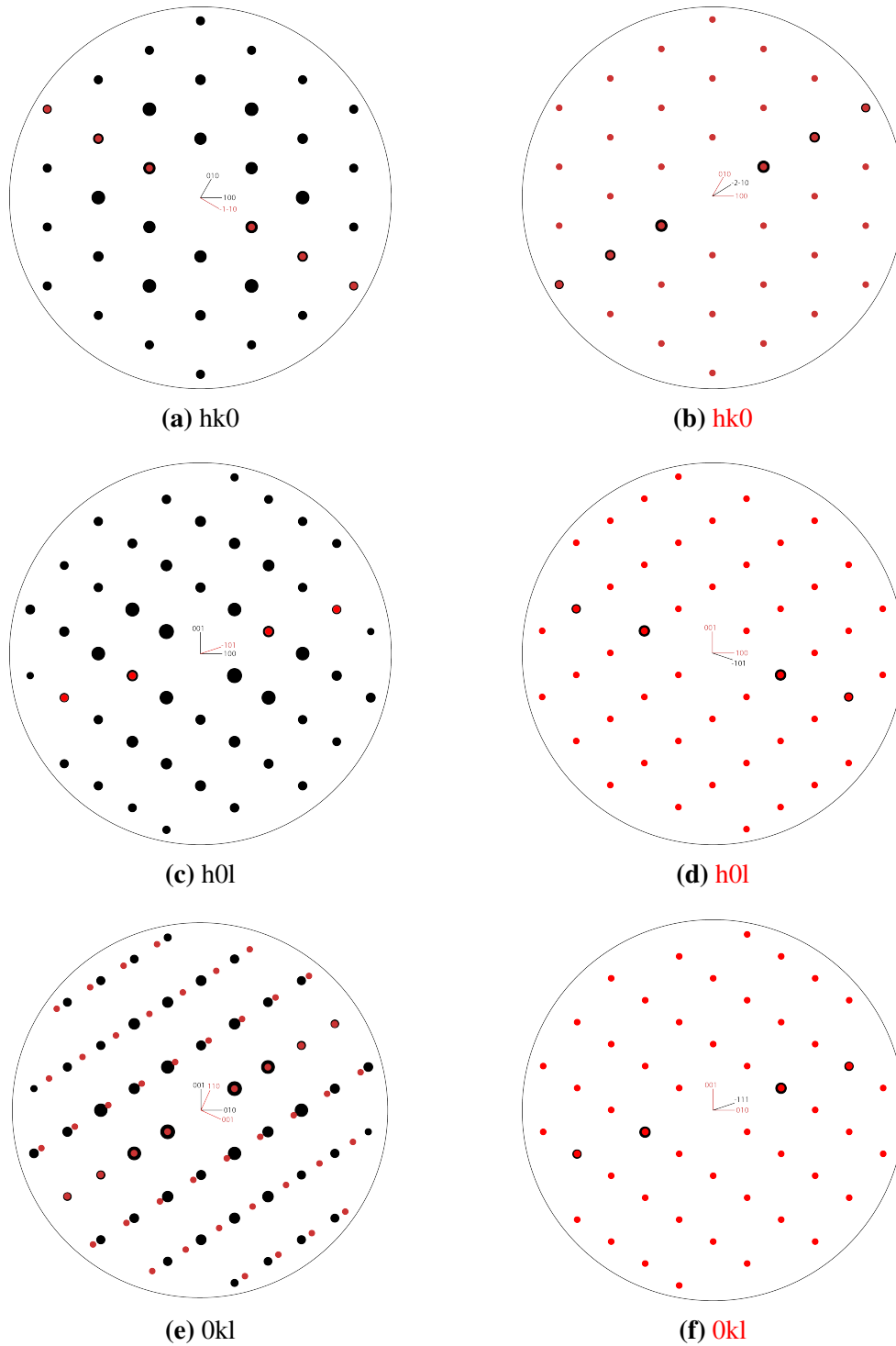


Figure 5-1 Reciprocal space unwarp simulations for LNT crystals containing a mechanical twin. Unwarps based on the main component and the twin component are on the left and right, respectively. Peaks from the main component are black and peaks from the twin are red.

5.2 Growth using a floating zone furnace

5.2.1 Experimental details

LNT powder with the initial composition of 94 mol % Ta was used for growth of single crystals using a floating zone furnace. The initial materials were hydrostatically pressed into rods. A molten zone was then created between two rods and passed along the whole length of the rod, this results in a denser crystalline rod which is then used to grow a crystal. Full details for the growth of LNT crystals using the floating zone technique are given in Bartasyte et al [2]. A large quantity of gas was given off during the melt zoning process and a high flow rate of O was required to keep a stable molten zone. This initial rod, however, was fragile and shattered into a large number of fragments upon removal from the furnace. The growth of LNT crystals using the floating zone furnace was abandoned due to the large amount of material required for each growth and the difficulties associated with successfully growing a single-crystal piece of LNT. However, the fragments of the initial rod were of sufficient size and quality to be used for structural and optical measurements.

5.2.2 Results and analysis

Single-crystal diffraction was performed using the high-intensity mode. The peak hunting software found 4100 peaks in the collected images and 63% of these were indexed on the expected hexagonal unit cell. Viewing the Ewald sphere of the collected peaks clearly showed that the crystal was twinned and a second hexagonal cell which contained 28 % of the collected peaks was found. Unwarp images of the reciprocal lattice planes are shown in figure 5-2 and match the simulated images in figure 5-1. This confirms the crystal is twinned and the twin plane is the (012). The unwarps of the main lattice contain peaks at $(h/2, k/2, l/2)$ because of the $\lambda/2$ X-rays generated in the high-intensity mode. The peaks from the $\lambda/2$ X-rays are too weak to be measured from the twin lattice.

The details of the data collection and analysis are shown in table 5-1. The angles between the lattice directions of the main lattice and the twin lattice have been calculated to confirm that the extra peaks are from a twin in the crystal. The angles between the lattice directions are shown in table 5-2 and they are consistent with those calculated

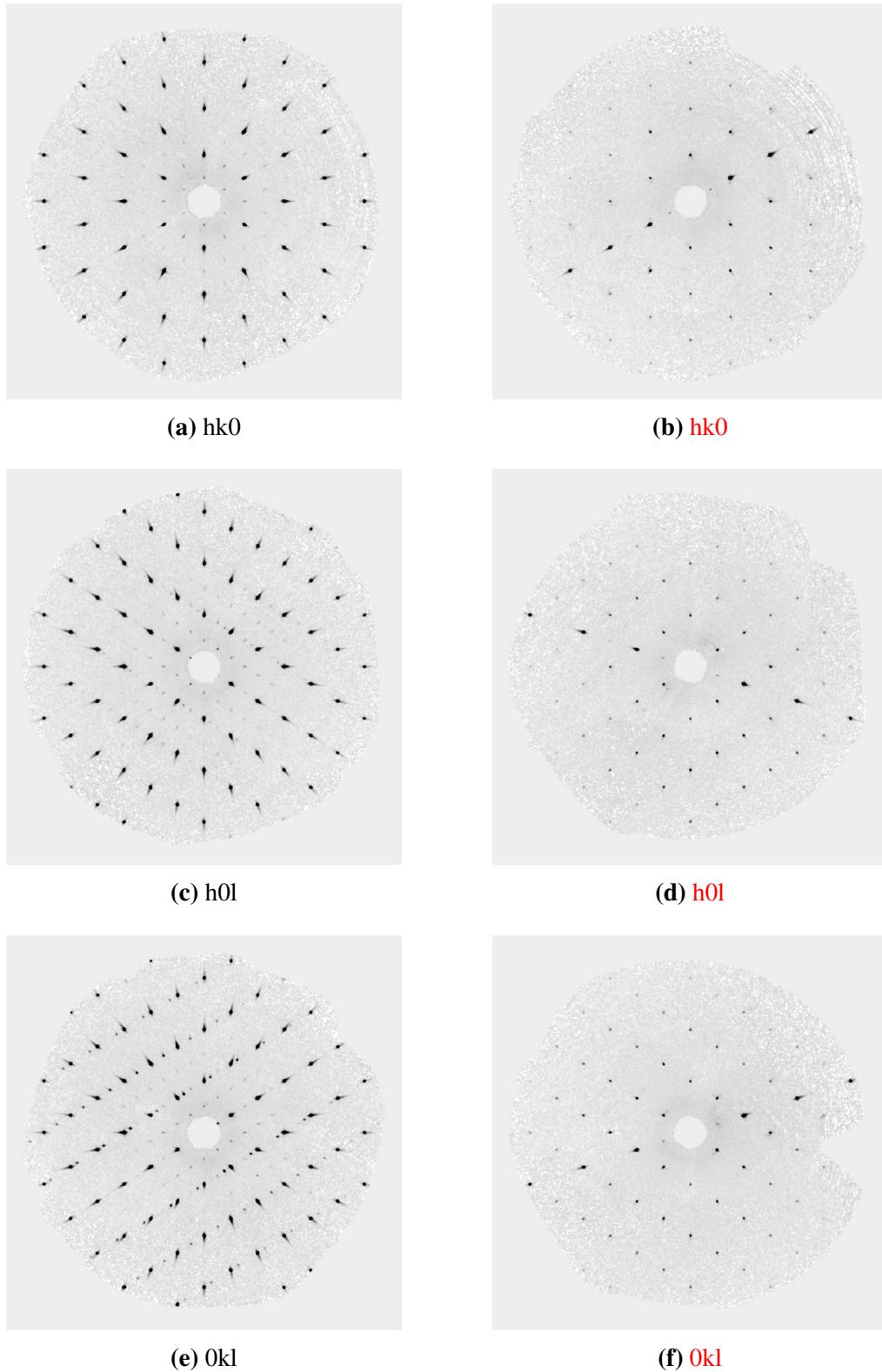


Figure 5-2 Reciprocal space unwarps for an LNT94 crystal containing a mechanical twin. Unwarps based on the main component and the twin component are on the left and right, respectively.

Table 5-1 Collection and refinement details from LNT94 single-crystal diffraction measurements.

Crystal	Main	Twin
a	5.1540(4) Å	5.1429(3) Å
b	5.1540(4) Å	5.1429(3) Å
c	13.755(13) Å	13.8397(4) Å
Volume	314.7(4) Å ³	317.01(3) Å ³
Absorption correction	51.663 µm ⁻¹	51.663 µm ⁻¹
Crystal size	cuboidal 150-200 µm	cuboidal 150-200 µm
Voltage	50 kV	50 kV
Current	40 mA	40 mA
Radiation	MoKα	MoKα
Scan width	0.5°	0.5°
Reflections collected	4100	4100
Reflections used	2596	1143
Overlapped reflections	340	340
Completeness	65.5 % to 0.5 Å	65.5 % to 0.5 Å

Table 5-2 Angles (°) between lattice directions.

	a1	a2	b1	b2	c1	c2
a1	-	119.9	120.0	120.0	90.1	89.9
a2	119.9	-	93.5	120.1	142.1	90.1
b1	120.0	93.5	-	55.9	90.0	38.0
b2	120.0	120.1	55.9	-	37.9	90.0
c1	90.1	142.1	90.0	37.9	-	114.4
c2	89.9	90.1	38.0	90.0	114.4	-

for twins measured in vapour transport equilibrium treated LT crystals by Glazer et al [3].

5.3 Growth using a lithium vanadate flux

5.3.1 Experimental details

Crystals were grown from the ceramic powders investigated in section 3, using a flux-growth method. A lithium vanadate (LV) flux was chosen because of its previous successful use in the growth of LN and LT layers onto a lithium tantalate substrate by Kondo et al [4]. A molar ratio of ten moles of LV to one mole of LNT was used to grow all the crystals. A three-zone vertical tube furnace with a maximum operating

temperature of 1500 °C was used for the flux growth. The maximum temperature required for growth was 1300 °C which was sufficiently below the maximum operating temperature of the furnace to ensure a stable operation. A large middle and two small heating zones at either end provided a steady temperature profile without any large temperature gradients across the middle zone. An iridium crucible with a platinum lid was used to hold the powders and was placed in the centre of the middle heating zone. The temperature profiles used for crystals were similar for all compositions with an initial heating at 180 °C h⁻¹ up to 1200 °C. This was followed by a slower heating rate of 20 °C up to 1300 °C and held for 24 h. The dwell at 1300 °C allows for the melted powders to homogenize. This heating profile was used for the initial heating of the material for all compositions of LNT. The cooling profile was different for each composition with a 1 °C h⁻¹ cooling rate to below the super-saturation point of each LNT composition in LV. LNT crystallizes out of solution as the temperature becomes less than the super-saturation point. The cooling profiles were changed according to the super-saturation temperature given in the LNT-LV phase diagram [4]. When the temperature was sufficiently below the super-saturation point, the cooling rate was increased to 60 °C h⁻¹, giving a total growth time for each crystal of 30 days. Further details on the flux growth of LNT crystals are given in Bartasyte et al [2].

Crystals were removed from the crucible by reacting the crystalline flux with dilute hydrochloric acid. They were then cleaned in water using an ultrasonic bath to ensure all the flux had been removed. A large quantity of green LNT crystals were produced which, were plate-like and cuboidal in shape. Many of the crystals were twinned and contained parts of the flux within them. The crystals lacking any of these defects were chosen for experiments. Due to the small size of the crystals, cutting to a desired orientation was not possible with the equipment available. Starting with the largest crystal face, the crystals were mechanically polished to produce a crystal plate with two parallel surfaces and a thickness of roughly 200-450 µm.

5.3.2 Crystal orientation

To measure the orientation of the polished crystals a PANalytical X'Pert Pro MRD equipped with a hybrid monochromator and a PIXcel detector was used. This provided a high-intensity source of CuK α_1 X-rays. The crystals were mounted onto a glass slide

using wax for the measurements. An ω - 2θ scan between 5 and 100° in 2θ was measured on each sample. The scan measured on LNT70 is shown in figure 5-3 which shows 3 peaks between 20 and 80° in 2θ . These are the (012), (024) and (036) Bragg peaks and gives the out-of-plane direction of the polished surface as the [012]. The surface orientation of all the polished LV flux grown samples was in the [012] direction and shows that the largest surface of the grown crystals was the same for all compositions. This preferred growth direction is consistent with the preferred orientation measured in section 3 on LNT powder samples and also the dominant cleavage planes in LT [5].

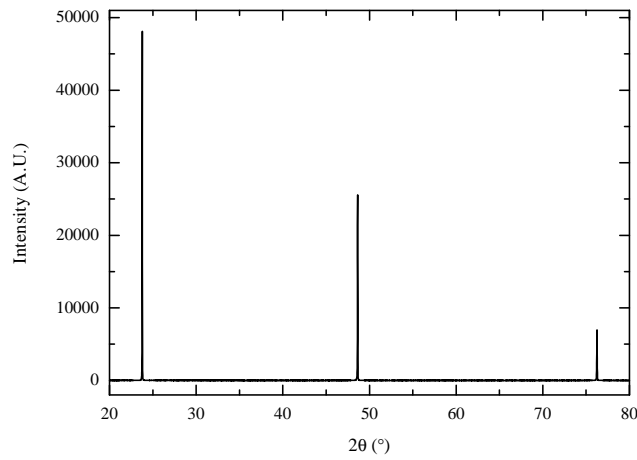


Figure 5-3 XRD ω - 2θ scan on LNT70 single crystal.

5.3.3 Composition

The measured EDX spectra of the LNT50 sample is shown in figure 5-4a. The energy of the electron beam was 20 keV which results in the O $K\alpha$ peak, Nb L series, Ta L series and the Ta M series of emission lines in the recorded spectra. A comparison of the measured spectra for all the LV flux grown crystals is plotted in figure 5-4b. This shows an increase in the intensity of the Ta $K\alpha$ and a decrease in the Nb $K\alpha$ as the amount of Ta in the crystals increases. The Nb and Ta content has been quantified using the Ta M series and Nb L series of peaks. The calculated compositions and the results of the single-crystal X-ray diffraction measurements on the LV flux grown crystals are collated in tables 5-3-5-13.

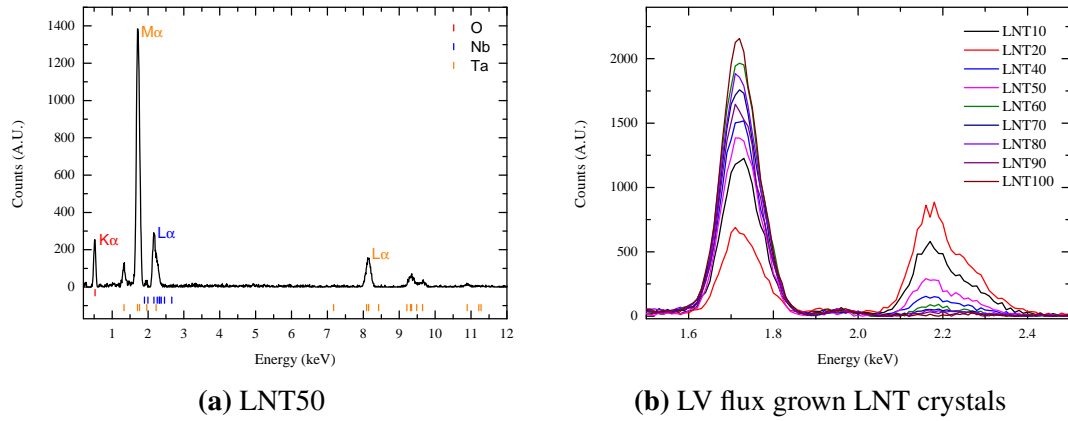


Figure 5-4 EDX measurements on (a) LNT50 crystal and (b) comparison of all LNT LV flux grown crystals.

Table 5-3 Refinement details for LNT0.

Composition	LiNbO ₃	Plate thickness	339(4) μm
Voltage	33 kV	Current	35 mA
Absorption correction	5.34 μm^{-1}	Scan width	0.5°
Reflections collected	13778	Reflections used	4006
Completeness	65.75 % to 0.5 Å	Crystal size	cuboidal 190-260 μm
a	5.146(1) Å	O _x	0.0478(1)
b	5.146(1) Å	O _y	0.3430(1)
c	13.857(5) Å	O _z	0.0798(2)
Volume	317.810(16) Å ³	Nb _z	0.0163(2)
Twins	Yes	Li _z	0.296(1)
Parameters	17	R _{obs}	1.91 %

5.3.4 Results and analysis

Single-crystal X-ray diffraction data have been refined following the procedure used for the crystal grown using the floating-zone furnace. In crystals which contained a twin, refinements were made taking into account the main lattice only. The majority of crystals have an R_{obs} of 1.8 to 2.8 %, with the LNT40, LNT80 and LNT90 having a value between 6 and 9 %. The structural refinements of these crystals are less reliable and result in the refined atomic positions having larger uncertainties. The lower data quality in these measurements was likely caused by a poor quality piece of crystal or a mis-alignment of the crystal with the X-ray beam.

Table 5-4 Refinement details for LNT10.

Composition	$\text{LiNb}_{0.47}\text{Ta}_{0.53}\text{O}_3$	Plate thickness	442(5) μm
Voltage	33 kV	Current	35 mA
Absorption correction	$29.87 \mu\text{m}^{-1}$	Scan width	0.5°
Reflections collected	6233	Reflections used	1411
Completeness	75.9 % to 0.6 \AA	Crystal size	82x146x119 μm
a	5.147(1) \AA	O_x	0.0478(3)
b	5.147(1) \AA	O_y	0.3427(3)
c	13.835(5) \AA	O_z	0.0676(5)
Volume	$317.41(2) \text{\AA}^3$	Nb/Ta _z	0.0013(5)
Twins	Yes	Li _z	0.281(3)
Parameters	17	R _{obs}	2.45 %

Table 5-5 Refinement details for LNT20.

Composition	$\text{LiNb}_{0.7}\text{Ta}_{0.3}\text{O}_3$	Plate thickness	157(15) μm
Voltage	33 kV	Current	35 mA
Absorption correction	$19.25 \mu\text{m}^{-1}$	Scan width	0.5°
Reflections collected	13868	Reflections used	3736
Completeness	65.8 % to 0.5 \AA	Crystal size	cuboidal 200 μm
a	5.146(1) \AA	O_x	0.0481(2)
b	5.146(1) \AA	O_y	0.3434(2)
c	13.842(5) \AA	O_z	0.0678(3)
Volume	$317.480(12) \text{\AA}^3$	Nb/Ta _z	0.0027(3)
Twins	Yes	Li _z	0.280(2)
Parameters	17	R _{obs}	2.3 %

Table 5-6 Refinement details for LNT30.

Composition	$\text{LiNb}_{0.4}\text{Ta}_{0.6}\text{O}_3$	Plate thickness	-
Voltage	33 kV	Current	35 mA
Absorption correction	$33.26 \mu\text{m}^{-1}$	Scan width	0.5°
Reflections collected	13452	Reflections used	2997
Completeness	33.26 % to 0.5 \AA	Crystal size	cuboidal 150-230 μm
a	5.148(1) \AA	O_x	0.0491(2)
b	5.141(1) \AA	O_y	0.3431(3)
c	13.799(5) \AA	O_z	0.0689(4)
Volume	$316.642(16) \text{\AA}^3$	Nb/Ta _z	0.0013(4)
Twins	Yes	Li _z	0.282(2)
Parameters	17	R _{obs}	2.02 %

Table 5-7 Refinement details for LNT40.

Composition	$\text{LiNb}_{0.22}\text{Ta}_{0.78}\text{O}_3$	Plate thickness	249(6) μm
Voltage	33 kV	Current	35 mA
Absorption correction	$41.62 \mu\text{m}^{-1}$	Scan width	0.5°
Reflections collected	14538	Reflections used	2240
Completeness	65.75 % to 0.5 \AA	Crystal size	cuboidal 190-220 μm
a	$5.148(1) \text{ \AA}$	O_x	0.042(2)
b	$5.148(1) \text{ \AA}$	O_y	0.330(3)
c	$13.789(5) \text{ \AA}$	O_z	0.069(2)
Volume	$316.484(15) \text{ \AA}^3$	Nb/Ta _z	0.001(1)
Twins	Yes	Li _z	0.282(7)
Parameters	17	R _{obs}	7.35 %

Table 5-8 Refinement details for LNT50.

Composition	$\text{LiNb}_{0.36}\text{Ta}_{0.64}\text{O}_3$	Plate thickness	298(2) μm
Voltage	33 kV	Current	35 mA
Absorption correction	$35.16 \mu\text{m}^{-1}$	Scan width	0.5°
Reflections collected	14680	Reflections used	3057
Completeness	65.75 % to 0.5 \AA	Crystal size	cuboidal 130-180 μm
a	$5.150(1) \text{ \AA}$	O_x	0.0485(3)
b	$5.150(1) \text{ \AA}$	O_y	0.3420(4)
c	$13.786(5) \text{ \AA}$	O_z	0.0688(5)
Volume	$316.61(2) \text{ \AA}^3$	Nb/Ta _z	0.0013(4)
Twins	Yes	Li _z	0.286(2)
Parameters	17	R _{obs}	2.28 %

Table 5-9 Refinement details for LNT60.

Composition	$\text{LiNb}_{0.11}\text{Ta}_{0.89}\text{O}_3$	Plate thickness	480(23) μm
Voltage	33 kV	Current	35 mA
Absorption correction	$46.8 \mu\text{m}^{-1}$	Scan width	0.5°
Reflections collected	14913	Reflections used	3394
Completeness	65.8 % to 0.5 \AA	Crystal size	cuboidal 220-330 μm
a	$5.151(1) \text{ \AA}$	O_x	0.0496(2)
b	$5.151(1) \text{ \AA}$	O_y	0.3436(2)
c	$13.780(5) \text{ \AA}$	O_z	0.0694(4)
Volume	$316.61(2) \text{ \AA}^3$	Nb/Ta _z	0.0011(4)
Twins	Yes	Li _z	0.282(2)
Parameters	17	R _{obs}	1.84 %

Table 5-10 Refinement details for LNT70.

Composition	$\text{LiNb}_{0.08}\text{Ta}_{0.92}\text{O}_3$	Plate thickness	201(12) μm
Voltage	33 kV	Current	35 mA
Absorption correction	48.13 μm^{-1}	Scan width	0.5°
Reflections collected	8145	Reflections used	1780
Completeness	65.5 % to 0.5 Å	Crystal size	cuboidal 150-220 μm
a	5.149(1) Å	O _x	0.0502(3)
b	5.149(1) Å	O _y	0.3445(4)
c	13.787(5) Å	O _z	0.0693(6)
Volume	316.57(3) Å ³	Nb/Ta _z	0.0014(5)
Twins	Yes	Li _z	0.283(4)
Parameters	17	R _{obs}	2.63 %

Table 5-11 Refinement details for LNT80.

Composition	$\text{LiNb}_{0.04}\text{Ta}_{0.96}\text{O}_3$	Plate thickness	423(5) μm
Voltage	33 kV	Current	35 mA
Absorption correction	49.8 μm^{-1}	Scan width	0.5°
Reflections collected	13457	Reflections used	2895
Completeness	65.21 % to 0.5 Å	Crystal size	cuboidal 140-230 μm
a	5.149(1) Å	O _x	0.0497(6)
b	5.149(1) Å	O _y	0.3431(5)
c	13.772(5) Å	O _z	0.071(3)
Volume	316.186(19) Å ³	Nb/Ta _z	0.001(1)
Twins	Yes	Li _z	0.28(1)
Parameters	17	R _{obs}	8.79 %

Table 5-12 Refinement details for LNT90.

Composition	$\text{LiNb}_{0.04}\text{Ta}_{0.96}\text{O}_3$	Plate thickness	174(3) μm
Voltage	33 kV	Current	40 mA
Absorption correction	49.82 μm^{-1}	Scan width	0.5°
Reflections collected	15663	Reflections used	3301
Completeness	65.75 % to 0.5 Å	Crystal size	cuboidal 200-300 μm
a	5.151(1) Å	O _x	0.0498(5)
b	5.151(1) Å	O _y	0.3441(4)
c	13.776(5) Å	O _z	0.069(2)
Volume	316.53(2) Å ³	Nb/Ta _z	0.001(1)
Twins	Yes	Li _z	0.28(1)
Parameters	17	R _{obs}	6.24 %

Table 5-13 Refinement details for LNT100.

Composition	LiTaO ₃	Plate thickness	417(2) μm
Voltage	33 kV	Current	40 mA
Absorption correction	52.04 μm^{-1}	Scan width	0.5°
Reflections collected	13612	Reflections used	2892
Completeness	65.75 % to 0.5 Å	Crystal size	cuboidal 200-290 μm
a	5.149(1) Å	O _x	0.0496(3)
b	5.149(1) Å	O _y	0.3436(3)
c	13.768(5) Å	O _z	0.070(2)
Volume	316.08(2) Å ³	Nb/Ta _z	0.0011(7)
Twin	Yes	Li _z	0.283(5)
Parameters	17	R _{obs}	2.69 %

5.3.4.1 Lattice parameters

The measured a lattice parameters for the single crystals are plotted in figure 5-5a along with the fit to the powder measurements in section 3.2. The errors in the lattice parameters have been estimated from the scatter of the values measured across the compositional range. The LV flux grown crystals are marked by the black squares and show an increase with LT content. This agrees with the expected trend measured on powder samples of LNT. The a lattice parameters measured for the flux grown crystals are less than those measured on the powder samples, which is likely because of the lower accuracy in determining lattice parameters using the single-crystal diffraction technique. The LNT94 crystal produced using a floating zone furnace has a higher a lattice parameter than those produced using a LV flux, which is consistent with the observation of Li₂O being lost during the growth process.

The c lattice parameters as a function of LT content are plotted in figure 5-5b. The c lattice parameters of the LV flux grown samples decrease with increasing LT content as expected from the measurements on powder samples. The c lattice parameter of the LNT 94 crystal has a lower value than the LV flux grown crystals, which is consistent with the drop measured in the LT powders.

5.3.4.2 Atomic positions

The Ta displacement as a function of composition is plotted in figure 5-6a and shows that the displacement increases linearly as the amount of Nb decreases. This is consis-

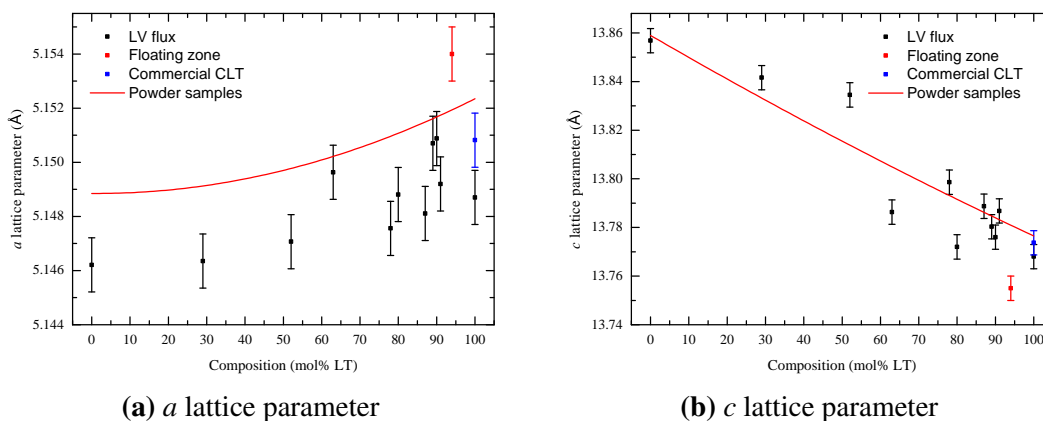


Figure 5-5 The (a) *a* lattice parameter and (b) *c* lattice parameter as a function of composition for single crystals of LNT. The black data are LV flux grown crystals, the red point is the floating zone grown crystal and the blue is a commercial piece of CLT. The red line is the fit to the powder data measured in section 3.2.

tent with the measurements on LNT powders in section 3.2. The Ta displacement measured on the LT crystal is 0.20 ± 0.01 which agrees with the value of 0.198 ± 0.004 Å measured on a powder SLT sample in section 3.2 and 0.20 ± 0.01 measured on a single crystal of LT using neutron diffraction by Abrahams et al [6]. The Nb displacement in the LN crystal was measured to be 0.275 ± 0.003 which agrees well with the value of 0.27 ± 0.01 measured by Abrahams et al on an SLN crystal using neutron diffraction [7]. The close agreement between these values suggests that the LN crystal grown using the LV flux is close to the stoichiometric Li content. The Nb and Ta displacements measured on the single crystals show that the small range of composition investigated using powder XRD was not enough to accurately calculate the displacements in low-Ta content LNT.

The Li displacement is plotted in figure 5-6b and shows the Li displacement refines to between 0.6 and 0.7 Å for all crystal compositions. The determination of the Li position is inaccurate because of the small X-ray scattering factor of Li and hence the lack of information in the data: however, the refined values are consistent with the values determined on LNT powders in section 3 and the displacement of 0.601 ± 0.004 Å determined using powder neutron diffraction on LT in section 4.2.

The octahedral distortion does not change as a function of composition and is plotted in figure 5-6c. The crystals have a distortion between -0.002 and -0.003, which is consistent with the LNT powders measured using XRD: the majority of composi-

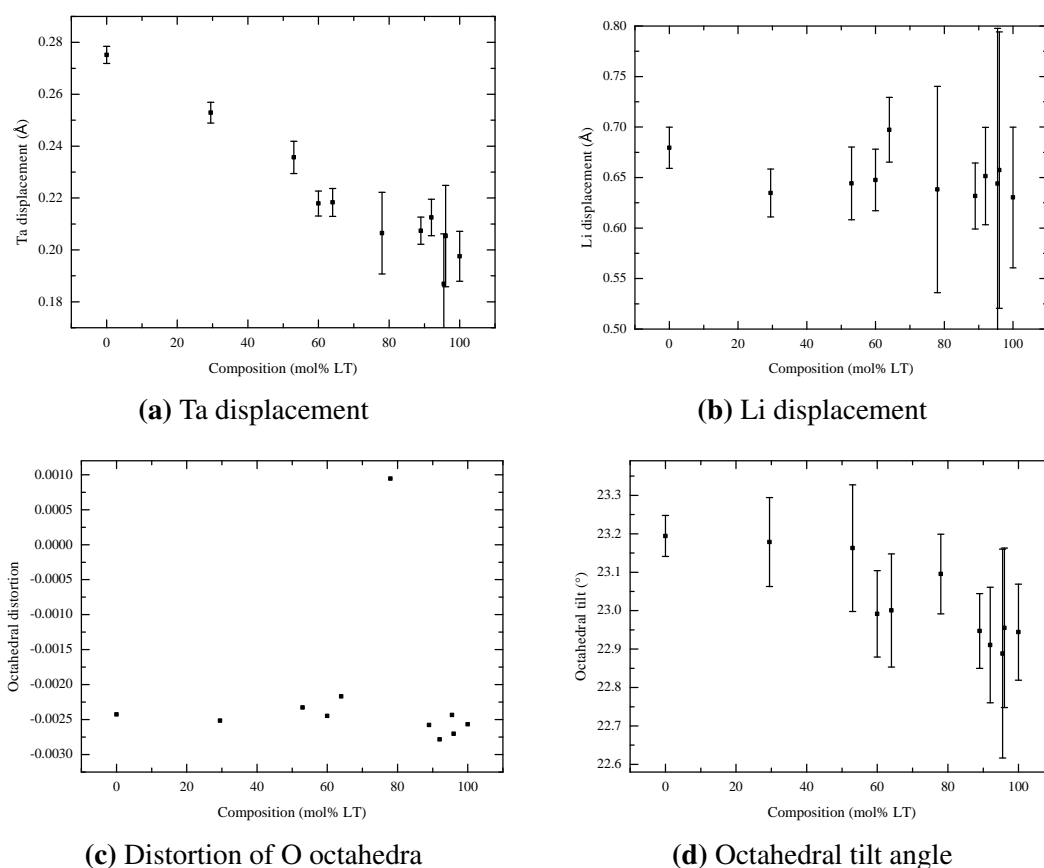


Figure 5-6 Parameters from refinements of LV flux grown LNT crystals, the (a) Ta displacement, (b) Li displacement, (c) octahedral distortion and (d) octahedral tilt angle are shown.

tions had distortions between -0.0024 and -0.0032. The octahedral tilt increases from $22.94 \pm 0.12^\circ$ for LT to $23.19 \pm 0.05^\circ$ for LN and is plotted in figure 5-6d. These values agree well with the previously measured values of 22.9° and 23.1° measured on LT and LN, respectively [6, 7]. The measured trend in the tilt of the single crystals shows that the trend measured in the high-Ta content LNT powders was incorrect and an accurate determination of the O positions using powder XRD was not possible, further justifying the use of the single-crystal studies reported here.

5.3.4.3 Curie point

The intensity of the SHG signal as a function of temperature has been used to measure the Curie point of high-Ta content crystals. The maximum operating temperature of the furnace was 750°C which limited the compositional range that could be measured to above 90 mol % LT. A sufficiently large piece of crystal was required such that it could

be mounted in the furnace and positioned in the path of the laser. This was possible for the LV flux grown LNT90 and LNT100 crystals and a commercial piece of CLT. The maximum intensity of the fundamental and secondary signals were then measured every 1 °C while heating and cooling between 500 and 750 °C.

The normalised SHG intensity measured during the heating and cooling of the LNT100 crystal is plotted in figure 5-7. The SHG signal decreases with increasing temperature until it reaches a constant background level and this gives the temperature of the Curie point. The Curie point measured for LNT100 is 667 ± 4 °C and for CLT is 600 ± 4 °C. The errors are because of the accuracy of the furnace and the difficulty in determining when the signal reaches the background level. The value measured for the CLT sample agrees well with the value of 603.0 °C precisely determined by Kushibiki et al [8]. For the LNT100 samples the composition is 49.70 ± 0.20 mol % Li content according to Curie point measurements on LT powders in figure 4-11 and shows that the LT crystal does not form stoichiometrically using an LV flux.

The Curie point in stoichiometric LNT powders increases as the amount of Ta is decreased, consistent with the results of the high-temperature XRD measurements in section 3.3.2. The Curie point of the LNT90 crystal was measured to be 674 ± 4 °C which is very close to the value of 667 ± 4 °C measured on LNT100. The Ta content of the LNT90 crystal is 96 ± 2 % and is consistent with the Curie point being slightly higher than that of the LT crystal.

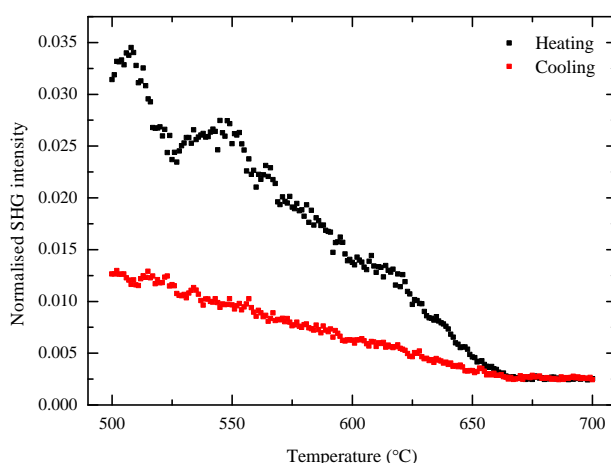


Figure 5-7 Normalised SHG intensity as a function of temperature during heating of a LV flux grown LNT100 crystal.

5.4 Commercially-grown lithium tantalate

5.4.1 Piezoresponse

A Z-cut (polished faces perpendicular to the c -axis) piece of commercially grown CLT purchased from MTI Corporation, was used to determine the absolute structure. The crystal is poled during growth to produce a single-crystal boule, which can be cut into plates of the desired orientation. The crystal is a Z-cut plate 10x10x0.5 mm with both surfaces polished. The +Z and -Z faces of the crystal plate were coated in silver and connected to a high voltage power supply to confirm the crystal was fully poled. After applying the silver to both surfaces, the piezoelectric coefficient was measured as 6.3 pC N^{-1} using a d_{33} meter. A d_{33} meter works by applying an oscillating force to the crystal and measuring the resulting charge, with the d_{33} coefficient being the ratio between them. A range of increasing voltages were applied to the crystal and the resulting piezoelectric coefficient was measured. The crystal was fully poled after applying a field of 26 kV mm^{-1} for 1 min. The piezoelectric coefficient of the fully poled crystal was measured to be $7.4 \pm 0.4 \text{ pC N}^{-1}$ with the silvered surfaces. The silver was then removed using acetone and the piezoelectric coefficient was measured as $8.9 \pm 0.3 \text{ pC N}^{-1}$. The surface corresponding to the positive direction of the piezoelectric coefficient was marked with non-water based pen.

5.4.2 Absolute structure determination

5.4.2.1 Experimental details

The absolute atomic arrangement can be determined using the poled single crystal and can be related to the sense of the ferroelectric polarization given by the measurements of the piezoelectric coefficient. The plate was carefully cut using a scalpel while maintaining the marked surface denoting the positive piezoelectric coefficient. A cuboidal shaped piece of the crystal with dimensions roughly $100\text{-}200 \mu\text{m}$ was prepared for the single-crystal diffraction experiment. The pen marking the positive surface was removed using acetone while washing off the vacuum grease and any other crystal fragments. The crystal was then attached to a glass fibre with the polarisation direction of the crystal perpendicular to the length of the glass fibre. This allowed measurements of

Table 5-14 Refinement details for poled CLT crystal.

Composition	CLT	Plate thickness	500 μm
Voltage	33 kV	Current	40 mA
Absorption correction	51.848 μm^{-1}	Scan width	0.5°
Reflections collected	16012	Reflections used	3739
Completeness	65.2 % to 0.5 Å	Crystal size	cuboidal 150-240 μm
a	5.151(1) Å	O _x	0.0499(2)
b	5.151(1) Å	O _y	0.3435(2)
c	13.774(5) Å	O _z	0.0705(6)
Volume	316.470(11) Å ³	Nb/Ta _z	0.0009(1)
Twin	No	Li _z	0.285(3)
Parameters	18	R _{obs}	2.51 %

both (00n) and (00-n) reflections in the diffraction experiment.

5.4.2.2 Results and analysis

The parameters and results of the diffraction measurements are in table 5-14. The Flack parameter was refined to be 0.00 ± 0.13 which confirms the piece of crystal prepared for the diffraction measurement is single domain and that the absolute structure has been correctly determined relative to the data collection, i.e. +Z for the refinement corresponds to +Z for the crystal axis. The piezoelectric coefficient is in the same direction as the displacement of the Ta atom from the centre of the O octahedra. This is in agreement with the direction determination by Abrahams et al [6] using the measurements of the sense of the pyroelectric axis.

The Ta displacement is calculated to be 0.188 ± 0.002 Å, which is similar to the calculated value for the LV flux grown crystal of 0.20 ± 0.02 which had a measured Li content of 49.70 ± 0.20 mol %. It is expected from the powder diffraction measurements on LT samples in section 4.1 that the displacement decreases as the Li-content decreases. The displacement in the LV flux grown crystal has not been determined accurately enough to confirm this trend. The Li displacement is 0.66 ± 0.04 Å and agrees within the errors to the expected range of between 0.58 and 0.64 Å calculated from the LT powder measurements.

The octahedral distortion is -0.00253 ± 0.00001 and agrees with the previously refined values using powder LT and LNT samples. The tilt angle is $22.89 \pm 0.11^\circ$ which

is very close to the the value of $22.94 \pm 0.12^\circ$ calculated for the LV flux grown LNT100 sample. The errors in the values determined using single-crystal XRD measurements are too large to confirm the possible trend measured on LT powders, which showed a small decrease in tilt angle in the Li-deficient samples.

5.5 Conclusions

The growth of single crystals of LNT has been performed using a floating zone furnace and an LV flux growth technique. In both growth methods it has been shown that mechanical domains on the (012) plane can form. Using a floating zone furnace results in Li-deficient crystals because of a loss of Li_2O during growth. The LV flux growth technique produces crystals with a small reduction of roughly 0.5 mol % Li_2O .

The LV flux growth technique has been successfully used to grow crystals across the full compositional range, including both LN and LT. EDX and SHG measurements have shown that the crystals grow Ta-rich compared to the initial materials and a signal from V incorporation was not measurable using EDX. Refinements of single-crystal XRD measurements have shown that the Nb/Ta displacement increases as the amount Ta in the crystals decreases. This is in agreement with powder XRD measurements in section 3.2. The accuracy in determining the Li and O positions is lower because of their low scattering factors. However, the results confirmed the expected increase in the octahedral tilt angle with decreasing Ta content.

For the first time the absolute structure of LT has been determined using direct measurements of the piezoelectric d_{33} coefficient and single-crystal XRD measurements. The positive sense of the polarisation is in the same direction as the Ta displacement from the centre of the O octahedra.

References

- [1] R. C. Clark and J. S. Reid, *Acta Crystallographica* **A51**, 887 (1995).
- [2] A. Bartasyte, A. M. Glazer, F. Wondre, D. Prabhakaran, P. A. Thomas, S. Huband, D. S. Keeble, and S. Margueron, *Materials Chemistry and Physics* **134**, 728 (2012).
- [3] A. M. Glazer, N. Zhang, A. Bartasyte, D. S. Keeble, S. Huband, P. A. Thomas, I. Gregora, F. Borodavka, S. Margueron, and J. Hlinka, *Journal of Applied Crystallography* **45**, 1030 (2012).
- [4] S. Kondo, K. Sugii, S. Miyazawa, and S. Uehara, *Journal of Crystal Growth* **46**, 314 (1979).
- [5] A. M. Glazer, N. Zhang, A. Bartasyte, D. S. Keeble, S. Huband, and P. A. Thomas, *Journal of Applied Crystallography* **43**, 1305 (2010).
- [6] S. C. Abrahams, W. C. Hamilton, and A. Sequeira, *Journal of Physics and Chemistry of Solids* **28**, 1693 (1967).
- [7] S. C. Abrahams, W. C. Hamilton, and J. M. Reddy, *Journal of Physics and Chemistry of Solids* **27**, 1013 (1966).
- [8] J. Kushibiki and Y. Ohashi, *IEEE Transactions on Ultrasonics, Ferroelectrics and Frequency Control* **53**, 385 (2006).

CHAPTER 6

Optical measurements and calculations

Birefringence measurements were performed using the Metripol equipment in conjunction with a Linkham THMS600 furnace. All samples were heated and cooled between 30 and 600 °C at a rate of 1 °C min⁻¹ with measurements made every 1 °C. A temperature run was collected using the 550, 570, 590 and 600 nm filters for each sample. Images were collected using the 10x objective lens and data analysis was performed on a 12x12 pixel square sufficiently far away from any visible scratches or defects. The analysis was performed while taking into account the movement of the sample to ensure the same area of the sample was investigated at each temperature.

6.1 Birefringence measurements

6.1.1 Floating zone LNT94 crystal

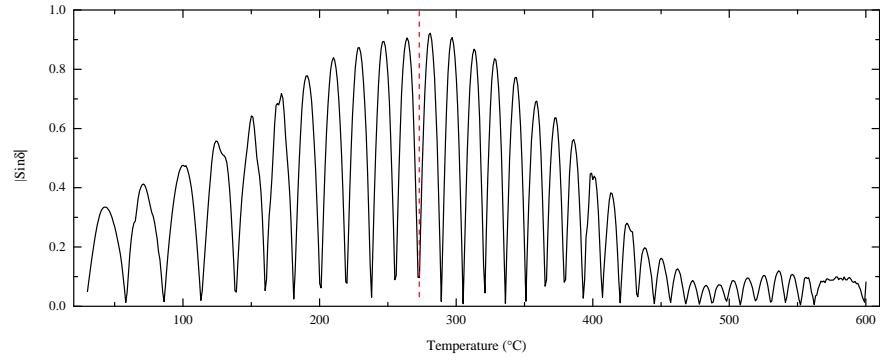
The measured $|\sin\delta|$ using each wavelength is plotted in figure 6-1. As described in section 2.2, the $|\sin\delta|$ oscillates between a maximum and a minimum, with one minimum occurring when the sample becomes zero-birefringent. According to Shimura et al [1] the birefringence is relatively constant as a function of wavelength. This allows the zero-birefringence point to be determined without an absolute measurement of the refractive indices. As the sample becomes zero-birefringent, a trough in the plot of $|\sin\delta|$

will be measured at the same temperature using each wavelength. This position has been marked in figure 6-1 and gives a zero-birefringence point at $274 \pm 2^\circ\text{C}$. This method for determining the zero-birefringence point has been checked using measurements at 550 nm on one sample with two different thicknesses to confirm the zero-birefringence point has been determined at the correct temperature. The zero-birefringence temperature coincides with the centre of the peak in the measured signal of $|\sin\delta|$.

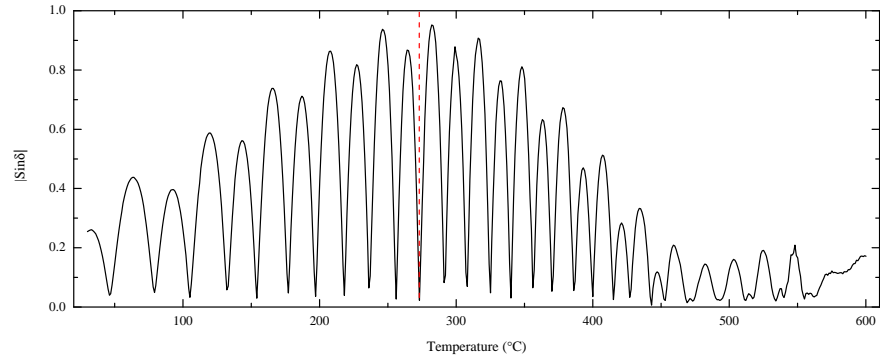
6.1.2 LV flux crystals

Birefringence imaging measurements between 30 and 600°C were performed on LV flux-grown crystals using light with a wavelength of 550, 570, 590 and 600 nm. The birefringence of the samples could not be determined because of the [012] out-of-plane direction of the polished samples. For crystals in this orientation the plano-birefringence is measured, which for these crystals is the difference between n_o and $n_e \cos(57.2)$, where the angle between the [001] and [012] directions is 57.2° . However, the determination of the zero-birefringence point is unaffected by this because the plano-birefringence will also be zero when the indicatrix becomes a sphere. The measured $|\sin\delta|$ as a function of temperature of the LV flux grown samples using a wavelength of 550 nm is plotted in figure 6-2. The zero-birefringence point was calculated and is plotted as a function of the composition in figure 6-3. This shows the expected increase in temperature of the zero-birefringence point with decreasing Ta content as measured by Wood et al [2]. The zero-birefringence point was only measurable for samples with a composition between 50 and 100 mol % LT because of the maximum operating temperature of the Linkham furnace used. Similar to the measurements on the float zone crystal in figure 6-1, a peak in the measured $|\sin\delta|$ signal coincides with the zero-birefringence point of the crystal.

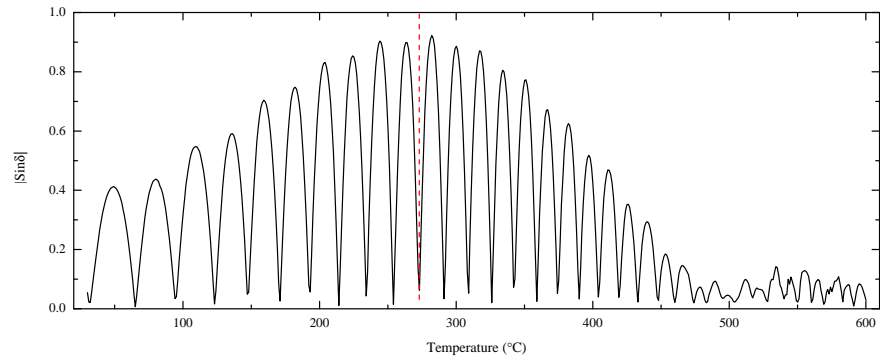
The profile measured in the $|\sin\delta|$ signal is similar to measurements on a 69 mol % Ta LNT crystal grown using the top seeded solution growth technique by Glazer et al [3]. There is a peak centred on when the crystal becomes zero-birefringent and a small peak either side, above and below this the signal drops to a background value. The measured $|\sin\delta|$ is expected to oscillate with a maximum value of 1 as shown in figure 2-5b, the low values measured either side of the zero-birefringence point are usually because of small domains in the crystal, which scatter the light [3]. This is consistent with



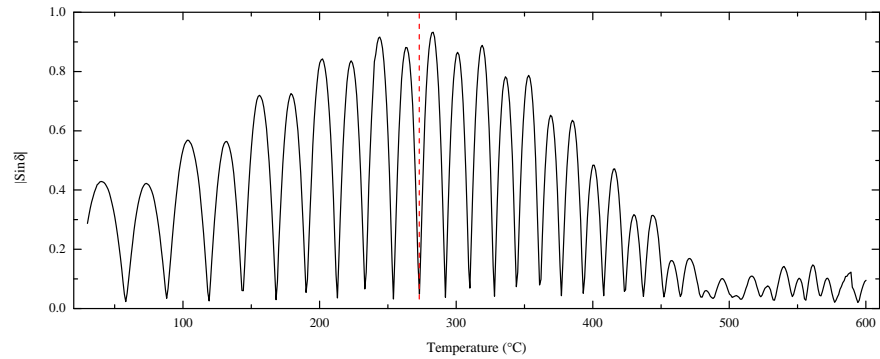
(a) 550 nm



(b) 570 nm



(c) 590 nm



(d) 600 nm

Figure 6-1 $|\sin\delta|$ as a function of increasing temperature for the float zone grown LNT94 crystal using light with a wavelength of (a) 550 nm, (b) 570 nm, (c) 590 nm and (d) 600 nm.

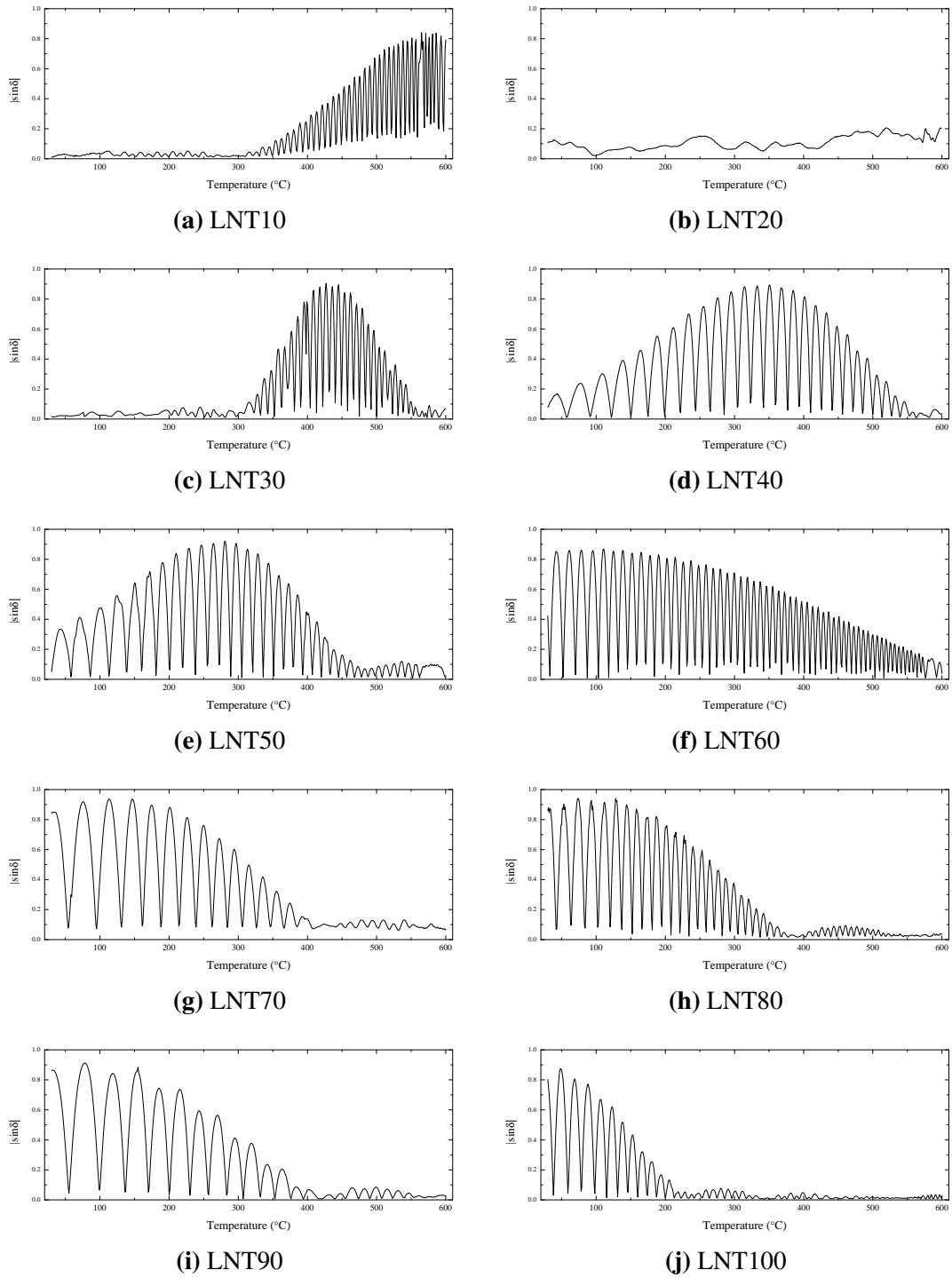


Figure 6-2 $|\sin\delta|$ as a function of temperature on LV flux grown samples using a wavelength of 550 nm.

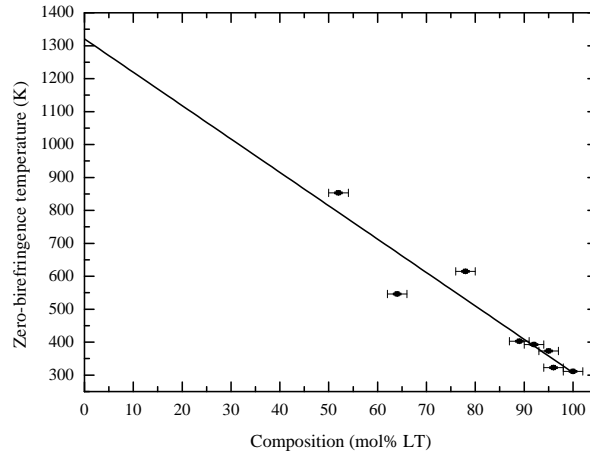


Figure 6-3 Measured zero-birefringence temperature as a function of composition of the LV flux grown crystals.

the results of the single-crystal X-ray diffraction measurements on LNT crystals, which confirmed the crystals contained polar domains in the Z-direction and mechanical twins in the (012) plane. The full $|\sin\delta|$ is measured at the zero-birefringence point because the refractive indices of the different domains are now the same. As the birefringence increases or decreases from zero, the refractive indices between the mechanical domains are no longer the same and the light is scattered.

The measured $|\sin\delta|$ of the crystals in figure 6-2 shows the zero-birefringence point decreasing as the amount of Ta in the crystals increases. All the measurements show a peak in the signal measured at the zero-birefringence point and all but LNT60 have the same shape as that measured by Glazer et al. The peak centred at the zero-birefringence point in LNT60 is much wider, which suggests that the LNT60 sample has formed with less mechanical twins than the other samples. The composition of the LNT20 crystal was measured to be 29 mol % and the measured $|\sin\delta|$ value is low because the zero-birefringence point of this composition is above 600 °C.

The measured zero-birefringence point of LNT100 in figure 6-2 is 37 ± 2 °C. The zero-birefringence temperature of VTE treated LT crystals as a function of Li content was investigated by Bäumer et al [4] and using these data, we calculate a composition of 49.60 ± 0.05 mol % for our LNT100 sample, which shows it has grown with a Li deficiency. The calculated composition from birefringence measurements agrees with the composition determined using measurements of the Curie point. The measured profile suggests that this crystal also contains mechanical domains.

The linear fit to the measured zero-birefringence points in figure 6-3 can be used to calculate a value for an LN crystal. This gives a zero-birefringence point of roughly 1040 °C, which is significantly higher than that of a CLN crystal which was measured to be 880 °C [3]. The zero-birefringence point of the LT sample is 140 °C higher than that of a CLT crystal [4]. This trend agrees with the predicted zero-birefringence of the LN sample in this study.

6.1.3 Commercially-grown LT

Metripol measurements were made on a commercially-grown X-cut (polished faces perpendicular to the a -axis) CLT crystal also purchased from MTI Corporation. The measured $|\sin\delta|$ as a function of temperature using the 550 nm filter is plotted in figure 6-4. The thickness of the sample was 500 μm which results in a large number of oscillations in the measured $|\sin\delta|$ signal. The measured profile drops to a background level at 500 °C and then increases again above this, similar to measurements on the LNT crystals. This suggests the CLT crystal contains mechanical domains.

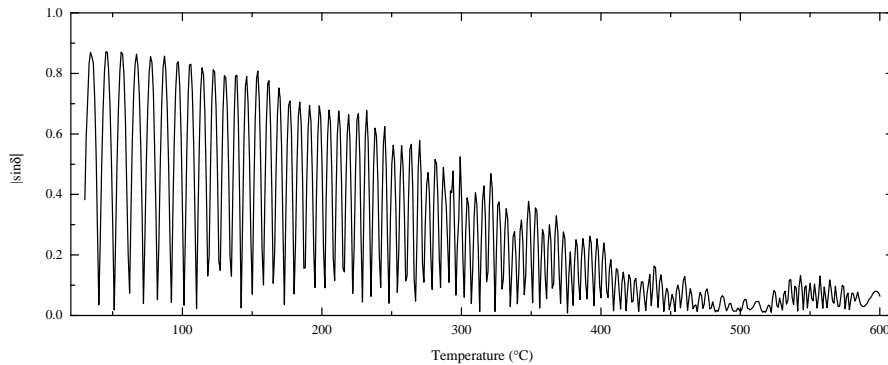


Figure 6-4 Measured $|\sin\delta|$ of X-cut commercial CLT crystal as a function of temperature using a 550 nm filter.

It was shown in section 5.4 that the commercially-grown piece of Z-cut CLT contained polar domains and these multiple polar domains could be removed with the application of a high voltage. To investigate the measured $|\sin\delta|$ of this poled crystal, a section was cut perpendicular to the surface. This piece was then polished on both sides to allow measurements of the $|\sin\delta|$ perpendicular to the c axis. The measured $|\sin\delta|$ is plotted in figure 6-5 for light with a wavelength of 550, 570, 590 and 600 nm. These measurements have a different profile compared to those measured on the LNT

samples and the X-cut CLT crystal, in particular, the absence of the zero and small subsequent maximum. The measured $|\sin\delta|$ signal decreases with increasing temperature at a slower rate than that measured in the X-cut crystal. This suggests the mechanical domain content of this Z-cut crystal is less than the X-cut crystal.

6.2 DFT calculations using Wien2k

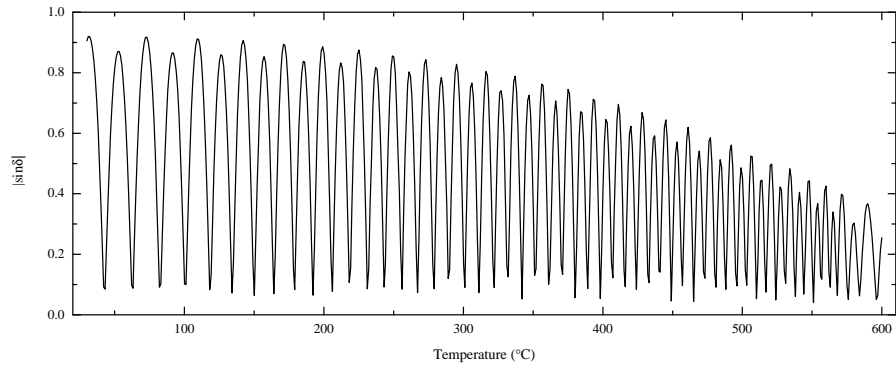
6.2.1 Introduction

Single-particle DFT calculations have been performed using WIEN2k, with a focus on the optical properties of LT. These calculations have been based on the resulting structures from Rietveld refinements of the neutron diffraction measurements on SLT in section 4.2. Calculations have also been made on the structure resulting from the linear fits applied to the refined Megaw parameters and following this the effect of each atom on the optical properties has been investigated. The exchange correlation potential used for these calculations is the PBE-GGA developed by Perdew, Burke and Ernzerhof [5] and the muffin-tin radii are taken to be 1.69, 1.89 and 1.63 a_0 for the Li, Ta and O atoms, respectively. All refractive index values are for a wavelength of 550 nm.

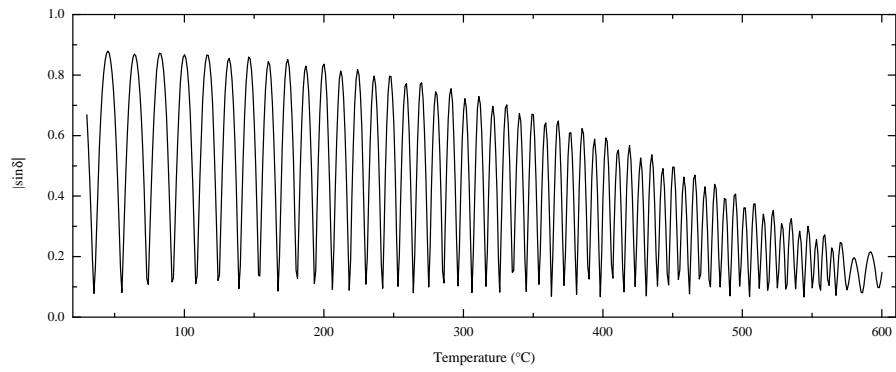
6.2.2 Convergence of calculations

Using an initial $R_{MT}K_{MAX}$ of 6, the total energy and the n_e as a function of the k-mesh size was investigated. The size of the k-mesh was changed from 10 to 5000 k-points to check the value required for converged calculations. The dependency of the total energy and the n_e on the size of the k-mesh is plotted in figure 6-6. This shows that the total energy of the system has already reached convergence with the initial 10 k-points used in the calculation. The refractive index is much more sensitive to the amount of k-points and only converges when around 1000 k-points are used. The amount of time required for a calculation is heavily dependent on the number of k-points, therefore 1000 k-points were utilised for calculations. This allowed for converged calculations whilst using the lowest processing time possible.

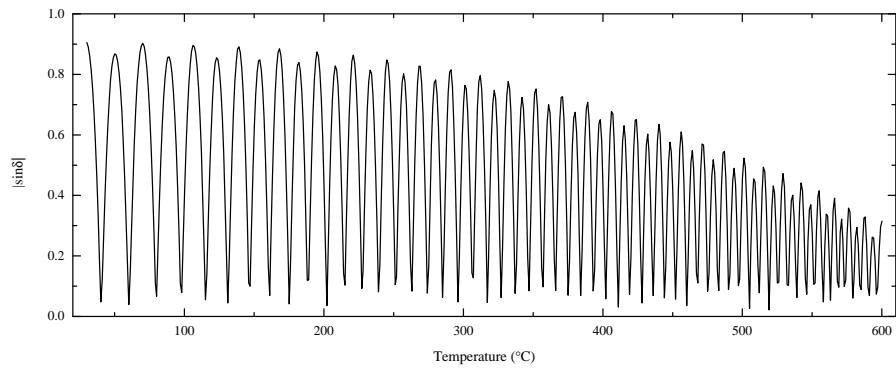
With the number of k-points in the k-mesh set to 1000, the effect of the $R_{MT}K_{MAX}$ on the convergence of the calculations was investigated. The $R_{MT}K_{MAX}$ was varied from



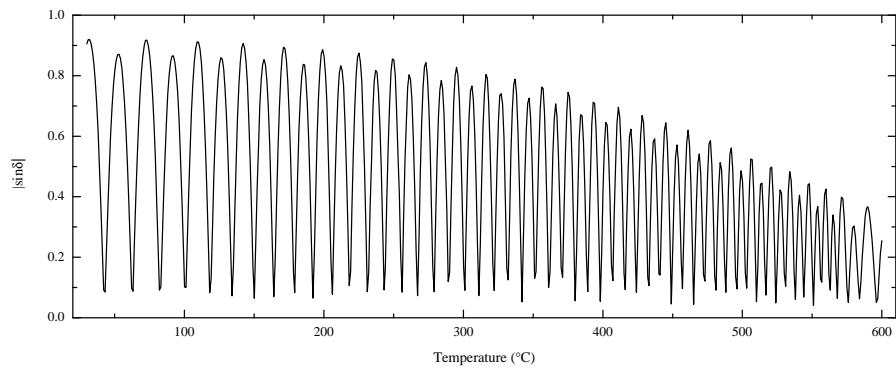
(a) 550 nm



(b) 570 nm



(c) 590 nm



(d) 600 nm

Figure 6-5 $|\sin\delta|$ as a function of increasing temperature for the poled commercial Z-cut crystal using light with a wavelength of (a) 550 nm, (b) 570 nm, (c) 590 nm and (d) 600 nm.

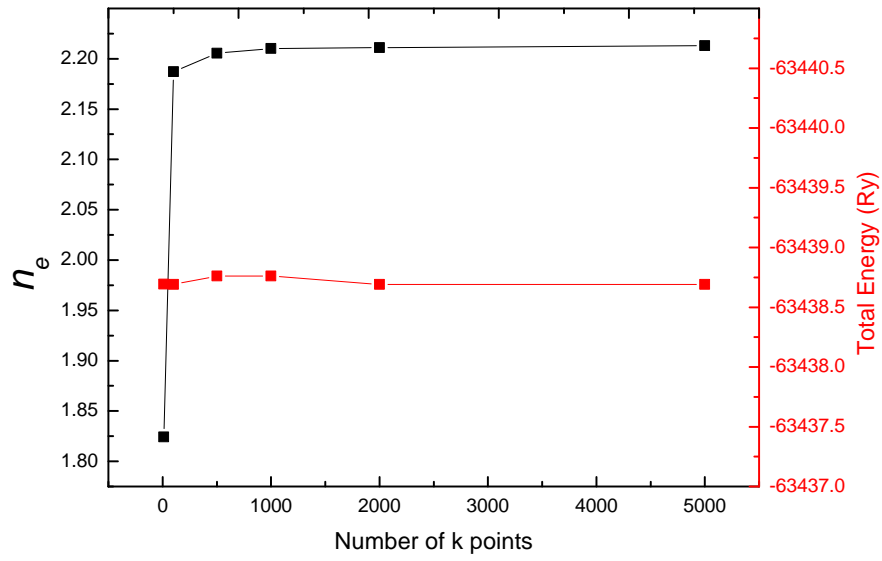


Figure 6-6 n_e and total energy as a function of k points used in a calculation. Refractive index values are shown in black and total energy values are shown in red.

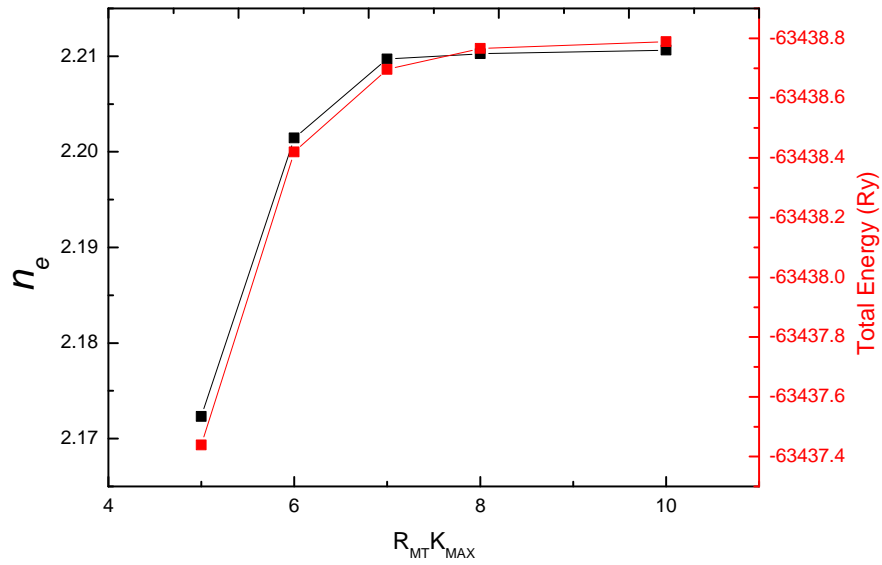


Figure 6-7 n_e and total energy as a function of the $R_{MT}K_{MAX}$ used in a calculation. Refractive index values are shown in black and total energy values are shown in red.

5 to 10 and its effect on the total energy and the n_e is plotted in figure 6-7. The change in the total energy and refractive index show that the calculations fully converge when $R_{MT}K_{MAX}$ is set to 10. However, as extra processor time was required for each increase in the $R_{MT}K_{MAX}$ value, a lower value than 10 was subsequently used. An $R_{MT}K_{MAX}$ of 7 provides a reasonable time for each calculation and is within a percent of the converged values for both the total energy and the n_e .

6.2.3 Results of calculations on SLT

The bandstructure calculated for LT at 27 °C has been plotted in figure 6-8. The direct band gap is located at the Γ point and is 3.8 ± 0.1 eV, the errors are estimated from the change in the calculated band gap from the measured structure at 27 °C and that calculated for the structure given by the linear fits to the Megaw parameters. The calculated value agrees well with other single-particle calculations using a range of different DFT codes and functionals. The band gap was calculated to be 3.86 eV using LDA in the ABINIT code by Cabuk et al and 3.71 eV using the PW91 functional in the VASP code by Rieffer et al [6, 7]. A small range in the band gap values is expected as a result of using different functionals and different structural parameters. In this study, the structure was calculated using the neutron diffraction measurements. The calculated value of the band gap in this work agrees closely with the experimental value of 3.93 eV measured using optical methods by Cabuk et al [8]. This close agreement between the calculated and the measured value is unexpected because of the usual underestimation of the band gap calculated using DFT on semiconductors and insulators and does not confirm the validity of the calculation. One of the methods used to correct the underestimation of the calculated band gaps is to include the self-energy of the system using the GW approximation and electron-hole interactions, increasing the calculated value to 5.65 eV [7].

A similar trend is evident between the calculated and measured band gap values for LN. It was suggested by Thierfelder et al that the agreement between the single-particle DFT calculations and the measured direct band gap was because of a cancellation between the exciton binding energy and the electronic self-energy [9]. They calculate the direct band gap to be 4.7 eV using the GW approximation to include the effect of quasi-particles and the exciton binding energy. Following this the experimental band gap was measured for crystals with a range of Li compositions. The band gap for LN was measured to be 4.12 eV by Bhatt et al which was larger than the initially calculated value of 3.78 eV by Dhar et al [10, 11]. This increase, however, is not large enough to remove the discrepancy between the measured and calculated direct band gap values.

The calculated refractive indices and the birefringence of the structures for each temperature have been plotted in figure 6-9. The errors have been estimated using the change in measured values between the initially calculated values and those calculated

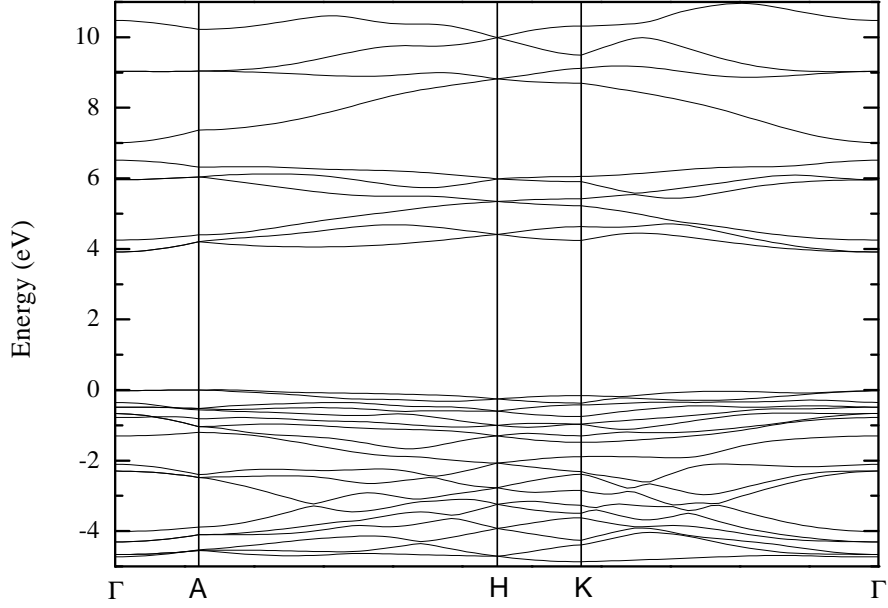


Figure 6-8 The electronic band structure calculated from the refined structure of LT at 27 °C.

after averaging the Megaw parameters. The value of the n_e at 27 °C is calculated to be 2.213 ± 0.002 which is close to the experimentally measured value of 2.194, measured by Bruner et al [12] but not within the uncertainties of the calculated value. The structural changes as the temperature is increased results in the n_e increasing, which is fitted by a linear trend in figure 6-9a.

The n_o also shows a linear increase with temperature with a value of 2.241 ± 0.001 at 27 °C which does not agree with the previously measured value of 2.198 by Nakamura et al [13]. A small change in value across the temperature range, suggests the n_o is not very sensitive to the changes in the structure as the temperature is increased. The total change in the value of the n_o is 0.00542 which is considerably less than the change of 0.01391 in the value of the n_e . This larger change in the n_e results in the birefringence increasing with temperature, as is expected from the experimental measurements. The birefringence at 27 °C is calculated to be -0.027 ± 0.001 which doesn't agree with the measured value of -0.005 for SLT [14]. Recent DFT calculations using the GW approximation have produced a birefringence value of 0.005 for a CLT based structure [7], but the corresponding values for the refractive indices in this study have not been published. The large variation between the calculated values using DFT is due to the inclusion of quasiparticles and electron-hole interactions. DFT calculations of the optical properties of insulators are very sensitive to the band gap. By shifting the values of the calculated

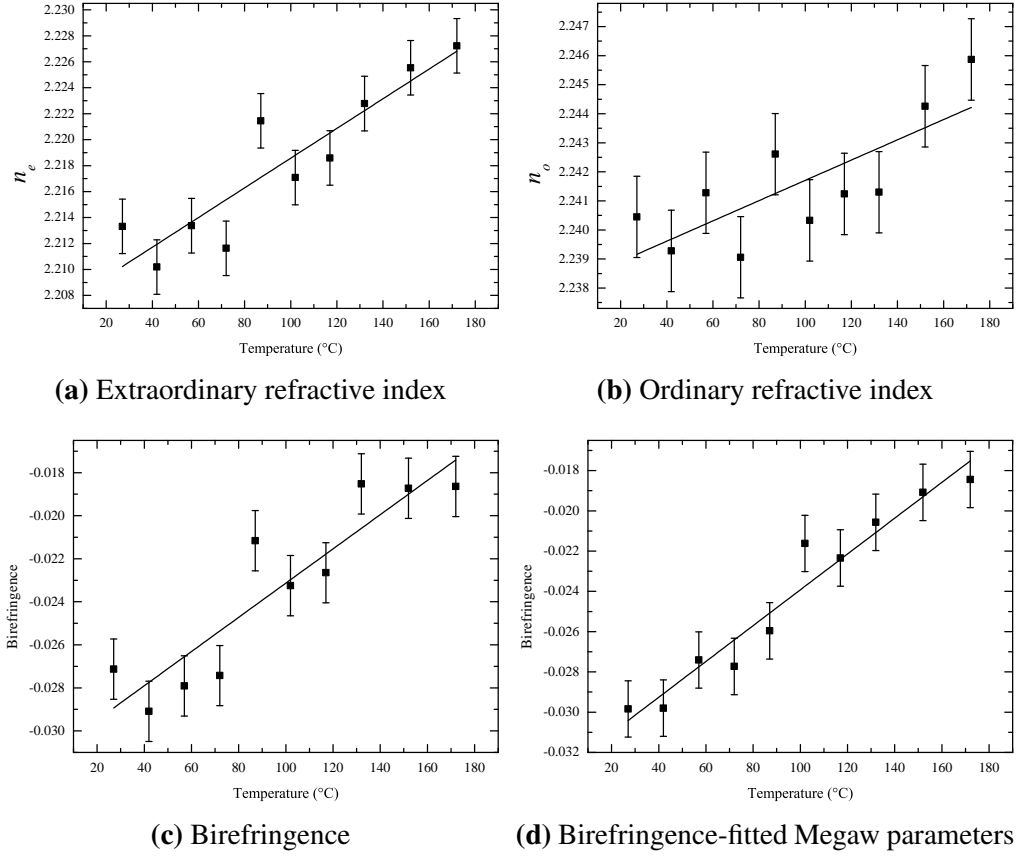


Figure 6-9 The (a) extraordinary refractive index, (b) ordinary refractive index, (c) birefringence and (d) birefringence from fitted structures of SLT at 27 °C calculated using DFT.

birefringence so that the value at 27 °C agrees with the measured value, the temperature at which SLT has zero birefringence can be predicted. This occurs at 90 °C and agrees well with the measured value of 100 °C [4].

By using the values of the Megaw parameters from the fits to the refined values in section 4.2, the birefringence can be calculated from structures with a smooth linear change in the atomic positions. The results of these calculations are plotted in figure 6-9d. The linear trend is the same as in figure 6-9c but with less scatter of the points about the linear fit.

6.2.4 The effect of each atom on the optical properties

The effect each type of atom has on the optical properties of the material can be investigated by repeating the DFT calculations as a function of temperature and only allowing one type of atom to move. For these measurements the structures from the fit-

ted Megaw parameters are used to provide a linear variation in the atomic positions as the temperature increases. To investigate the effect of only one atom type moving, the lattice parameters of the structure at 27 °C have been used for all temperatures, while the atomic position of a single atom type is varied. By changing the lattice parameters and keeping the the atomic positions at those of the structure at 27 °C, the change in the optical properties from the volume expansion can also be investigated. The uncertainties in the calculated values are the same as those for the calculations on the LT structure in section 6.2.3.

6.2.4.1 Extraordinary refractive index

The values of n_e from these calculations have been plotted in figure 6-10. As the temperature increases and the position of the Li is changed, the n_e increases linearly with a small peak at 100 °C. The change in n_e because of the movement of the Ta atom is very close to the change calculated when all the atoms and are allowed to move. The movement of the O results in a linear decrease in the value of n_e as the temperature increases. These plots show that the value of the n_e of SLT is largely affected by the movement of the O and Ta, with the Li having a small effect. The increase of the lattice parameters produces a small linear increase in the value of n_e .

6.2.4.2 Ordinary refractive index

The values of n_o from the DFT calculation performed on structures with one parameter varying as a function of temperature are shown in figure 6-11. With only the positions of Li atoms moving, the increasing temperature results in an overall decrease in the n_o . The points at 72, 87 and 102 °C have a deviation from the overall linear decrease. These three points suggest a large peak occurs in the data centred on 100 °C. The height of this peak is almost as high as the total increase in the n_o for calculations with all the parameters varying. The n_e data does not show a pronounced peak in the same position which shows this effect is orientation dependent. The change in the Ta position produces a similar trend to the data when all the parameters are varied. A large decrease in the value of n_o results from the movement of the O atoms, which is greater than the total increase of n_o when all the parameters are varied. The increase in the lattice parameters also results in a large change in the calculated n_o values, producing a linear increase

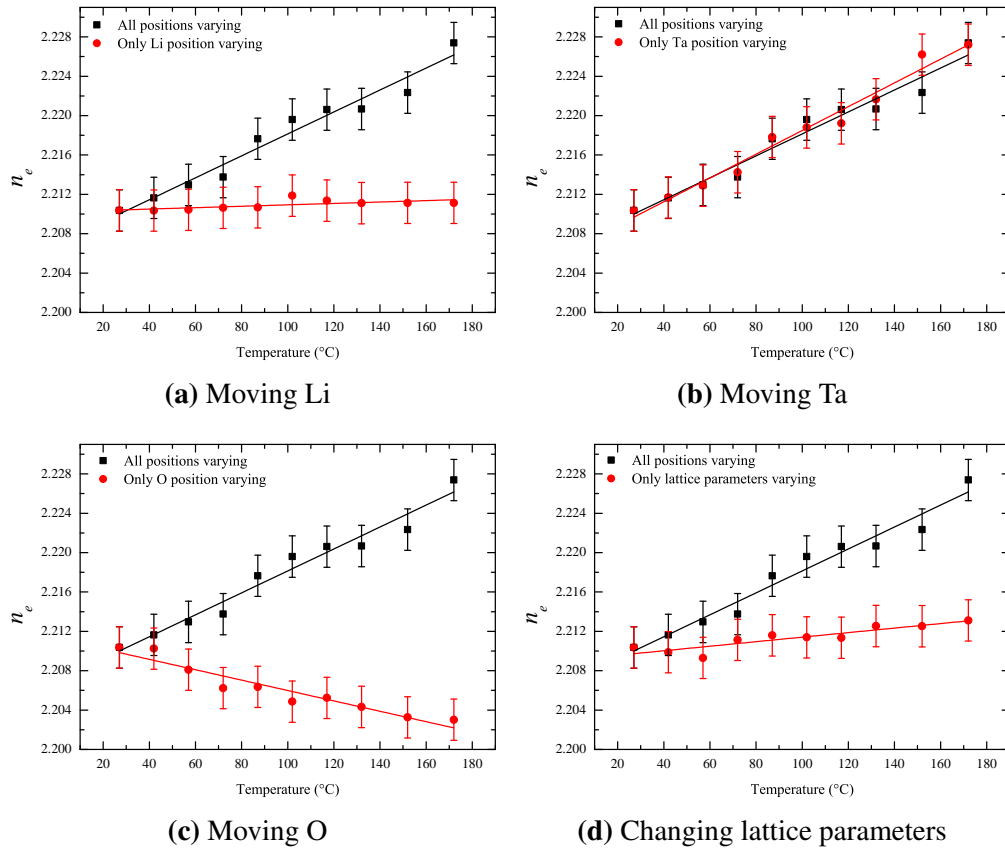


Figure 6-10 The n_e as a function of temperature for the movement of the (a) Li atoms, (b) Ta atoms, (c) O atoms and (d) and the changing lattice parameters are plotted in red. The n_e of the fitted Megaw parameters is plotted in black.

greater than the total increase when all parameters are varied.

6.2.4.3 Birefringence

Using the values of the n_e and the n_o , the birefringence is calculated and is plotted in figure 6-12. The decrease in the n_o because of the movement of the Li is larger than the increase in the n_e and this results in a small increase in the birefringence with temperature. The peak in the n_o produces a trough in the birefringence centred on 95 °C. This feature is not apparent in the birefringence data calculated when all the parameters are varied, which suggests it is an artifact of allowing only the Li atoms to move in the structure. Movement of the Ta atoms causes a change in the birefringence that matches the birefringence when all the parameters in the structure are varied. With both the n_e and n_o decreasing because of the movement of the O, the birefringence stays constant as a function of temperature. The decrease in the value of n_o as the lattice parameters

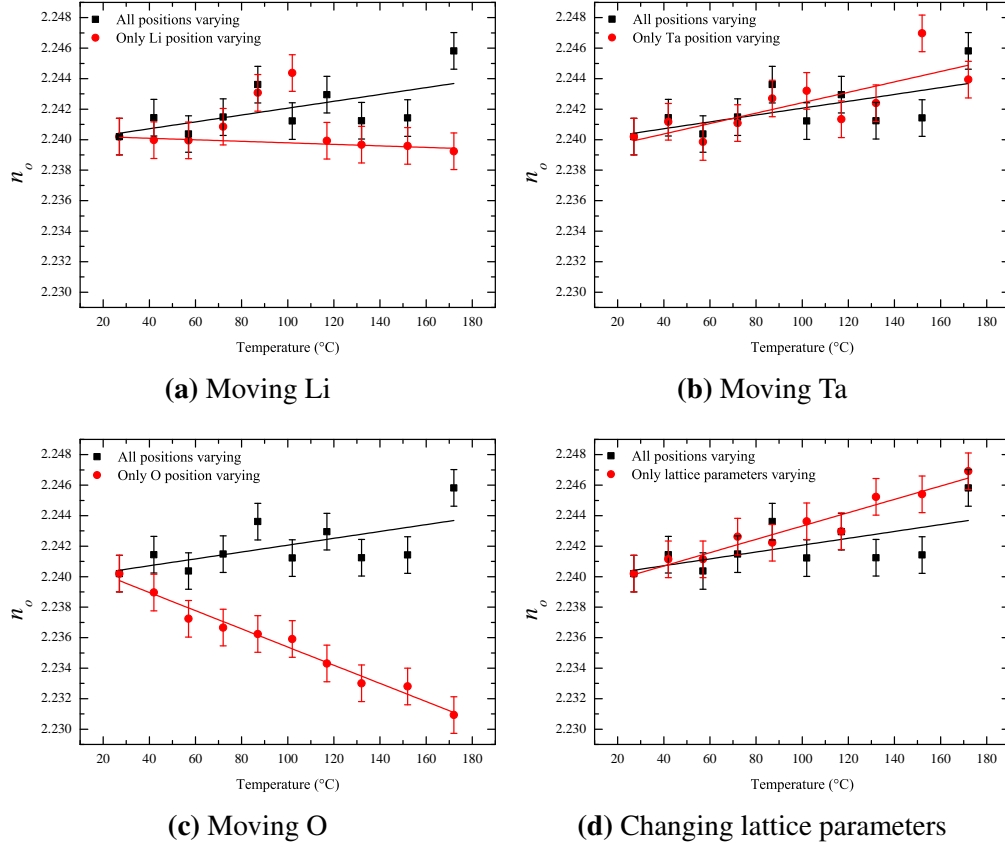


Figure 6-11 The n_o as a function of temperature for the movement of the (a) Li atoms, (b) Ta atoms, (c) O atoms and (d) and the changing lattice parameters are plotted in red. The n_o of the fitted Megaw parameters is plotted in black.

are increased produces an overall decrease in the birefringence.

The changes to the calculated birefringence from the movement of only the Li, O, and changing lattice parameters is very small compared to those produced by the Ta movement and add up to cancel each other out. The close agreement between the optical properties calculated with the natural structural changes and those with only the Ta atoms moving, suggests that the change in the optical properties of SLT is dominated by the increasing displacement of the Ta atom with increasing temperature.

6.3 Conclusions

The zero-birefringence points of LV flux grown LNT crystals have been measured and shown to increase linearly as a function of Nb composition. The Li composition of the LV grown LT crystal calculated from the zero-birefringence temperature agrees with

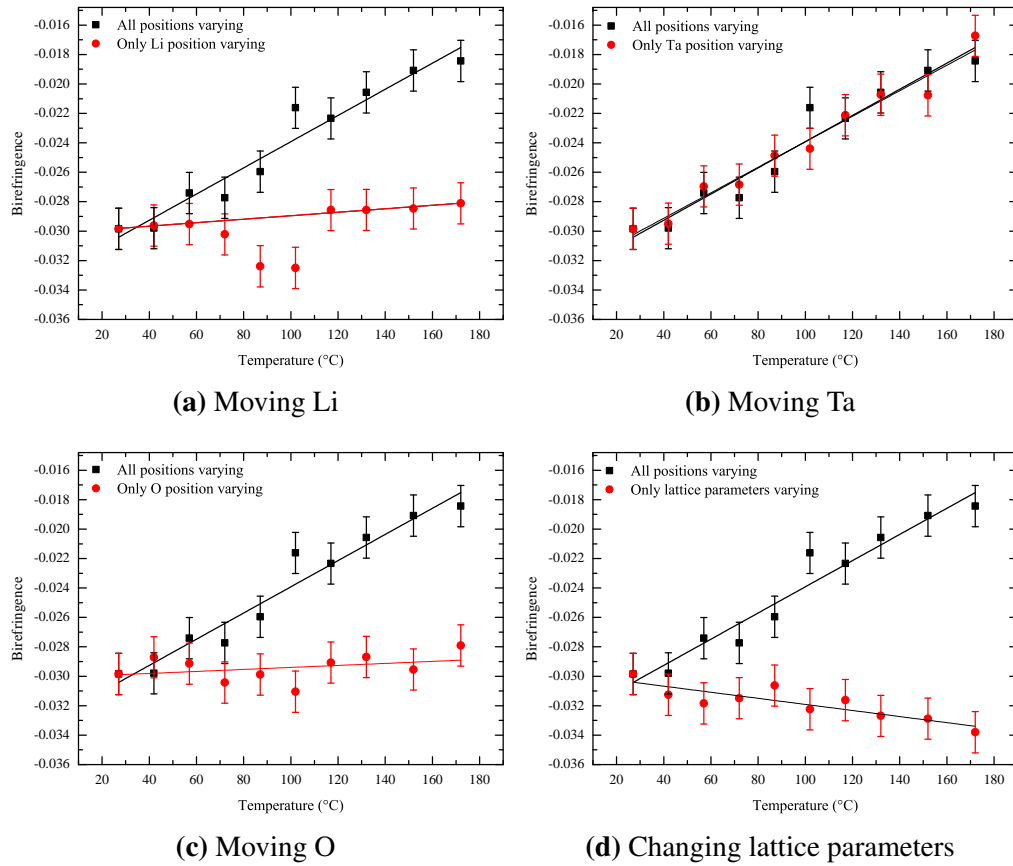


Figure 6-12 The birefringence as a function of temperature for the movement of the (a) Li atoms, (b) Ta atoms, (c) O atoms and (d) and the changing lattice parameters are plotted in red. The birefringence of the fitted Megaw parameters is plotted in black.

the composition determined using the Curie point in section 5.3.4.3. This confirms that the LV flux grown crystals have formed with a small Li-deficiency.

Measurements of the $|\sin\delta|$ on a range of LNT and LT crystals have shown the effects of mechanical domains on the measured signal. The mechanical domains do not affect the determination of the zero-birefringence point but reduce the measured signal above and below this temperature.

DFT calculations have been used to calculate the optical properties of LT based on the structural refinements from the LT neutron diffraction measurements as a function of temperature. By correcting the calculated room-temperature birefringence value to the experimentally measured one, the zero-birefringence temperature was predicted to be 90 °C, which agrees with the previous experimental value. By allowing only one atom to move, the effect of each atom on the optical properties was investigated. The

results showed that the birefringence is most heavily dependent on the displacement of the Ta atom from the centre of the O octahedron and with a smaller dependence on the O position and the lattice expansion.

References

- [1] F. Shimura, Journal of Crystal Growth **42**, 579 (1977).
- [2] I. G. Wood, P. Daniels, R. H. Brown, and A. M. Glazer, Journal of physics. Condensed matter **20**, 235237 (2008).
- [3] A. M. Glazer, N. Zhang, A. Bartasyte, D. S. Keeble, S. Huband, and P. A. Thomas, Journal of Applied Crystallography **43**, 1305 (2010).
- [4] C. Baumer, D. Berben, K. Buse, H. Hesse, and J. Imbrock, Applied Physics Letters **82**, 2248 (2003).
- [5] J. P. Perdew, K. Burke, and M. Ernzerhof, Physical review letters **77**, 3865 (1996).
- [6] S. Cabuk, International Journal of Modern Physics B **24**, 6277 (2010).
- [7] A. Rieffer, S. Sanna, and W. G. Schmidt, Proceedings of ISAF-ECAPD-PFM 2012 (2012).
- [8] S. Cabuk and A. Mamedov, Journal of Optics A: Pure and applied optics **1**, 424 (1999).
- [9] C. Thierfelder, S. Sanna, A. Schindlmayr, and W. G. Schmidt, Physica Status Solidi (C) **7**, 362 (2010).
- [10] R. Bhatt, I. Bhaumik, S. Ganesamoorthy, a. K. Karnal, M. K. Swami, H. S. Patel, and P. K. Gupta, Physica Status Solidi (a) **209**, 176 (2012).
- [11] A. Dhar and A. Mansingh, Journal of Applied Physics **68**, 5804 (1990).

- [12] A. Bruner, D. Eger, M. B. Oron, P. Blau, M. Katz, and S. Ruschin, *Optics letters* **28**, 194 (2003).
- [13] M. Nakamura, S. Higuchi, S. Takekawa, K. Terabe, Y. Furukawa, and K. Kitamura, *Japanese Journal of Applied Physics* **41**, L465 (2002).
- [14] A. M. Glazer, N. Zhang, A. Bartasyte, D. S. Keeble, S. Huband, P. A. Thomas, I. Gregora, F. Borodavka, S. Margueron, and J. Hlinka, *Journal of Applied Crystallography* **45**, 1030 (2012).

CHAPTER 7

Conclusions and future work

7.1 LNT

The structure of LNT powder samples was investigated across the compositional range using XRD measurements from 23 to 820 °C. Reliable structural refinements were only possible on high-Ta content samples because of the preferred orientation of the crystallites in samples with less than 70 mol % Ta. It was concluded that the change in the lattice parameters as a function of temperature was a result of the combined changes in the octahedral tilt and Nb/Ta displacements along with the normal expansion of the lattice with increasing temperature. As the temperature was increased the Nb/Ta displacement and octahedral tilt both decreased.

Similar to the structural changes as a function of temperature, it was found that the Nb/Ta displacement and tilt angle increase as the amount of Nb is increased. This also results in a continuous increase in the lattice parameters from LT to LN.

7.2 LT

The effect of the Li content on the structure of LT has been studied using X-ray and neutron powder diffraction measurements between room temperature and 850 °C. The

a lattice parameter decreases as the composition increases towards the stoichiometric ratio, whereas the *c* lattice parameter decreases with a small increase just before the stoichiometric composition. The amount of Li lost during firing of the samples was carefully quantified to give the correct composition of the samples. It was found that a reduction in the FWHM of the Bragg peaks occurred for stoichiometric samples. This gives an easy method to check for the loss of Li in the production of SLT powder samples.

High-temperature XRD measurements showed the Curie point decreases as the Li content of the samples decreases and agreed with the previously published results. The Curie point measurements are used to provide an estimate of the congruent composition of LT, which gives a calculated value of 48.3 ± 0.2 mol % Li_2O . This is in agreement with the precisely determined value of 48.46 mol % Li_2O measured by Kushibiki et al [1].

7.3 Single-crystal measurements

Structural studies of LV flux grown crystals have provided a clearer picture on the change in the Nb/Ta displacement and octahedral tilt across the compositional range, confirming the previously determined increase with increasing Nb content. The Li content of the LV flux grown crystals was estimated using measurements of the Curie point and comparing them with the values determined using powder XRD. The zero-birefringence temperature of these crystals was measured, giving a similar increase in temperature with increasing Nb content as had been previously measured.

For the first time the absolute structure of CLT has been determined using direct measurements of the piezoelectric d_{33} coefficient. These results show that the positive sense of the polarisation is in the direction of the Ta displacement, confirming the measurements by Abrahams et al [2].

7.4 DFT calculations

The DFT calculations on SLT were performed with a focus on the refractive indices and how they are affected by a variation of the atomic positions. Using the structures

determined from the variable temperature neutron diffraction measurements, the optical results of the DFT calculations were compared to previously measured values. The calculated refractive indices gave a small and negative birefringence, which increased with increasing temperature. The calculated n_e value is close to the expected value for room-temperature value of SLT but the n_o is larger than the experimental value, which results in a lower value for the birefringence as well. The absolute value of the calculated birefringence is incorrect but a trend because of the changing temperature can still be determined. This shows the birefringence increases as the Ta displacement and octahedral tilt decrease.

By repeating the DFT calculations whilst allowing only one atom to move, the effect of each atom on the optical properties was investigated. These results suggest that the Nb/Ta displacement has a very large effect and the changing O position and lattice expansion both made small changes to the birefringence, which cancelled each other out.

7.5 Final conclusions

The structural studies show that LNT and LT both remain polar as they become zero-birefringent, whether the zero-birefringence is because of compositional or temperature changes. The DFT calculations suggest that the increase in the birefringence as a function of temperature is mainly because of the decrease in the Ta displacement. This trend is consistent with the structural and birefringence changes as a result of varying both the Li and Nb/Ta compositions. A reduction in the Li-content results in a decrease of the average Nb/Ta displacement and an increase in the measured birefringence, while an increase in the Nb-content produces an increase in the average Nb/Ta displacement along with a decrease in the birefringence.

7.6 Future work

The structural refinements in this thesis have not included a defect model for the Li-deficient structures. It would be interesting to investigate this using single-crystal neutron diffraction experiments on LT crystals with different Li content and also their bire-

fringe using the Metripol system. DFT calculations on LN with varying Li content have been made by Xu et al [3]. Combining the calculated defect structures with DFT calculations would allow an increased understanding of the how the structure affects the optical properties of the Li-deficient crystals.

An investigation of the mechanical domains using optical and electron microscopy techniques would help to understand the effect of the domains on the measured $|\sin\delta|$ using the Metripol system. A recent investigation of a fragment of LNT90 using an optical transmission microscope equipped with crossed-polars has allowed the domain structure to be measured, as shown in figure 7-1. The fragment of LNT90 broke off during polishing of the main crystal, resulting in a dirty surface. Further work to understand why these domains are not visible in all crystals and how they affect the transmission of light through the crystals is required. Information about the quantity and size of these mechanical domains would provide a starting point for a model describing the profile of the measured $|\sin\delta|$ signal.

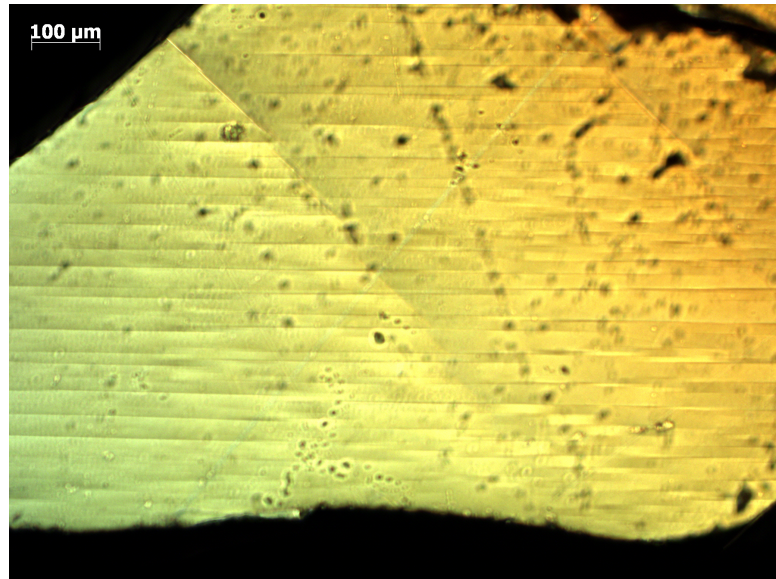


Figure 7-1 Image of the domains in an LNT90 fragment, using an optical transmission microscope equipped with cross-polars.

The birefringence values calculated by Riefer et al [4] including self-energy effects using the VASP code and the GGA agree well with the measured values of CLNT crystals by Wood et al [5]. Very recently it was also shown by Mamoun et al that including a scissor operator in the WIEN2k code to increase the band gap in LN resulted in an improvement of the calculated optical properties [6]. It will be interesting to

use the LNT structures measured in this thesis as the basis for the DFT calculations performed by Riefer et al and Mamoun et al, to allow an improved calculation of the refractive indices of SLNT.

References

- [1] J. Kushibiki and Y. Ohashi, IEEE Transactions on Ultrasonics, Ferroelectrics and Frequency Control **53**, 385 (2006).
- [2] S. C. Abrahams and J. L. Bernstein, Journal of Physics and Chemistry of Solids **28**, 1685 (1967).
- [3] H. Xu, D. Lee, J. He, S. B. Sinnott, V. Gopalan, V. Dierolf, and S. R. Phillpot, Physical Review B **78**, 1 (2008).
- [4] A. Riefer, S. Sanna, and W. G. Schmidt, Proceedings of ISAF-ECAPD-PFM 2012 (2012).
- [5] I. G. Wood, P. Daniels, R. H. Brown, and A. M. Glazer, Journal of physics. Condensed matter **20**, 235237 (2008).
- [6] S. Mamoun, A. E. Merad, and L. Guilbert, Computational Materials Science **79**, 125 (2013).

APPENDIX A

Rietveld example file

This is an example TOPAS input file for refining neutron diffraction data measured at 42 °C.

```
'Goodness of fit parameters
r_wp 5.784 r_exp 4.295 r_p 4.495 r_wp_dash 10.016 r_p_dash 10.153 r_exp_dash 7.437
weighted_Durbin_Watson 0.409 gof 1.347

'Refinement settings
chi2_convergence_criteria 0.001
do_errors
iters 100000
continue_after_convergence
randomize_on_errors

'Data settings
xdd SLT_315K-c.xy
start_X 15
finish_X 147
x_calculation_step = Yobs.dx.at(Xo);
rebin_with_dx_of 0.05

'background terms
bkg @ 32.2648193' _0.0935660454 -1.90458998' _0.145009496 0.63978538' _0.113910533
0.348008487' _0.109891008 0.785846341' _0.0977678273 0.69805523' _0.0962381057

'Neutron experimental parameters
lam ymin_on_ymax 0.0001 la 1.0 lo 1.593333_1.17233615e-005 lh 0.5
neutron_data
LP_Factor( 90)
xye_format
Zero_Error(!zeron,-0.03432_0.00109)
Simple_Axial_Model(@, 15.92025' _0.09874)
```

```

'Structural parameters
str
phase_name "LiTaO3"
a lpa 5.15498°_0.00002
b lpa 5.15498°_0.00002
c lpc 13.77668°_0.00011
al 90.
be 90.
ga 120.
volume 317.051458°_0.00376185592
space_group "R3c"
site Li1 x 0 y 0 z Li_z = 0.25 + Megaw_s; occ 7Li+1 1 beq @ 1.2068°_0.0761
site Ta1 x 0 y 0 z Ta_z = Megaw_t; occ Ta+5 1 beq @ 0.1236°_0.0194
site O1 x O_x = (1/6) - 2 * (Megaw_e + Megaw_d); y O_y = (1/3) - 4 * Megaw_d; z = 1/12; occ O-2 1. beq @ 0.2988°_0.0141
prm Megaw_s 0.04328°_0.00028
prm Megaw_t 0.01426°_0.00012
prm Megaw_d -0.00241°_0.00008
prm Megaw_e 0.06111°_0.00006
prm Tilt_Angle = 180/3.14159 ArcTan(4 3^(0.5) Megaw_e); : 22.94712°_0.01907
scale @ 0.0423289876°_0.000173
r_bragg 3.19941914

'Peak shape
TCHZ.Peak.Type(@, 0.02945°_0.00328,@,-0.13287°_0.00615,@, 0.15876°_0.00218,, 0,@, 0.00536°_0.02783,, 0)

'Parameters for Stephens anisotropic peak broadening
Stephens.trigonal_high
prm eta 0.90160°_0.88749 min 0 max 1
prm s400 -121.17459°_229.09074
prm s004 -1.64674°_3.04874
prm s202 -16.51372°_33.28324
prm s211 1.88161°_9.42221
macro Stephens_lor_gauss(mhkl)
{
local mhkl_ = mhkl;
local pp_ = D_spacing^2 * Sqrt(Max(mhkl,0)) / 1000;
gauss_fwhm = 1.8/3.1415927 pp_ (1-eta) Tan(Th);
lor_fwhm = 1.8/3.1415927 pp_ eta Tan(Th);
}
macro Stephens.trigonal_high
{
Stephens_lor_gauss(Abs(
s400 (H^4+ 2 H^3 K + 3 H^2 K^2 + 2 H K^3 + K^4) +
s004 L^4 +
s202 (H^2 L^2 + H K L^2 + K^2 L^2) +
s211 (H^2 K L - H K^2 L + 2 H^3 L / 3 - 2 K^3 L / 3)
))
}

'Background peaks in experiment

```



```

prm furnace_scale 0.87598' .04202

xo_Is

xo @ 40.1530044' .0.0186077393 I = 2.399482 * furnace_scale;

xo @ 46.667477' .0.0508470878 I = 0.875470 * furnace_scale;

xo @ 50.1584682' .0.175884749 I = 0.412976 * furnace_scale;

xo @ 67.7750466' .0.0882206964 I = 1.022087 * furnace_scale;

xo @ 48.0903245' .0.102188198 I = 0.438469 * furnace_scale;

xo @ 64.4615018' .0.150967259 I = 0.775546 * furnace_scale;

xo @ 66.8283956' .0.148298339 I = 0.615464 * furnace_scale;

xo @ 25.2326626' .0.15201581 I = 0.104684 * furnace_scale;

xo @ 51.5303549' .0.105574909 I = 0.485187 * furnace_scale;

CS_L(, 21.91418_1.64527)

xo_Is

xo @ 39.3732567' .0.023361705 I @ 0.223745447' .0.0469953789

Strain_L(, 0.24391_0.32267)

```

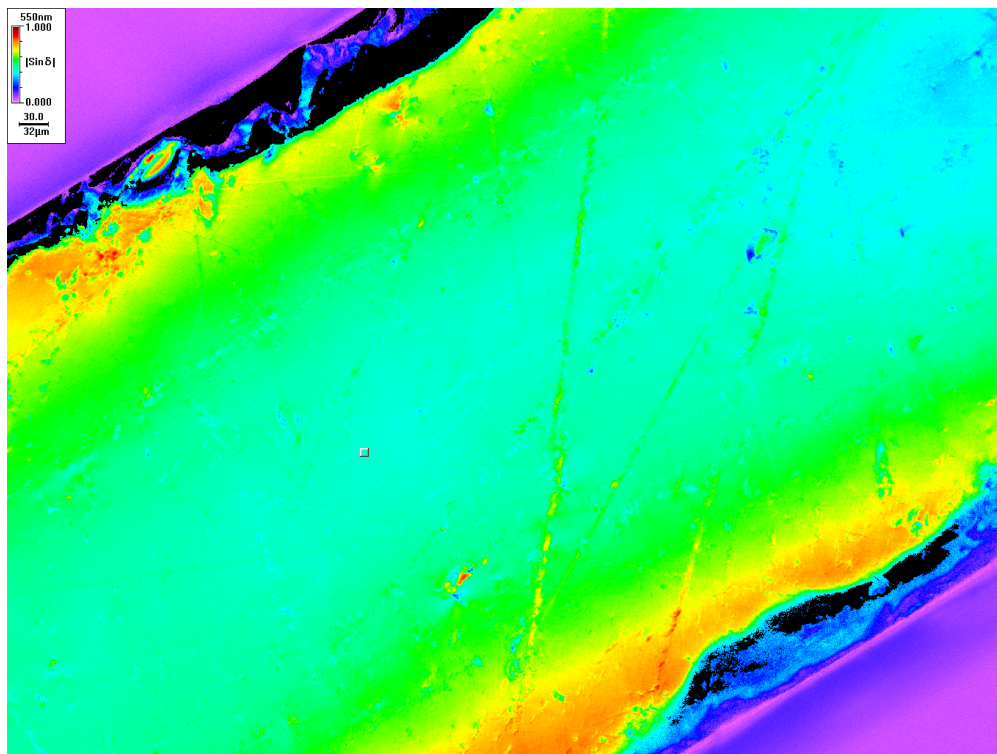
APPENDIX B

Metripol examples

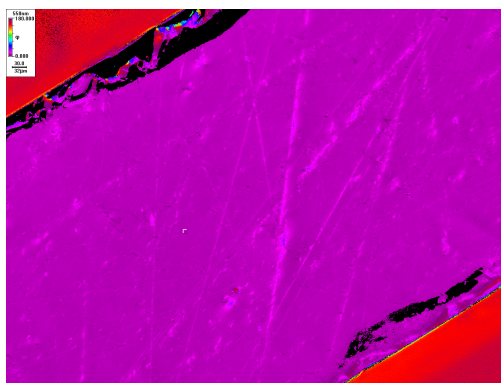
The measured $|\sin \delta|$, orientation and intensity images measured on the poled CLT crystal in section 6.1.3 in figure B-1 at 30 °C, in figure B-2 at 323 °C and figure B-3 at 600 °C, using the 550 nm filter. False colours have been applied to the measured data to produce the images. In the images measured at 30 °C, the area used for averaging is indicated by the square. As the temperature is increased the position of the sample with respect to the microscope drifted and this can be seen in the images. This was taken into account when analysing the data by moving the averaging square with the drift.

The $|\sin \delta|$ and orientation images at 323 °C show the 180° change in the orientation as the $|\sin \delta|$ signal reaches a minimum ($\delta = n\pi$). In the $|\sin \delta|$ the minimum signal is given by the pink colouring and results in the change from green to purple in the orientation image.

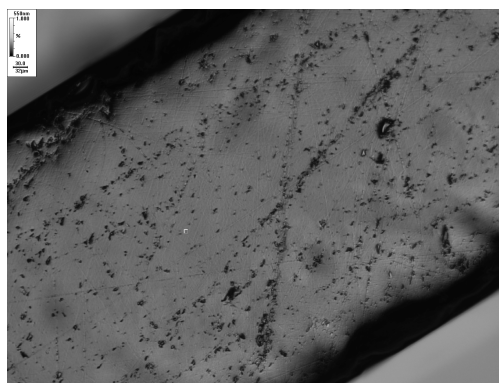
On the attached cd, is the video of $|\sin \delta|$ recorded for the heating run of CLT with a wavelength of 550 nm, using the Metripol system. The video is titled: CLT-550nm-sind.mp4.



(a) $|\sin \delta|$

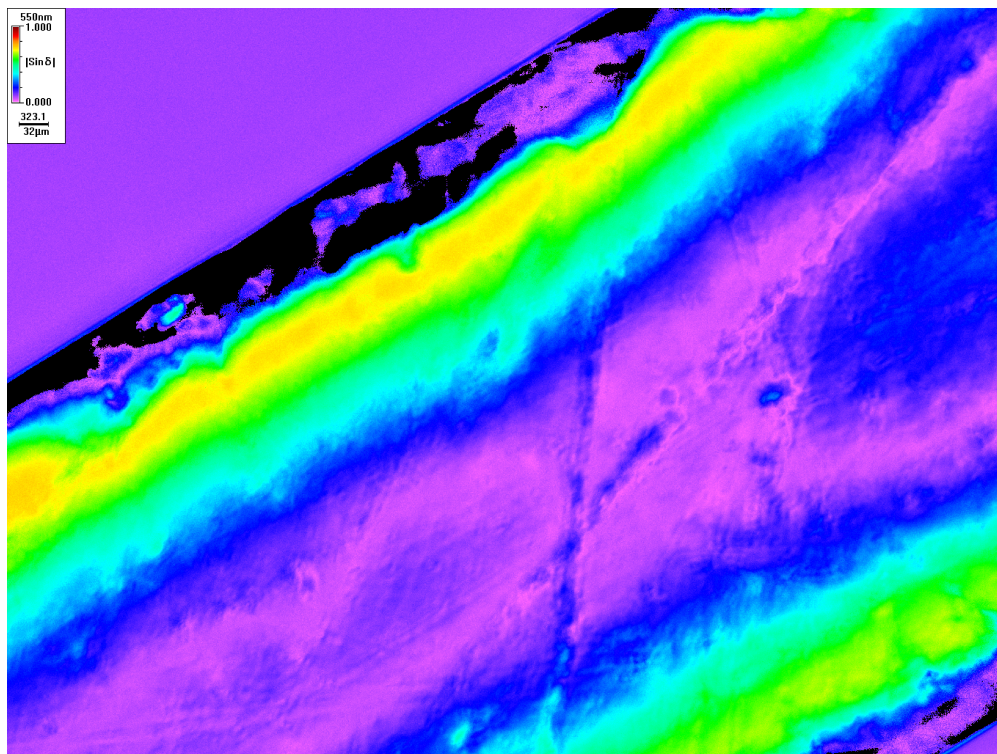


(b) Orientation

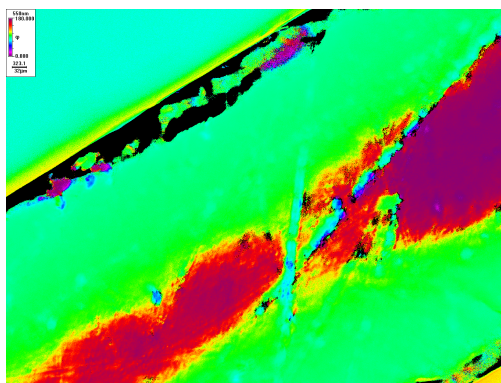


(c) Intensity

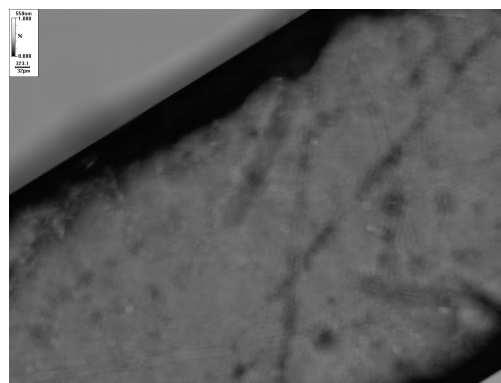
Figure B-1 The measured (a) $|\sin \delta|$, (b) orientation and (c) intensity images at 30 °C on the poled CLT sample.



(a) $|\sin \delta|$

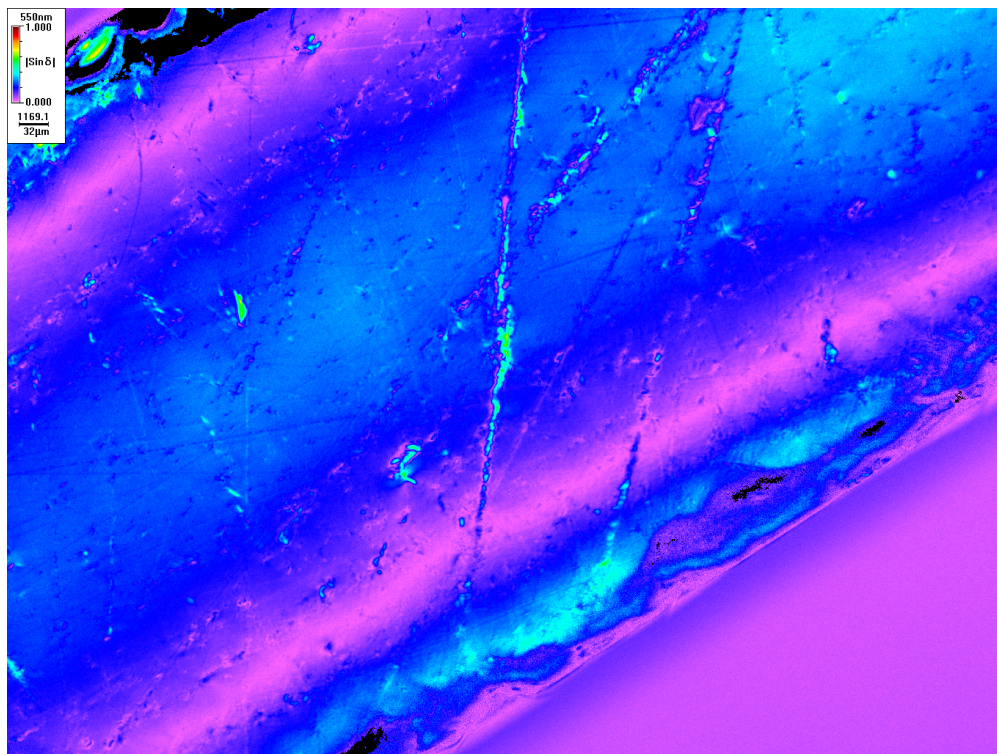


(b) Orientation

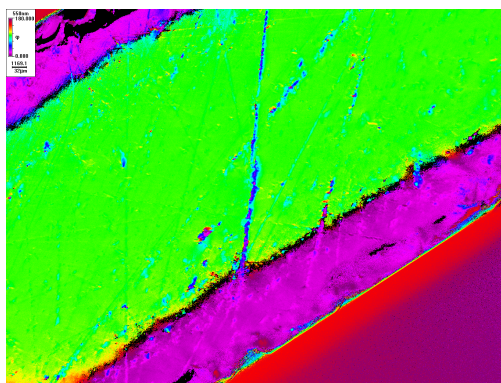


(c) Intensity

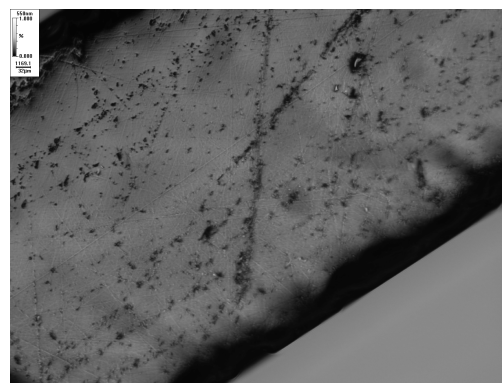
Figure B-2 The measured (a) $|\sin \delta|$, (b) orientation and (c) intensity images at 323 °C on the poled CLT sample.



(a) $|\sin \delta|$



(b) Orientation



(c) Intensity

Figure B-3 The measured (a) $|\sin \delta|$, (b) orientation and (c) intensity images at 600 °C on the poled CLT sample.